UNIVERSITY OF NAIROBI

LASER RAMAN MICROSPECTROMETRIC ASSESSMENT OF URANIUM FORENSICS

SIGNATURE IN AEROSOLS OVER A MODEL NUCLEAR ATMOSPHERE

MSc. THESIS

By

JUMA MOSES WABWILE

I56/73670/2014

BSc. (Hons)

A thesis submitted for examination in partial fulfillment of the requirements for the award of the Degree of Master of Science in Physics of the University of Nairobi.

© Nov 2018

DECLARATION

I hereby declare that this thesis submitted for the Master's degree at the Department of Physics, University of Nairobi is my original work and has not previously been presented to any other institution of higher learning.

JUMA MOSES WABWILE

I56/73670/2014

Department of Physics, University of Nairobi.

Signature ………………………………… Date ……………………..

This thesis has been submitted with approval of the undersigned supervisors for examination

Dr. Angeyo H. Kalambuka

Signature ………………………………….Date ………………………..

Dr. Alix Dehayem Massop

Signature ………………………………….Date …………………

DEDICATION

I am never alone wherever I am.

The air itself supplies me with a century of love.

When I breathe in, I am breathing in the laughter,

tears, victories, passions, thoughts, memories,

existence, joys, moments and the hues of the sunlight

on many tones of skin; I am breathing in the same air

that was exhaled by many before me. The air that bore

them life. And so how can I ever say that I am alone?

C. Joy Bell C.

Dedicated to my longtime friend, my wife and the Love of my life Esther Precious Wabwile and my loving son Felician Niels Juma.

Acknowledgements

Abstract

Nuclear forensics relies on environmental sampling to detect undeclared nuclear activities. In the nuclear fuel cycle, mining and processing of uranium is accompanied by immobilization and translocation of uranium to the environment. Capability for direct and rapid analysis of micro-size particles such as aerosols in the environment is therefore a powerful tool to monitor undeclared nuclear activity. The strength of particle analysis is that it allows analyzing very small amounts of material exhibiting an undeclared nuclear forensic signature. Uranium bearing aerosol micro-particles sampled from e.g. a uranium mine or reactor atmosphere have unique inherent signatures that can be used to study the dynamics of detecting undeclared nuclear activities. For this work, typical uranium-specific Raman scatter bands were characterized using 532 nm and 785 nm lasers-based Raman microspectroscopy for different uranium molecules with different embedding anions (uranium trioxide, uranyl chloride, uranyl sulphate and uranyl nitrate). The Raman scatter bands varied in the range of $(810$ to $870) \pm 15$ cm^{-1} for both laser excitations. The uranium forensic signatures were used to characterize uranium bearing aerosol particulate matter. A multivariate calibration strategy using artificial neural network (both new feedforward and cascade correlation algorithms) was developed for quantification of trace uranium in aerosol particles sampled around Mrima hills which is a quasi-uranium mine. The validation of the analytical method was done using a synthetic membrane standard based on the IAEA-RGU-1 certified reference material and the relative error of prediction was found to be $\leq 10\%$. Depending on the sampling location, the concentration of uranium in the aerosols was found to range from (200-800 ppb) being more enriched in PM$_{4.5}$ as compared to PM$_{2.5}$ size fraction. This shows that most of the uranium was from the immediate environment as opposed to long range transport to the study area. In addition, principal component analysis was employed on both particulate sizes to explore the variability of their intrinsic chemical components. Using both the scores and loadings plots, the samples classified based on their sampling source fields. Whereas all PM$_{2.5}$ grouped together with some PM$_{4.5}$ that were sampled away from road sides, all other PM$_{4.5}$ particles were grouped differently indicating that their source is different. The PCA also showed that most of PM$_{2.5}$ were as a result of sea spray as shown by presence of chloride based uranium bands in the loadings plot. The heterogeneity of individual aerosol particles was characterized by overlap of spectral information (completely buried in the background) that could not be resolved by conventional Raman analysis.

To yield information about the specific uranium species present in the particles as well as the uranium distribution within the particles, MCR-ALS was employed. The MCR-ALS gave results at an explained variance of 80.883 % and lack of fit of 9.56. Three distinct uranium scatter bands specific for uranium (814, 854 and 868 cm^{-1}) were resolved as typical forensic signatures specific for uranium molecule in aerosol particles. The findings of this work are important in developing a spectral library that can be used by nuclear security authorities for environmentally sampled particulate matter.

Table of Contents

List of Tables

List of Figures

xi

List of Acronyms and Abbreviations

ANN   Artificial neural network

BDL   Below detection limit

ET   Exposure time

HBRA   High background radiation area

IND   Improvised nuclear device

IR   Infrared

LSD   Laser spot diameter

LOD   Limit of detection

MCR   Multivariate curve resolution

ML   Machine learning

MSE   Mean Square Error

MOX   Mixed oxide

NORM   Naturally occurring radioactive material

NA   Numerical aperture

NA   Number of accumulations

NRM   Nuclear and radioactive materials

NF   Nuclear forensics

PCA   Principal component analysis

PLS   Partial least square

PM   Particulate matter

RDD   Radiological dispersive device

REP   Relative error of prediction

RRS   Resonance Raman spectroscopy

SNR   Signal to noise ratio

SERS   Surface enhanced Raman spectroscopy

SEM   Scanning electron microscopy

SIMS   Secondary ion mass spectrometry

TERS   Tip enhanced Raman spectroscopy

TE-NORM   Technologically enhanced naturally occurring radioactive material

XRF   X-ray fluorescence

XRD   X-ray diffraction

1 INTRODUCTION

1.1 Background Information

Nuclear forensics (NF) is a relatively new scientific field that has been gaining significant prominence since the 1990's as a response to the illicit trafficking of nuclear materials. The goal of this field is to identify and quantify the hazard and the origin of nuclear and radiological material thus helping to strengthen nuclear security as well as prevent nuclear terrorism (Fedchenko, 2014).

In the recent past, nuclear forensics research has dwelt around detecting uranium and other radioactive elements in soils and uranium ores towards nuclear safety. Such research has shown that nuclear or other radioactive materials have been released into the environment or illegally possessed (Kemp, 2008). This has been prompted by nuclear accidents and the inadvertent destruction of devices containing nuclear weapons, illegal dumping of nuclear wastes, releases of traces of radioisotopes from declared and/ or clandestine activities, etc. In investigating such incidents, questions arise regarding their intended use, the origin and where applicable the route with which the nuclear and radioactive material was diverted from statutory nuclear fuel cycle (Luna *et al.*, 2014).

NF analysis is a key technical capability that exploits specific signatures from the sample e.g. the surface roughness, microstructure and the isotopic composition that is inherent to nuclear or radioactive material to provide information on its source, production and history. Since NF signatures are created, modified and destroyed as the material moves through the nuclear fuel cycle, it is important to consider the relevant NF analytical techniques in relation to where the material is produced in the fuel cycle. Each step in the fuel cycle provides important NF

signatures that can be used to identify and constrain the source of the material (Keegan *et al*., 2014) .

1.2   Raman Microspectroscopy

In this technique, a Raman microspectrometer is used in place of a standard Raman spectrometer. Such a spectrometer is integrated into an optical microscope that makes it easy to acquire Raman spectra of microscopic samples or microscopic areas of larger samples. This makes it possible to acquire maximum information from very little sample sizes.

Nuclear forensic analysis relies on physical, isotopic and chemical analysis of sometimes microscopic quantities of materials. In case of a nuclear explosion for example, trained forensic teams would need to gather samples within the vicinity of the explosion, some of which are too tiny or worse still embedded in a mixture of debris. The analytical challenges of such minute samples may be overcome by such microscopic techniques.

1.3   Utility of Raman Spectroscopy in Nuclear Forensics

There already exist conventional analytical techniques that have found applicability in nuclear forensics. Such techniques include; infrared spectroscopy (Palacios and Taylor, 2000), gamma ray spectroscopy (Eriksson *et al.*, 2005; Shawky *et al.*, 2001), SIMS (Ranebo *et al.*, 2007; Betti *et al.*, 1999), XRF (Fiedor *et al.*, 1998) and XRD (Keegan *et al.*, 2014) most of which have however proved to be time consuming, invasive and at times NF signature destructive. In environmental sampling for forensic purposes e.g. by swiping nuclear installation surface (Pointurier and Marie, 2010a) or dubbing adhesive carbon discs near a nuclear facility, we are presented by forensic scenarios that utilize minute sample sizes which is a common phenomenon in modern nuclear forensics.

Raman spectroscopy uniquely identifies samples based on their molecular vibrations. The vibrational modes obtained can be regarded as a molecular fingerprint that uniquely identifies substances in a sample (Zachhuber *et al.*, 2011). However, the spectra acquired using this technique are hard to interpret due to its multidimensional nature whose latent information content can be hard to extract. These limitations may be overcome by coupling Raman microspectrometry with multivariate chemometric methods such as PCA, ANN and MCR.

Whereas PCA helps to reduce the data dimensionality and spectral exploratory analysis, ANN performs multivariate calibration and extracts relevant analytical information from the spectra (Howley *et al.*, 2006). MCR on the other hand is a technique that helps to determine the chemical composition and the spatial distribution of analytes in a sample (Batonneau *et al.*, 2006). Since aerosol particles are heterogeneous with spectral overlaps, MCR is very useful in resolving such spectra to identify uranium scatter bands as well as show the spatial distribution of U within the particulate matter. Confocal laser Raman spectroscopy is therefore a remarkable tool for nuclear forensics since it has the ability to realize 3-D structural and chemical characterization of materials and even particles at nanometer scale (Worobiec *et al.*, 2011).

1.4 Uranium in the Environment

Uranium is a radioactive element that occurs in soils, rocks and even air (ATSDR). It exists as ^{234}U, ^{238}U and ^{235}U in the environment and occurs in its other chemical forms such as UO_2, UO_3, U_3O_8 (most stable form of uranium), UF_4 and UF_6. In nature, uranium is also found to be compounded to anions such as chlorides, sulphates, nitrates and phosphates since it cannot exist independently (Driscoll *et al.*, 2014). Based on these anions, uranium exists as uranyl nitrate, uranyl chloride, uranium sulphate and uranium fluoride (Sparks, 2003).

1.4.1 Immobilization of Uranium in the Atmosphere

Uranium normally gets immobilized in the atmosphere due to nuclear/ and radiological activities such as coal-fired power plants or as hot particles like in nuclear power plant accidents/emissions. This formed the basis of the earliest forensic testing of radioactive emissions emanating from the release of a nuclear material in the United States during the Cold War (Martin *et al.*, 1964). The Chernobyl nuclear power plant accident in 1986 released a formidable number of condensable radioactive materials to the environment. The radionuclides of some of the most volatile elements like caesium were immobilized over long distances and could be detected in aerosols and in bulk materials on the ground in many parts of Europe. Thereafter, small highly radioactive solid particles could be found in the USSR and other countries outside of Ukraine. The individual particles were so radioactive that they could be detected by Geiger counters. Such individual radioactive materials released to the ambient are referred to as hot particles since "hot" refers to highly radioactive (Sandalls *et al.*, 1993). The natural radionuclides present in coal consist of members of the U-238 and Th-232 decay chains that are considered to be in equilibrium with their parent radionuclides (Zakaria *et al.* 1998). During combustion, due to the volatization of the components that are being combusted, the radionuclides within the components are separated into the gas phase (air emission) and the solid phase (fly ash), depending on the volatility of the elements.

Coal contains uranium and thorium which occur in such trace amounts in natural, but when coal is burned, the uranium and thorium are concentrated up to a few times higher than their original levels. In fact, the fly ash emitted from burning coal for electricity by a power plant, carries into the environment 100 times more radiation than a nuclear power plant producing the same amount of energy (Mandal and Sengupta, 2003).

1.4.2 Uranium in Atmospheric Aerosols

Uranium naturally occurs at trace levels (24-300 ppb) in airborne dust (Kemp, 2008). Human activity however creates additional sources for example through uranium mining and atmospheric testing of nuclear weapons. Among these, fly ash from coal combustion is one of the major sources of release of uranium to the environment (Mahur *et al.*, 2008).

Compared to primary sources of uranium such as in coal mines, the concentration in secondary sources like fly ash is always enriched. This is because the uranium in fly ash mixes with natural uranium hence getting elevated in the atmosphere (Zielinski and Budahn, 1998).

Although uranium exists in many chemical forms, it is UF_6 that escapes to the atmosphere from a nuclear power plant or dust from a given uranium mine. Uranium hexafluoride reacts immediately with atmospheric water vapor to form uranyl fluoride (UO_2F_2) which coalesces around dust particles in air. The released uranium blends with natural uranium in the environment, altering the isotopic content found in the sample and leaving a unique signature of the presence of activities involving uranium. The particles grow larger with time and eventually fall back to earth in the vicinity or even far away from a uranium facility (Lau *et al.*, 1985).

At atmospheric temperature and pressure, UO_2F_2 is a solid hence it exists as an aerosol particulate matter (PM). Large aerosols ($\varnothing > 10$ μm) are efficiently scavenged from the atmosphere by rain and gravity. Therefore, it is possible to collect rain water, evaporate it and leave particulate suspensions that may be analyzed for uranium content. However, the fine and ultrafine aerosols (≤ 4.5μm) can persist in the atmosphere on time scales of 4 - 40 days (Kemp, 2008).

Atmospheric aerosols may thus easily contain a given concentration of for example depleted uranium (DU) above the recommended limits. The level of such concentrations in aerosols raises

concern on not only the nuclear facility responsible for the high levels of uranium in air but also the nuclear security threats that come with it. Therefore, aerosol sampling can be used for environmental monitoring in support of nuclear security and safeguards.

1.4.3 Challenges of Detecting Uranium over Nuclearized Atmospheres

Analytical procedures involved in sampling and subsequent analysis of aerosols undergo myriads of challenges. These challenges become more pronounced when dealing with uranium compounds in micrometer sized samples. Extracting information about their molecular composition is a challenge since during analysis, the oxidation state of the uranium particles may change besides the samples being burned (Stefaniak *et al.*, 2009). On the other hand, NF relies on the measurable parameters that are characteristic for a given material to help draw conclusions. However, such parameters (signatures) may change from the time of sampling, sample storage or particle relocation to another substrate in the case of techniques that do not do direct analysis. This calls for techniques that can perform direct analysis of samples without lengthy sample preparation procedures. Furthermore, uranium, just like other NRM are often accompanied by different types of feed material like ores of different mineralogical nature or from other secondary sources when in the environment. In such a scenario, the interpretation of the signatures is complicated. This is because the uranium could be embedded with the feed material or altered by the purification process in case of its extraction. This challenge could also be manifested in analysis of uranium bearing aerosol particles since their Raman signals could be hardly visible (Krajkó *et al.*, 2016).

1.5 The Nuclear Fuel Cycle

In the context of the nuclear fuel cycle as in Figure 1.1, NF signatures can be defined as different measurable attributes that can be assigned to different materials. Since the signatures are created, modified and destroyed when the material moves through the cycle, it is significant to consider

appropriate analytical techniques that can link to where the material is produced in the cycle (Keegan *et al.*, 2014).
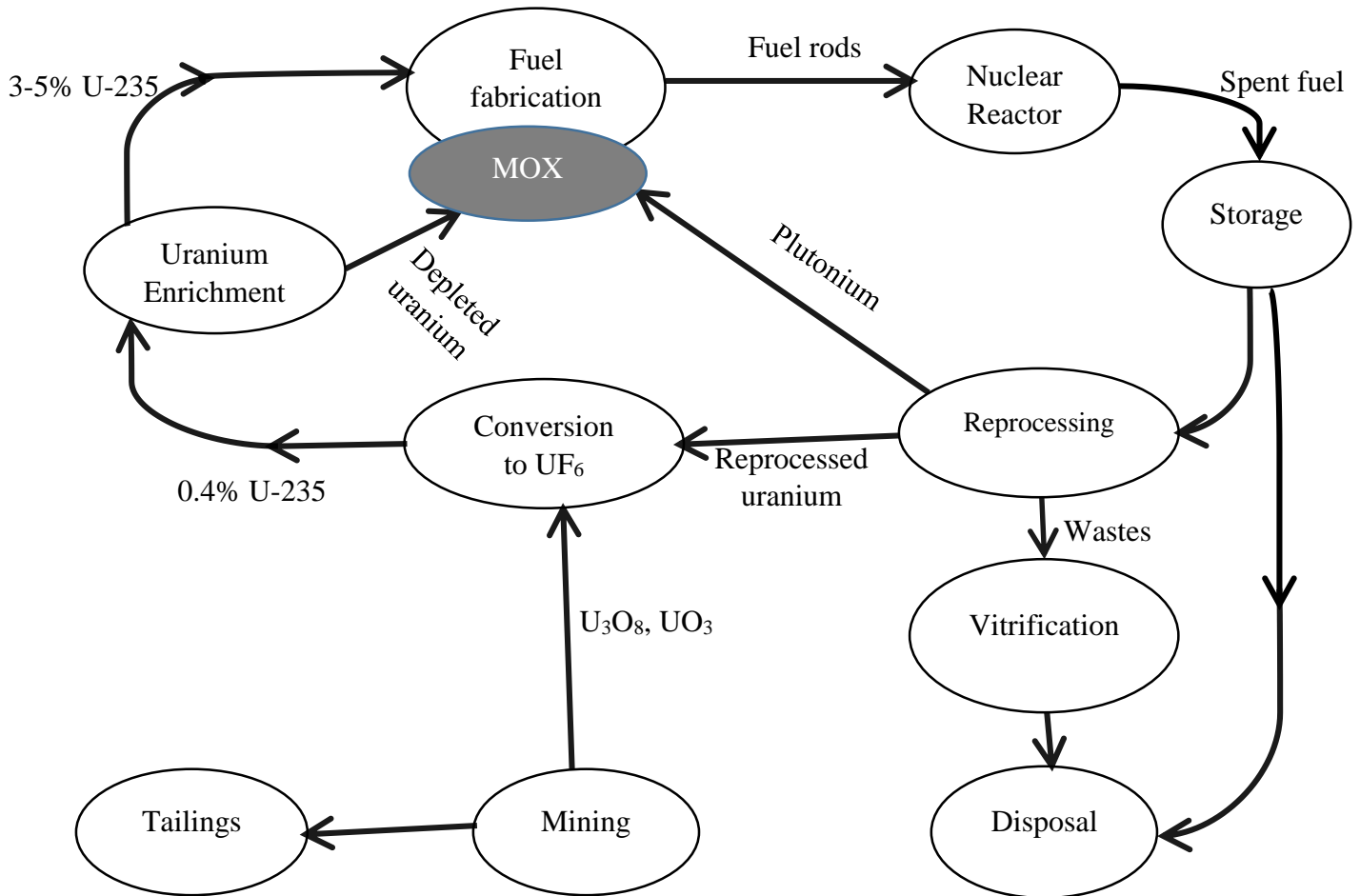
The nuclear fuel cycle involves ten steps of mining, milling, conversion, enrichment and fuel fabrication. After uranium oxide rods have spent about three years in a reactor, the used fuel may undergo a further series of steps including storing it temporarily, reprocessing and recycling (Moody *et al.*, 2014).

After extraction of natural uranium from the ore in which it exists, the chemical separation during milling becomes a critical stage in the nuclear fuel cycle. Chemical separation entails crushing up the ore, adding water, pressurizing, heating up and even altering the pH. Uranium gets dissolved

and precipitated. The tailings, the crushed rock left over after the uranium has been removed are deposited off or on site. Tailings need to be isolated from the environment since they contain long lived radioactive materials in low concentrations and may be toxic materials such as heavy metals (Moody *et al.*, 2014).

HBRA which mimic a quasi-uranium mine, release U- bearing aerosols which can be linked to the tailings in the nuclear fuel cycle. Liquids from mine tailings are also expected to contain uranium. It is possible therefore as has been shown elsewhere by Lu *et al.*, (2016), to sample natural waters from a uranium facility and quantify the trace uranium levels.

1.6 High Background Radiation Areas (HBRA) as Model Nuclear Atmospheres

By definition, HBRA is an area where the sum of cosmic exposure situations and the natural radioactivity in soil, rocks, indoor and outdoor air, water, food etc. is above the annual effective dose levels (Achola *et al.*, 2012). Such areas have been observed to be composed of deposits of mineral ores such as thorium, niobium and uranium besides other naturally occurring radioactive materials and rare earth elements. In Kenya, several areas have been designated as HBRA and they include North and South Ruri in Lambwe (Achola *et al.*, 2012), Mrima hills in South Coast Kenya (Mangala, 1987) and Homa mountain (Otwoma *et al.*, 2000) in Kenya.

When mining of any mineral or earth crust modification takes place in HBRA e.g. fluorspar mining in the Kerio valley or titanium mining in Mrima hills in Kwale, HBRA-NORM becomes HBRA TE-NORM and aerosols from such regions become even more enriched in uranium. Such elevated uranium levels in those areas therefore makes HBRA a mimic of a typical uranium mine or other uranium processing facility (O'Brien and Cooper, 1998). In addition, HBRA aerosols will dilute

with other atmospheric (perhaps U-bearing) aerosols from far and near, and hence the isotopic composition will be modified. The particles in such areas are also a "replica" of fine and coarse debris that one would encounter at for example radiological crime scenes involving IND or RDD when surfaces are sampled (swiped) for NF forensic investigations.

1.7 Problem Statement

Direct rapid analysis of uranium-bearing particles in the fine or hyperfine range is a desirable primary tool that can be utilized by nuclear safeguard or security authorities for detecting undeclared nuclear activities. Such aerosol particles in the environment vary in size (fine, hyperfine and coarse), chemical form, isotopic composition, formation mechanism and origin. Their analysis can comprehensively inform nuclear forensics and by extension inform on attribution. Conventional nuclear forensic analytical techniques are tedious and at times destructive and as such are inappropriate to conduct direct, rapid analysis and attribution of micro sized NRM. Laser Raman microspectroscopy coupled with multivariate chemometric techniques has the requisite potential to be explored towards realizing nuclear forensic analysis and attribution of the uranium bearing aerosols over a nuclearized atmosphere.

1.8 Research Objectives

1.8.1 Main Objective

The goal of this work was to utilize laser Raman microspectroscopy to perform direct, rapid detection and quantification of uranium in aerosols over a model nuclear atmosphere in the context of nuclear forensic analysis.

1.8.2 Specific Objectives

i. To utilize available uranium compounds and analytical grade salts to prepare uranium bearing aerosol simulates for quantitative model development using drop coating deposition Raman microspectroscopy.

ii. To develop multivariate calibration models (based on newff-BP and cascade correlation ANN) for determining uranium in the simulates developed in (i) above.

iii. To predict and quantify uranium in ($PM_{2.5}$ and $PM_{4.5}$) aerosol particles utilizing the calibration model developed in (ii) above.

iv. To investigate and exploit PCA and MCR for spectral and spatial resolution of uranium signature in $PM_{4.5}$ aerosol field samples in the context of source attribution.

1.9 Significance and Justification of the Study

A good energy mix assures sustainability for Kenya's power needs. The Kenya government plan to construct its first nuclear power plant by 2021 to bring down the cost of electricity. The nuclear plant, projected to be complete in 2027 will add 1000 MW according to projections by Kenya Nuclear Electricity Board. The recent signing of the agreements with the government of South Korea and the approval received from the IAEA seems to have added an impetus to the momentum of the implementation of the project.

However, the quest for Kenya to set up a nuclear power plant may increase the risk of nuclear and radiological materials not only being smuggled but also increase the risk of nuclear terrorism using RDD and IND. In the recent past, there seems to be already substantial illegal trafficking and possession of radiological material in the region yet little is known if the experienced attacks are as a result of RDD or IND. It is against this backdrop that there is need to set up nuclear forensics laboratories through development of nuclear signatures and train enough forensic analysts.

This work therefore, aimed at analyzing uranium bearing aerosols from high background radiation areas using confocal Raman spectroscopy in order to develop a method for establishing the undeclared nuclear activity, monitor non- proliferation and to respond to the environmental releases of NRM with good accuracy and swiftly. The developed method can be of great utility in analyzing microdroplets in case of a nuclear explosion since very little sample size is required for analysis. This technique is also versatile since environmental sampling lies in the observation that processes involving the treatment of nuclear material release small amounts of uranium and other fissile materials.

1.10 Scope and Limitations of the Study

The study was limited to uranium as the only trace element and hence the spiking scheme only entailed uranium as the element of interest since it plays a major role in nuclear forensics. The anions to which uranium gets embedded only provided a base matrix. The study however had a limitation of generating monodisperse aerosol particles as would be expected when sampling using cascade sampler. On this, we resorted to using drop coating deposition technique.

1.11 Hypothesis of the Study

Uranium concentrations in individual aerosol particles are possible to quantify using Raman spectroscopy and are greatly influenced by the size of the particles and by the process through which the particles were immobilized as well as the chemical composition of the aerosol matrix in which the PM are embedded.

2 LITERATURE REVIEW

2.1 Chapter Overview

Nuclear forensics is defined as " the examination of nuclear or other radioactive materials, or evidence that a material is contaminated with radionuclides, in the context of legal proceedings (Fedchenko, 2014)". The purpose of nuclear forensics is to help produce knowledge base on which the law enforcement agencies or decision makers would be able to formulate their responsiveness to the event or action at hand (Mayer *et al.*, 2013). This chapter presents a review of literature on nuclear forensics and analytical techniques used in Nuclear Forensics.

2.2 Raman Spectroscopy verses other Vibrational Techniques

IR spectroscopy is one of the tools for forensic identification of materials, primarily because of its ease of use and the availability of large searchable digital libraries of spectra (Cooper *et al.*, 1997). However, IR spectroscopy has several limitations among them: minimal molecular information is given for most samples, it is time consuming, solid matrix must be relatively transparent in the spectral range of interest and the analyte molecule must be active in the IR region.

Laser Raman spectroscopy has begun to emerge as a forensic tool, several advantages being attributed to it for forensic analysis. Unlike IR spectroscopy, Raman spectroscopy provides complementary information (some vibrational modes of motion are IR – inactive but Raman active and vice versa.)

2.2.1 Types of Raman Spectroscopies

There are several types of Raman spectroscopic techniques that are used based on the nature of the sample (liquid, solid or powder) being analyzed or the detection limits being desired (Smith and Dent, 2013).

Surface Enhanced Raman Spectroscopy is a surface-sensitive technique that enhances Raman signals by adsorbing molecules of the analyte on a rough metallic surface or by use of nanostructures (Stiles *et al.*, 2008). Ruan *et al.* (2007) used gold Nano particles of diameter 50-60 nm as SERS substrate to detect 2 ppm uranium in aqueous samples. The detection limit was found to be three times lower than when a bare substrate was used in the case of (Burneau and Teiten, 1999). Bhandari (2011) used silver modified polypropylene filter substrates to study the rapid detection of uranyl species in aqueous solution. The results showed that the concentration of uranyl ion was detected to as low as 20 ppb. However, this study was limited to detecting uranium from a liquid and not in suspension like it would be expected in aerosols. This study mimics aerosol particles in a model nuclear atmosphere by using dried drops with the purpose of also lowering the limit of detection of uranium in aerosol particles.

Resonance Raman spectroscopy occurs when the wavenumber of the incident radiation is very close to or overlaps with the electronic transition of the scattering analyte in the sample. Due to the frequency coincidence, the intensity of the scattered photons is greatly enhanced. Low concentrations can therefore be measured (Clark and Dines, 1986). Resonance Raman however suffers from a lot of fluorescence (Efremov *et al.*, 2008).

Tip Enhanced Raman spectroscopy on the other hand uses a fine metal tip (to the order of nm) of a molecular film (Stöckle *et al.*, 2000). The technique can be used for molecular analysis with very

good spatial resolution since the tip provides localized nanoscale enhancement of the Raman signals from a sample located under it. However, it is limited to the size and shape of the apex.

2.3 Nuclear Forensic Signatures in Nuclear and Radioactive Material

In nuclear security and safeguards, a number of material characteristics are utilized either to verify the declared origin (for safeguard purposes) or to identify the source of an unknown nuclear material for forensic purposes (Varga *et al.*, 2017). Knowledge of nuclear forensic signatures (elemental, molecular, isotopic composition, crystallinity (and their spatial micro-distribution) and their material stress /strain) often leads to the attribution of nuclear and radioactive materials.

For instance, concentration of major, minor and trace – level constituents in a sample, the isotopic composition of impurities, the morphology of the material or its molecular structure can lead us to the origin of the sample (Varga *et al.*, 2017).

2.4 Determination of Uranium Signatures using Raman Spectroscopy

To uniquely identify the molecular fingerprint of a particular sample, its vibrational modes are obtained (Zachhuber *et al.*, 2011). Laser Raman spectroscopy is a type of optical vibrational technique that is capable of *in situ* molecular identification of molecules or group of atoms that are Raman active in solid, liquid or gaseous form. The technique is non- invasive, non-destructive and needs little or no sample preparation. A laser excites a given target/sample and the spectrum of the backscattered radiation serves as a fingerprint to the Raman active bonds within the sample (White, 2009).

2.4.1 Relevant Signatures used to Characterize Uranium

To characterize any uranium compound, one needs to know if uranium is Raman active. A lot of research has gone into identifying the different Raman signatures that are specific to uranium compounds in different matrices. However, little seems to have been done in also quantifying uranium in its ng/g concentration ranges as in aerosol particles.

In 2009 for example, a state policing agency in Australia undertook a detailed forensic analysis to characterize and identify contents of a small glass jar labelled "Gamma source" in a clandestine drug laboratory. The isotopic, phase composition, microstructure and other characteristics relevant to nuclear forensics were measured on the seized sample. The key nuclear forensic signatures used to identify the material were the uranium isotopic composition and the rare earth elements (REE) pattern. These measurements in combination with statistical analysis of the elemental and isotopic content led to the conclusion that the seized material originated from Mary Kathleen, a former Australian mine. This study shows that it is indeed possible to determine the source and identity of a nuclear material by use of forensic analysis (Keegan *et al.*, 2014).

Rare earth elements (REE) have strong optical transitions suitable to spectroscopic measurements which allow one to get systematic atomic and nuclear data (Wakui *et al.*, 2003). REE patterns remain invariant throughout the nuclear fuel cycle, so are excellent for source attribution. However, their chemical similarity makes their determination difficult and complicated when using IR spectroscopy. Especially serious problems arise if the selected REE must be determined in the mixtures of the other REE (Wakui *et al.*, 2003).

2.4.2   Uranium Bearing Aerosols and their Significance in Nuclear Forensics

Isotopic analysis of micrometer sized uranium bearing particles, released from nuclear facilities, has been proven to be an efficient tool for safeguard purposes. Because particle isotopic and elemental compositions are representative of the original material, these isotopic and elemental compositions can be considered as fingerprints of specific processes of the nuclear industry (Fauré *et al.*, 2014).

Particulate matter collected at both established nuclear facilities and locations suspected of clandestine nuclear material handling, play a critical role in nuclear forensics. The method of analyzing for the presence of uranium and its isotopic composition in such particles is important. This is because the particles are representative of the original material and their composition provides specific information about their source. The released particles are highly mobile and can be found in many locations at a nuclear facility (Ranebo *et al.*, 2010).

Swipe samples are taken at e.g. enrichment facilities to ensure that the levels of enrichment remain within the declared values. If a facility would start to produce higher enrichments, it is essential for the safeguard regime to have an early detection. This requires both timely analysis and the ability to find traces of more highly enriched material production in a background of material with lower enrichment.

Fauré *et al.* (2014) used secondary ion mass spectroscopy (SIMS) to analyze the quantity of uranium in uranium bearing aerosols. The aerosols were collected on cotton swipes and analyzed to detect the undeclared nuclear activity. In the research, authors observed that SIMS was efficient in that it enables one to perform isotopic analysis.

Although a lot of research has been done on utility of aerosols in nuclear forensics, most is limited on using SIMS (since it can work both in the microscope and microprobe mode) and SEM (as a conventional technique to do morphological characterization through mapping). Some work has been done on the use of Raman spectromicroscopy and but not when coupled with chemometrics and for quantitative analysis. This work aimed at filling this gap by utilizing laser Raman microspectroscopy in combination with chemometrics to achieve more rapid, direct and comprehensive quantitative nuclear forensic analysis and attribution of aerosols which is vital in nuclear security (and safeguards).

2.4.3 Typical Uranium Concentration in Aerosols and other Matrices

The radiological and chemical properties of depleted uranium can be compared to those of natural uranium that is universally present in soils at typical concentrations of 3 ppm (Bleise *et al.*, 2003). However, as it has been discussed in sub section 1.4.1, the levels of uranium can be elevated/ enriched due to human activities or in the case in high background radiation areas. Using neutron activation analysis, Ramli *et al.* (2005) found the concentration of uranium in air to be 0.076ppm, 4.9-40.4 ppm in soil and 0.33 -1.4 ppm in water. This research was done in the City of Palong in Malaysia, a high natural background radiation area. Baranwal *et al.* (2006) used portable pulsed Geiger Muller counters studies done in Orissa India (the most recently discovered HBRA),and found the concentration levels of uranium to be 33-95 ppm in soil and 312- 1434 ppm in granitic rocks. However, nothing was mentioned on the relative concentrations of uranium in the ambient air.

After the Gulf War in Kuwait, studies were done to determine the concentration of uranium in different environmental samples. The average concentrations of uranium in soil samples were

found to be 1.3-2.5ppm which is below the world average of 3 ppm (Bem and Bou-Rabee, 2004). However, the concentrations in solid particulate matter was 0.024 ppm which is higher than the world average of 0.001 ppm. This was as a result of the high dust concentration of air in that region (Bem and Bou-Rabee, 2004). Table 2.1 gives a summary of uranium concentration in different matrices such as NORM and from a high background radiation areas.

Table 2.1: Concentration levels of uranium in different matrices

Matrix	Normal average concentrations (ppm/ppb)	Elevated levels from HBRAs(ppm/ppb)
Soil	0.1-20 ppm (Veiga *et al.*, 2006)	4.9-100 ppm (Ramli *et al.*, 2005)
Rocks	50-300 ppm (Bem and Bou-Rabee, 2004)	312-1434 ppm (Baranwal *et al.*, 2006)
Surface water	0.03-2.1 ppb (Nriagu *et al.*, 2012)	330 ppb-1.4 ppm (Veiga *et al.*, 2006)
Ground water	0.003-2.0 ppb (Nriagu *et al.*, 2012)	330 ppb-1 ppm (Oeh et al., 2007)
Air	0.02-0.4 ppb (Loosmore and Cederwall, 2004)	24-300 ppb (Bem and Bou-Rabee, 2004)

Little research has been done on quantifying uranium in aerosols in atmospheres impacted by nuclear activity using Raman microspectroscopy.

2.5 Modelling of Aerosol Simulates

The task of modelling a reproducible, size-controlled aerosol particle that has specific concentrations of the analyte of interest from the laboratory is daunting. More challenging is to prepare a calibration standard when dealing with very low sample volumes that carry very low concentrated solutes (Fittschen *et al.*, 2006). There already exist techniques that are commercially available and have been used to make calibration standards for quantitative purposes. A vibrating orifice aerosol generator makes use of a piezoelectric cylinder that accurately controls the breakup of the liquid jet into monodisperse microdroplets. Davies *et al.* (1994) came up with a development program which applied two particle generation techniques; a vibrating orifice aerosol generator (VOAG) that involved evaporation of monodisperse liquid solution droplets and a generator that uses dry powder as the feed material. The technique however failed to have a good calibration and appeared to be very sophisticated (Steinfield, 1998). The advantage of VOAG though, is that it produces monodisperse particles (Knott *et al.*, 2014; Ranebo *et al.*, 2010).

However, a vibrating aerosol generator is quite expensive. Commercial inkjet printers have also been used to generate aerosol and micro particles. Udey *et al.* (2013) modified printers and cartridges to enable printing multiplicity of solutions and collecting and analyzing the printed droplets. The printers also needed an aerodynamic particle sizer and aerosol instrument manager software. Fittschen *et al.* (2006) used an ink jet printer to generate pico- droplets as a technique for deposition of standard solutions for aerosol analysis. Calibration by use of volumes of 130 µl was found to give monodisperse aerosol particles that were efficient in the determination of trace elements. The procedures that involved designing the aerosol generator using the ink jet printer therefore seemed very tedious and at the same time expensive. In this thesis (as will be described in Materials and Methods section), drop coating deposition technique was utilized by making

suspensions on an aluminium substrate. This method saves time and requires very small volumes besides making it possible to analyze very low concentration levels.

3   THEORETICAL BACKGROUND

3.1   Chapter Overview

This chapter discusses both the classical and quantum framework of Raman absorption and emission spectroscopy by considering the molecular vibrations and how to interpret the Raman spectra. Finally, a brief summary is given of chemometric techniques with focus on PCA, ANN and MCR.

3.2   Absorption and Emission Spectroscopy

When atoms or molecules emit or absorb radiation, we get information about these atoms/ molecules in form of spectra. This gives rise to techniques such as absorption, emission and fluorescence spectroscopy. In absorption spectroscopy, the radiation that has been absorbed by the sample in question is measured as a function of wavelength.

When light of sufficient energy interacts with a sample, the atoms or molecules get excited and move to a higher electronic energy level. When such light is absorbed, it gives an intensity that can be measured. Such measurements give rise to absorption spectroscopy. At ground state, such molecules or atoms tend to be at the lowest level during room temperature as per the Boltzmann equation 3.1 (Csele, 2004).

$$\frac{N_n}{N_m} = \frac{g_n}{g_m} \exp\left[\frac{-\left(E_n - E_m\right)}{KT}\right] \qquad (3.1)$$

Where m and n represent the ground and excited vibrational energy levels respectively, N_m is the number of molecules in the ground vibrational energy level, N_n is the number of molecules in the excited vibrational energy level, g is the degeneracy while $E_n - E_m$ represents the change in energy

between the vibrational energy levels, T is absolute temperature in kelvin scale while K is the Boltzmann constant.

Since the density of the molecules is high at the ground state, it implies from equation 3.1 that the molecules at ground vibrational state absorbs more light than the molecules at the excited vibrational state. If we measure the light absorbed as a factor of the concentration of a substance at a constant temperature, then the information can be of utility in quantitative analysis of unknown samples of same matrix. This is because an increase in number of molecules increases the intensity of the absorbed light.

Emission spectroscopy on the other hand, just like in absorption spectroscopy occurs when a sample is excited with an energy source that involves a collection of the permissible emission wavelengths owing to the quantum nature of the emitted wavelengths. At times, the absorbed energy can be dissipated without emission of photons. This could be because some substances do not emit light after absorption. Furthermore, when molecules of a substance are excited, they absorb light to different excited states, hence we expect that emission also occurs from different excited states, this however doesn't happen as when molecules interact with an EM radiation they get excited but settle on the lowest excited state as per the equation 3.1. Absorption is similar to emission but in opposite direction.

Plotting spectra of absorption and emission on the same axis will have the two spectra looking similar though this does not happen experimentally. This could be attributed to the fact that the highest excited molecule does not always occupy the lowest excited state. Some molecules are highly excited and thus undergo spontaneous emission hence go directly to the ground state which means there will be no emission of radiation while others will occupy other vibrational states and emit radiation. These are usually shown as small maxima in the spectrum (Demtröder, 2010).

Fluorescence spectroscopy involves using a beam of light that excites electrons in molecules of certain compounds and therefore can be realized in both absorption and emission modes. In absorption, a laser or any light source can be utilized to excite molecules to higher vibrational modes of the excited state as shown in

Figure *3.1*. In fluorescence spectroscopy however, instead of evaluating the absorbed light as is the case in absorption, we measure emission caused by degeneration of molecules or atoms excited by an incident light. The molecules emitted can also occupy different vibrational states and hence result to small peaks in the characteristic spectra. This technique can also be applied in quantitative analysis since the light emitted increases with increase in concentration of the analyte (Csele, 2004).
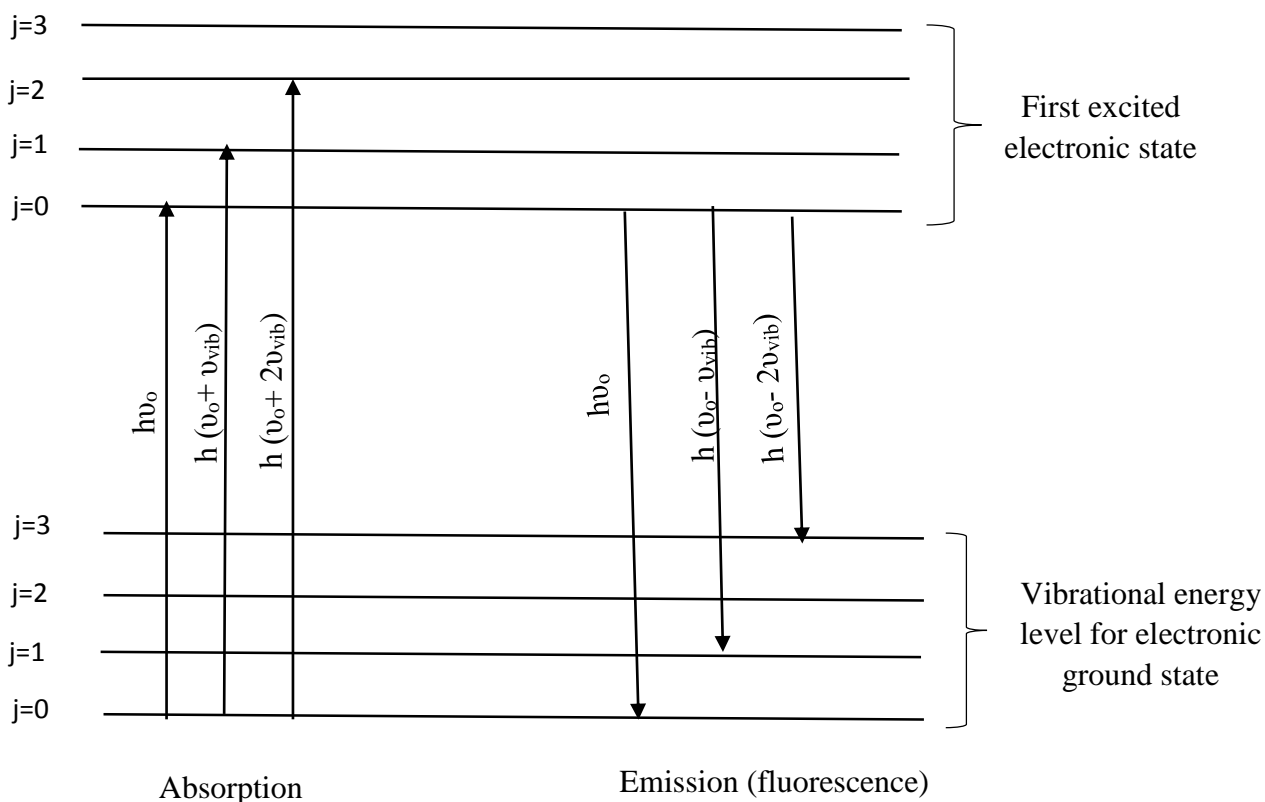
Figure 3.1: Jablosky diagram showing absorption, emission and fluorescence processes(Csele, 2004).

3.3   Classical Raman Scattering

When electromagnetic radiation is absorbed by a sample, the beam will scatter either elastically, inelastically or both processes (Smith and Dent, 2004). This is the principle behind Raman spectroscopy. The EM wave interacts with the sample and causes the electrons in the molecule to be perturbed. The perturbation prompts a dipole moment that oscillates at a frequency (υ) (Demtröder, 2010). Elastic scattering (Rayleigh scattering) happens to be the most intense and most probable type of scattering process. It happens when the frequency of the emitted beam is the same as the incident frequency. In inelastic scattering, the light is emitted at a frequency different from that of the incident beam. This process is also called Raman scattering process. Figure 3.2 shows a schematic diagram of how a sample interacts with light of sufficient energy.
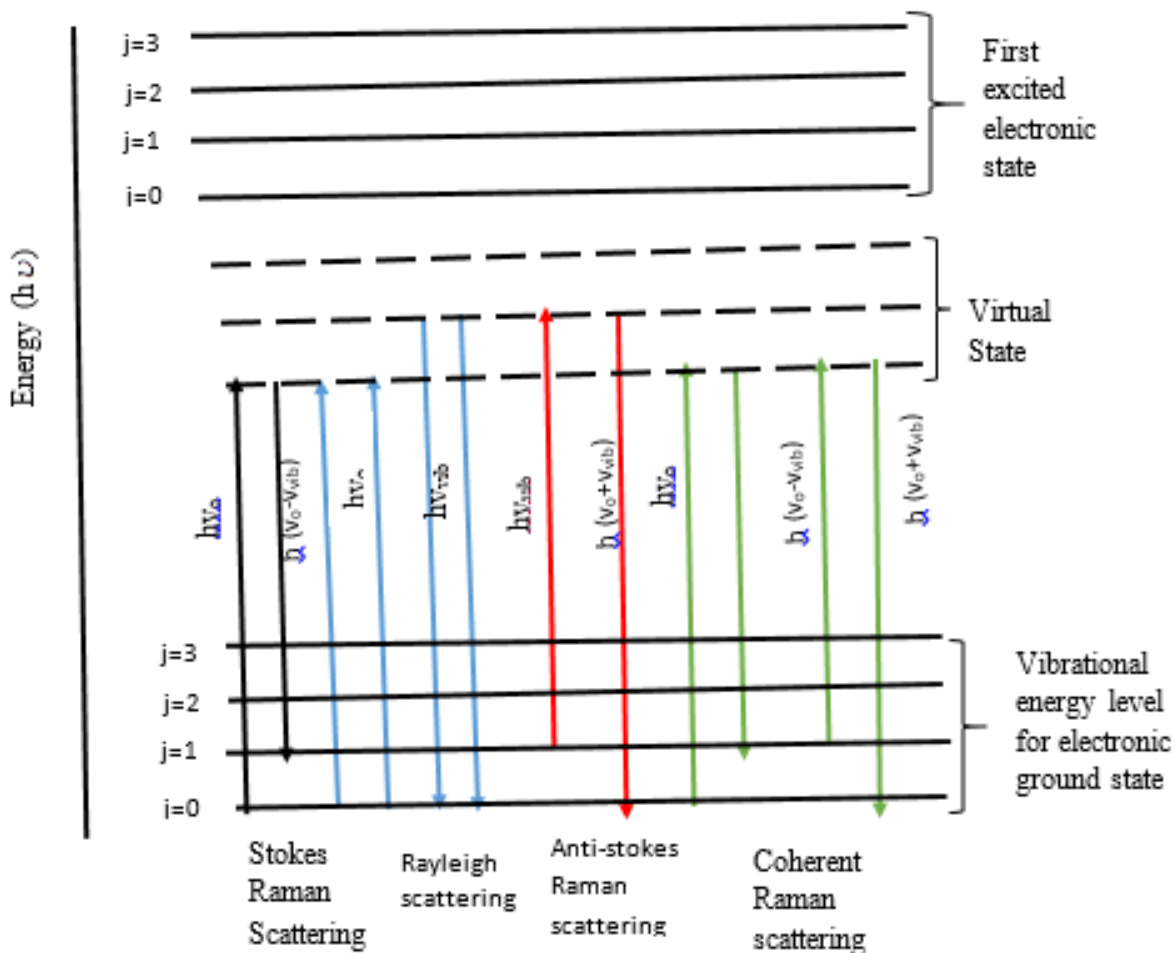
Figure 3.2: Joblonsky diagram showing elastic and inelastic scattering processes (Demtröder, 2010)

The diagram illustrates that Rayleigh scattering experiences no energy lost since the wavelength of the incoming light is the same as one of the scattered light hence it will be a stronger process as compared to the Raman scattering process that experiences loss in energy (Bumbrah and Sharma, 2016).

The incident EM wave induces a dipole moment $P(E)$ during light- sample interaction (Sato-Berrú *et al.*, 2004). The induced dipole can be expressed as:

$$P(E) = \alpha \bar{E} \tag{3.2}$$

Where $P(E)$ is the electric dipole moment, α is electric polarizability and $\bar{E}$ is the electric field which can be expressed as shown in equation (3.3)

$$\bar{E} = \bar{E}_0 \cos \omega t = \bar{E}_0 \cos(2\pi\upsilon_0 t) \tag{3.3}$$

Where υ_o is the incident frequency perturbing the sample, ω is the angular frequency and $\bar{E}$ is the initial electric field. Substituting equation (3.3) into (3.2) we obtain equation (3.4)

$$P(E) = \alpha E_o \cos(2\pi\upsilon_o t) \tag{3.4}$$

The position of different atoms is important in understanding how to perturb the electron cloud of a molecular structure. Molecular bonds make atoms to be restricted to specific quantized vibrational energy levels that have unique modes like the ones in electronic energies and can be expressed as in equation 3.5

$$E_{\upsilon b} = \left(j + \frac{1}{2} \right) h V_{\upsilon b} \tag{3.5}$$

Where $E_{\upsilon b}$ is the vibrational energy of one particular mode, j is the vibrational quantum number, h is the Planks' constant while the frequency of the modes of vibration is given by $V_{\upsilon b}$. If we assume a small change of displacement dQ caused by an energy $E_{\upsilon b}$ from a particular mode of vibration, then the displacement will be given by equation 3.6

$$dQ = Q_o cos(2\pi v_{vb} t) \tag{3.6}$$

Where Q_o represents the highest displacement attainable by an atom from equilibrium position.

The polarizability therefore can be given by a Taylor series expansion of equation (3.7)

$$\alpha = \alpha_o + \frac{\partial \alpha}{\partial \alpha_o} dQ \tag{3.7}$$

Substituting equation (3.6) into (3.7) we obtain equation 3.8 given as:

$$\alpha = \alpha_O + \frac{\partial \alpha}{\partial Q_o} Q_o \cos(2\pi v_{vb} t) \tag{3.8}$$

Consequently the electric dipole in equation 3.4 is given by equation 3.9 that can be further expanded to equation 3.10

$$P(E) = [\alpha_0 + \frac{\partial \alpha}{\partial Q_0} Q_0 \cos(2\pi v_{vb} t)] E_0 \cos(2\pi v_0 t) \tag{3.9}$$

$$P(E) = \left(\alpha_o + \frac{\partial \alpha}{\partial Q_0} Q_0 \cos(2\pi v_{vb}) E_o \cos(2 v_o t) \right) \cos(2\pi v_{vb} t) \tag{3.10}$$

We implore on the trigonometric identity in equation 3.11 that expands 3.10 to 3.12.

$$\cos a \cos b = \frac{1}{2} [\cos(a-b) + \cos(a+b)] \tag{3.11}$$

$$P(E) = \alpha_o E_o \cos(2\pi v_o t) + \left[\frac{\partial \alpha}{\partial Q} \frac{Q_0 E_o}{2} \right] \{ \cos[2\pi(v_o - v_{vb})t] + \cos[2\pi(v_o + v_{vb})t] \} \tag{3.12}$$

The above equation 3.12 implies that the induced dipole moment is affected by two terms; one being responsible for elastic (Rayleigh) scattering (the first term with frequency) while the other term is responsible for inelastic (Raman) scattering. On the other hand, the second term is further divided into two parts with one being upshifted in frequency ($\upsilon_o + \upsilon_{vb}$) causing anti-Stokes Raman and another one being down shifted in frequency ($\upsilon_o - \upsilon_{vb}$) causing Stokes Raman. For Raman scattering to occur therefore, there must be both Stokes and anti-Stokes Raman.

3.4 Quantum Raman Scattering

Different quantized vibrational energy states of molecular vibrational modes as depicted by the Jablonski diagram, determines the Raman scattering process. These discrete vibrational states correspond to the vibrational quantum numbers as explained in equation 3.5 (Dieing *et al.*, 2011).

According to Boltzmann distribution function, at room temperature, molecules will occupy different vibrational states with the ground state (j = 0) being the most populated. The incoming EM wave having energies below the first excited electronic state stimulates molecules to a virtual energy state (Smith and Dent, 2004). Molecules usually occupy ground electronic state but given an incoming radiation, a good portion of the quantum energy that is usually equal to the vibrational mode is shifted to the molecules as shown in **Error! Reference source not found.**.

Elastic scattering involves two types of scattering processes: Mie and Rayleigh scattering. The occurrences of the two depends on the size of the scattering particles. Mie scattering occurs when the wavelength of the light is considerably smaller than the size of the scattering particle. The probability of its occurrence depends on the wavelength of light, particle size/ radius, the absorption ability of the particle and the refractive index of the particles (Dieing *et al.*, 2011).

Rayleigh scattering on the other hand happens when the wavelength of light is much more than the size of the scattering particle. The light's electric field induces an electric dipole moment in the molecule after which the molecule reemits the light in a new direction. The probability of the occurrence of Rayleigh scattering as a function of wavelength is given by $(\frac{1}{\lambda})$ and hence it sturdily increases towards shorter wavelengths.

3.5   Intensity of the Scattered Raman Light

There are many factors that influence the intensity of the Raman scattered light as provided by equation 3.13

$$I = K(v)A(v)v^4 I_o J(v)c \qquad (3.13)$$

Where I is the intensity, K is the spectrometer's spectral response, A is the cross sectional area or the sample size of the analyte, υ is frequency of the exciting laser, I_o is the excitation energy, C is the concentration of the sample in question and J is the molar scattering coefficient.

A Raman spectrum is a factor of intensity as a function of the difference between the excitation frequency and the molecular abundance and bond strength as well as Raman scattered radiation frequency. As discussed before, in classical thinking, Raman power and intensity depends on the polarizability of the molecules, the source of excitation and the concentration of the molecules (Sato-Berrú *et al.*, 2004). The scattering of the Raman intensity is proportional to the fourth power of the exciting energy (Dieing *et al.*, 2011).

Normally for any acquired Raman spectra, the frequency shift for a Raman peak is independent of the wavelength of the excitation light. Since the frequency shifts are always very small (in the

order of $10^{-12}s^{-1}$), the frequency is normally divided by the speed of light to give a resultant quantity as a wavenumber defined as:

$$\Delta\omega = \left(\frac{1}{\lambda_o} - \frac{1}{\lambda_1}\right) \qquad (3.14)$$

Where $\Delta\omega$ is Raman shift which is expressed in wavenumbers, λ_o is the excitation wavelength and λ_1 is the Raman wavelength.

3.6 Vibrations of Molecules

Vibrations that can cause shift in the polarizability of the electron cloud around molecules cause a high Raman scattering intensity. Symmetric vibrations are customarily responsible for the greatest changes and give the intense Raman scattering (Demtröder, 2015). Provided energy is conserved, the energy of a system experiences six degrees of freedom of which three are responsible for the translation of the molecules while the other ones describe the rotational modes of the molecules a part from their linear molecules that have only two rotational modes. This is for the fact that linear molecules have 3N-5 vibrational modes instead of 3N-6 vibrations with N being the number of molecules in an atom (Smith and Dent, 2004).

The modes of vibration for the molecule are a function of the orientation of atoms and bonds, atomic mass and the bond order among other factors. Each mode of vibration is initiated by a specific frequency. The energy of this characteristic vibrations are as result of small number of photons scattered inelastically from a sample and is characteristic of the molecule/crystal.

3.7 Multivariate Chemometric Techniques in Raman Spectroscopy

The International Chemometric Society defines chemometrics as "the science of relating measurements made on a chemical system or process to the state of the system through

mathematical or statistical methods (Lavine and Workman, 2008). Due to the complex nature and the overlapping of the intense Raman bands, it is necessary to use mathematical methods such as data modelling to extract information from such complex data (Palacios and Taylor, 2000). On many occasions, the matrix in which Raman data is obtained, is complex as it is multidimensional. Such matrices provide low signal to noise ratio values that makes direct analysis and by extension quantification a big challenge. By use of chemometrics, it is possible to modify the spectrum to help perform quantification directly using modelling techniques.

3.8 Multivariate Calibration Approaches using ANN

Multivariate calibration methods used in chemometrics have over time been seen to be the most appropriate in overcoming problems associated with classical/univariate analysis of Raman data. The major aim of multivariate calibration is to define the relation that exists between a response y- variable and several variables of x.

Two basic chemometric techniques (PLS and ANN) are the state of the art that have over time been utilized in determining such relationships. Whereas PLS is a powerful multivariate regression method mostly utilized during linear relationships, ANN models utilize both linear and nonlinear relationships multivariately.

Unlike in other techniques that require an explicit understanding of the spectrum, multivariate models have no Raman-specific relations but rather, we establish a relationship between **X** and **Y**. The **X** (**n** x **p**) matrix is the spectral data having n as the measured spectra and p intensities and other spectral features. On the other hand, the **Y** variable is a matrix **Y** (**n** x **m**) m being the concentration of the analyte while n are the samples. Combining the multivariate techniques with Raman spectroscopy provides a synergy for exploratory data analysis.

Research has been done on how Raman spectroscopy can directly do quantification without multivariate techniques by considering the relationship between the intensity of the scattered radiation and the concentration of the analyte (Kneipp *et al.*, 1999). Ideally, a higher analyte concentration is expected to give a higher intensity. It is however more advantageous to use chemometrics since it avoids the difficult procedures of spectral evaluation.

3.9   Spectral Data Preprocessing

Data pre-processing is one of the most important aspects to be considered in multivariate calibration. Data pretreatment is the manipulation of the data before the main analysis (Shah *et al.*, 2007). The main purposes of data preprocessing in analysis of spectral data are:

    i.   To reduce the amount of data through elimination of sources of variation

    ii.   To provide sufficient information within the data to achieve the preferred goal

    iii.   To transform data into one that will be suitable for further analysis

The basic approach to data preprocessing is by data reduction. We construct new set of variables with each containing a sum of weighted original variables. The linear combinations are derived by use of mathematical techniques. Data transformations are applied to change the distribution of values of the variables for example to bring them to the normal distribution.

To achieve equal statistical influence on the data, the values of the input variables are normally scaled column wise through mean centering such that the values of the input variables are scaled to have a mean of 0 and a standard deviation of 1 (Varmuza and Filzmoser, 2016). New data matrix is normally generated that epitomizes the relationship that the data has among themselves. The different pre-processing techniques employed in analysis of data are:

- Smoothing

- Mean centering

- Normalization

After doing optimization for the analytical conditions suitable for Raman analysis, different strategies such as: averaging, smoothing and filtering are employed to reduce noise. The methods are usually applied on the transformed spectral data before any analysis is done so as to avoid unwarranted effects such as saturation caused by different scales and ranges of the initial variables (Brereton, 2003).

3.10 Supervised Learning

The main aim of supervised learning is to establish characteristic relationship models that are based on experimental data so as to determine hidden properties in the experimental data. New samples are then assigned to already defined classes based on their patterns of measured spectral intensities. This is where the multivariate calibration data falls.

Whereas multivariate classification (pattern recognition) assigns objects correctly to a given class e.g. the source of the sample, multivariate calibration aims at developing latent variables for best prediction of a property y from another variable x. For this work, ANN was applied for evaluation of data with the purpose of developing calibration models.

3.10.1 Principal Component Analysis (PCA)

Unsupervised method (one that does not require a training data set) is always the best technique for exploratory data analysis (EDA). One such unsupervised technique is the use of principal component analysis (PCA). It is a way of exploring patterns in data and expressing it in such a way as to bring out their similarities or differences. The main advantage of PCA is that once the

patterns have been found, the data is compressed by reducing its dimensions without much loss of information.

Other than just reducing dimensionality, PCA detects outliers, selects main variables, do pattern recognition and also validation and prediction of samples (Brereton, 2003). The new coordinates called principal components (PCs) are orthogonal to one another. The first principal component called PC1 is always the linear latent variable that has the maximum possible variance. On the other hand the second principal component (PC2) is orthogonal to the direction of PC1 and also has similar minimum possible variance of the scores. Other PCs also follow this rule (Varmuza and Filzmoser, 2016). Based on these properties, PCA can easily be utilized in recognizing the relationship between simulates of different concentration levels and also recognize patterns of field aerosol samples in reference to their sources.

PCA has important features provided in its graphic interface. The graphs include scores, loadings and residuals. The most important feature that provides quantitative information from the PCA are the scores and the loadings. The score plot shows the covariance between samples and detects outliers hence enabling one to draw expected/ unexpected trends from the data. The line plots of the loadings on the other hand demonstrate the significance of the original variables for each of the PC and can be used to construe the quantitative differences that cause the clusters or tendencies in the data. Loadings encompass qualitative information such as identification of molecular bands that are specific to the components within the sample. The loadings are used to describe the structure of the data in terms of different variable correlations in that each variable has a loading on each PC. It will therefore show the contribution the variable made to the said PC and also how the PC responds to the variation of that variable over different data points.

3.10.2 Artificial Neural Networks (ANNs)

ANNs are defined as practical input-output based models suitable for modelling multi-input and multi-output relationships through curve fitting (Liu *et al.*, 1993). Such models contain information that gets distributed over a large number of model parameters that accounts for their great flexibility. The networks mimic the cognitive behavior of human beings and as such they become suitable for processing incomplete and fuzzy data (Liu *et al.*, 1993). Such characteristics cannot be expressed through the well-known classical algorithms but rather they are based on learning experience. Other scientists argue that ANNs can be used to derive solutions to problems that are hard to solve using classical algorithms (Shah *et al.*, 2007).

The ability of ANNs as a tool in modelling for multivariate calibration is well documented. Concerted efforts are now being put together to develop approaches that ensure good conditions for calibration are obtained (Despagne and Massart, 1998). ANNs can be utilized in building empirical multivariate calibration models of the form:

$$Y = F(X) + \varepsilon \qquad (3.15)$$

Where F is the function of the network, $\mathbf{X}$ the matrix of analyte measurements performed on several n samples. $\mathbf{Y}$ is the vector matrix that contains the response of the samples such as the concentration of target analytes and ε is the error in the model prediction. The ANNs operate on the following principle: each neuron receives several inputs that are vigorously weighted, then the weighted sum of its input are then biased again against a given threshold level. The network finally applies a nonlinear function to compare the output. The neurons assigned in to the network are arranged in layers.

For purposes of calibration, the network optimizes the weights as a function of the difference between the predicted and the real values of the concentration of the analyte in the sample in question. Chen and Billings (1992) state that the ability of the network to predict unknown samples is therefore derived from its set of validation.

3.10.2.1 Back Propagation Networks (BP-ANNs)

Neural networks can be thought of as being related to artificial intelligence. Such networks are best suited in solving problems that have proved to be difficult in solving using traditional computational methods. As seen from Figure 3.3, the neuron network works as follows: Each neuron receives a signal from other preceding neurons in the previous layer whereby the signals are multiplied by a separate weight value.

The weighted inputs are summed and then passed through a limiting function that scales the output to a certain fixed range of values. The output is then displayed to all of the neurons in the next layer. For one to solve a problem using the network, we apply the values of the input to the outputs of the first layer, allowing the signals to propagate through the network and then read the output values.
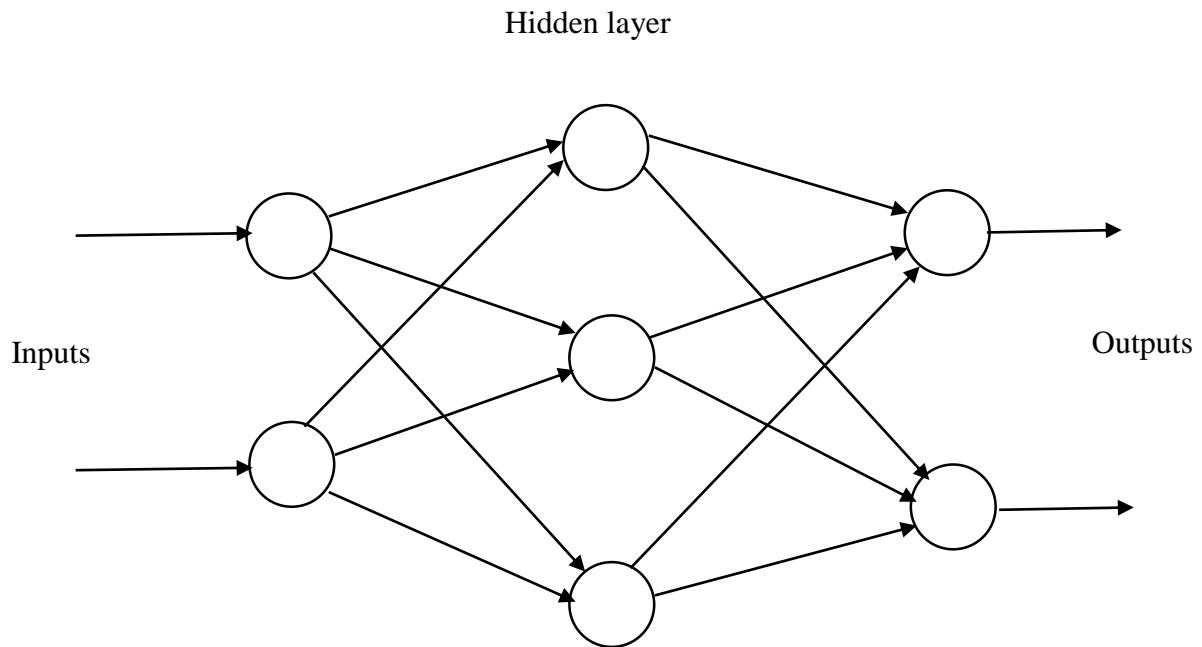
Hidden layer

Figure 3.3: A generalized schematic of the BP-ANN (Ilonen et al., 2003).

From the generalized network, stimulation is applied to the inputs of the first layer and the signals propagate through the hidden layers to the output layer. The link between neurons has a unique weighting value.

Figure 3.4 shows the structure of a neuron and how the inputs are weighed before passing the output value to the next neuron.
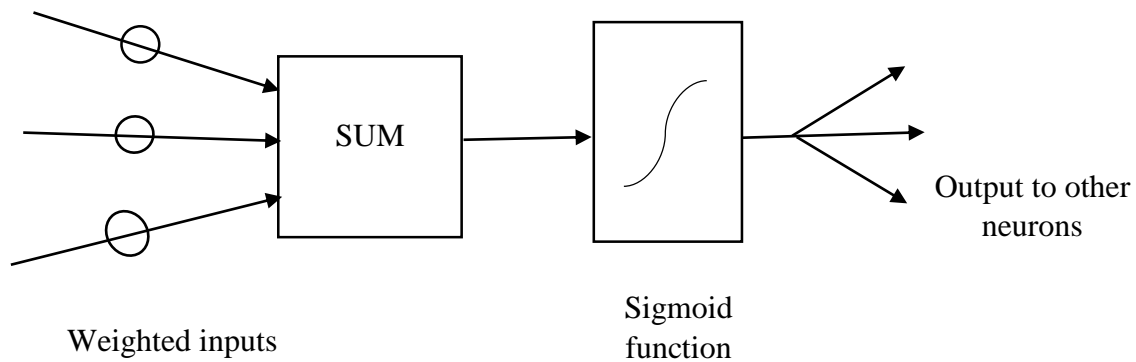
Figure 3.4: Schematic structure of a neuron (Ilonen et al., 2003).

From the structure of a neuron; inputs from one or more previous neurons are weighted individually and summed. The result is scaled between 0 and +1 non- linearly and the output value is passed on to the neurons in the next layer.

The values of the weights between neurons provides the real 'intelligence' of the network. Therefore, there has to be a way of adjusting the weights to solve a given problem. Such a type of network needs the Back Propagation algorithm. The algorithm learns by example such that there has to be a learning set that has some input examples and the known- correct output for each case. The input- output examples show what type of trend is expected of the network and the BP algorithm allows the network to adapt (Varmuza and Filzmoser, 2016).

The training is however an iterative process such that one of the example cases is applied to the network that produces some output based on the current state of the synaptic weights giving a random output. The output is compared to the known values, and a mean squared error signal is calculated. The error value is propagated backwards through the network and small changes are made to the weights for each layer to reduce the error signal. The cycle is repeated to ensure that

the overall error value drops below a predetermined threshold. At this point the network is said to have learnt the problem hence it can be applied to practical problems.

3.10.2.2   Cascade Correlation Neural Network

Cascade correlation is a supervised algorithm for artificial neural networks. Unlike in BP-ANNs which just adjusts weights in a network of fixed topology, CC starts with a minimal network after which it automatically trains and adds new hidden units one after the other hence creating a multi-layer structure (Hettinger *et al.*, 2017). After a new hidden unit is added to the network its weights in the input-side are frozen. The frozen unit becomes a permanent feature – detector in the network available for producing outputs or creating some more complex feature detectors.

Some of the documented advantages of cascade correlation over other algorithms is that it learns very fast. It retains the structures it has built or developed even if the training set changes. The algorithm also requires no backpropagation of error signals through the connections of the network (Fahlman and Lebiere, 1990) as shown in Figure 3.5.

Cascade correlation combines two major ideas: the first being the cascade architecture, in which hidden units are added to the network one after the other and they don't change after they have been added. The second idea is that the learning algorithm, creates and installs the new hidden units. For every hidden unit, the network attempts to maximize the magnitude of the correlation between the new unit's output and the residual signal error that needs to be avoided. The algorithm begins with some inputs and one or more output units without any hidden units. Every unit however, is connected to every output unit by a connection having an adjustable weight. The bias input is always set to +1.
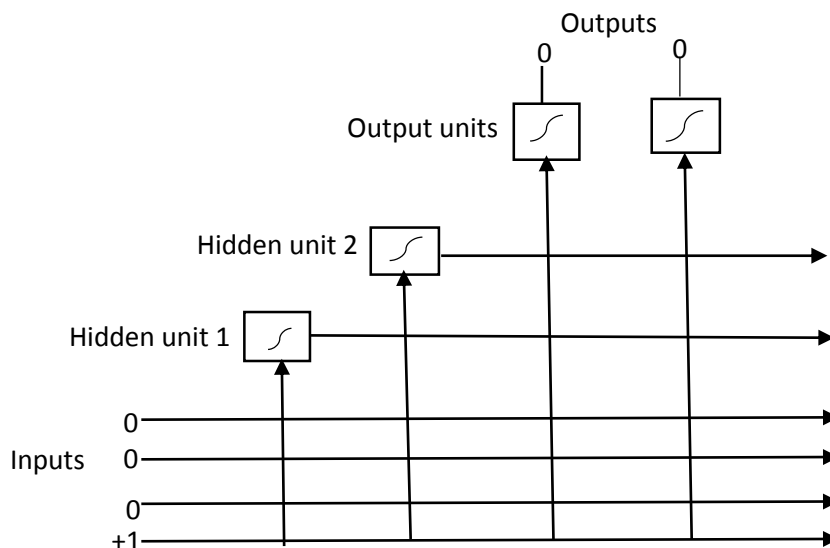
Figure 3.5: Schematic of Cascade correlation architecture after two hidden neurons have been added (Fahlman and Lebiere, 1990).

The output units may yield a linear sum of their weighted inputs or rather employ nonlinear activation function.

3.10.3 Multivariate Curve Resolution

Characterization of the chemical composition of individual aerosol PM aids in understanding the sources and transport of atmospheric aerosols. The challenge however is in getting analytical techniques that can provide the molecular, etc. information of the particle. Raman microspectrometry combines the capabilities of Raman spectroscopy that has an optical microscope that provides a solution for obtaining molecular information on particles at microscopic levels with *in situ* situations (van Drooge and Grimalt, 2015).

A Raman image provides many pixel Raman spectra that are characteristic of the complex mixture at levels of individual aerosol particles. The heterogeneity of such particles cannot be resolved by spatial resolution of the instrument that suffers from optical diffraction hence the need to employ multivariate curve resolution (Sobanska *et al.*, 2006).

MCR recovers the pure response profiles of the chemical constituents or species of an unresolved mixture when no prior information is available about the nature of the composition of the mixture (Stanimirova *et al.*, 2011). It is mostly applied to multicomponent systems like spectroscopic images. To apply MCR to a multicomponent data, the two steps involved are: one can structure the experimental data as a two way data matrix or multiset structure; and the data set can be reasonably explained by use of a bilinear model using a limited number of components. The bilinear model is normally expressed as:

$$D = CS^T + E \qquad\qquad (3.16)$$

 where $\mathbf{D}$ is the raw data set of the spectra, $\mathbf{C}$ is the concentration profiles for each of the compounds, $\mathbf{S}$ is the matrices of the pure spectra while $\mathbf{T}$ are the small matrices of the bilinear model that contain profiles of the pure contributions (species, compounds) of the original data set.

A hyperspectral image can be described as a 3D data cube having a matrix of image pixels as spatial data points described as $\mathbf{X \times Y = M}$ and W spectral data points (wavenumbers). The image is normally unfolded into a matrix to be input for MCR-ALS using specified number of components N. The unfolding of the matrix results in two matrices: C and S^T where C is an N x M matrix whose every row has the spectra of a pure component. C is used to construct segmentation maps and corresponding centroid profiles. The segmentation maps are based on number of clusters (K) that describe chemically unique zones in the sample. The centroid plot on the other hand describes the contributions of different pure components. Figure 3.6 shows schematic of MCR-ALS analysis on a sample.
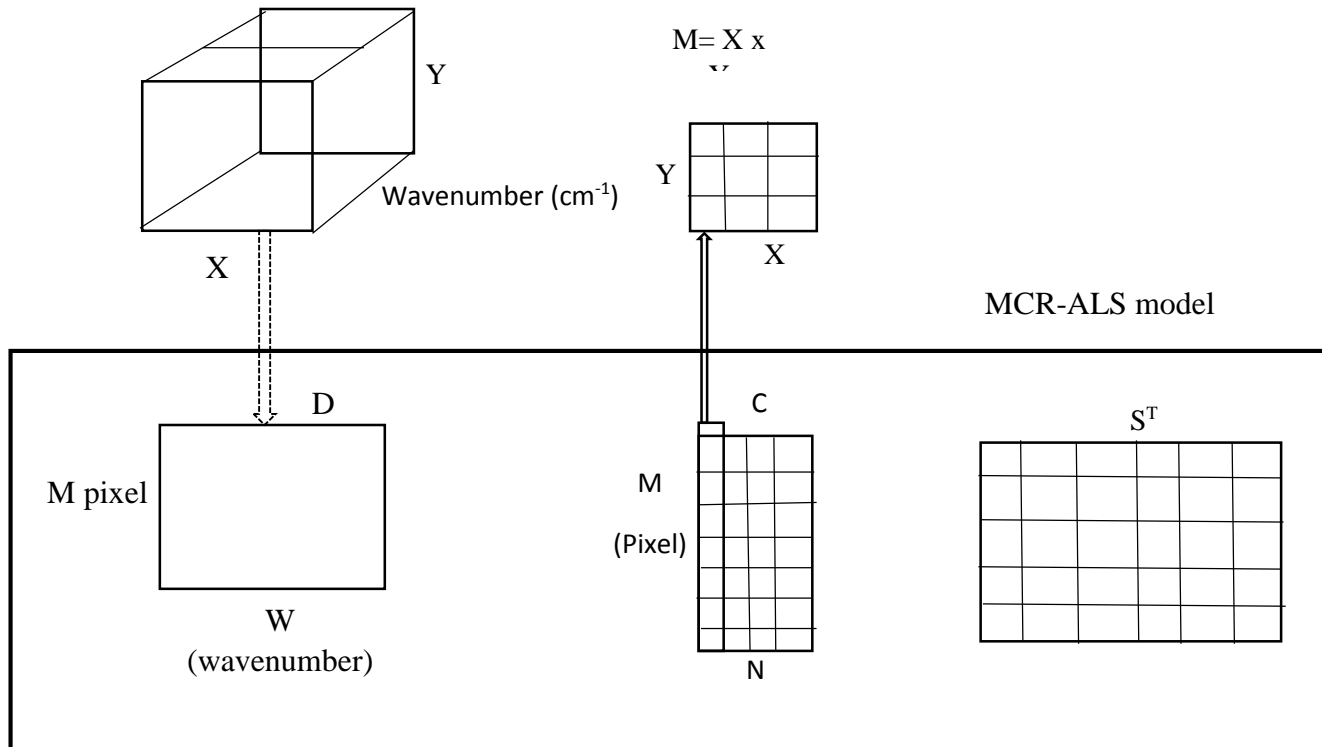
Figure 3.6: Schematic of MCR-ALS (Vosough et al., 2015).

Using MCR-ALS the **C** matrix will give the spatial distribution of uranium in the aerosol particles at each pixel while S^T gives the resolved spectral profile of the Raman spectra obtained using ALS constraints.

4 MATERIALS AND METHODS

4.1 Chapter Overview

The application of Raman microspectroscopy for quantification of uranium in simulate samples has been investigated using calibration models developed for its specific vibrational and rotational bands. The spectra were obtained at 10 s exposure time and wavelength centered at 1050 cm^{-1} to cover the fingerprint spectral region of uranium compounds which is between 400 and 1500 cm$^{-1.}$

The calibration models were validated using a synthetic uranium standard developed based on IAEA-RGU-1 which a uranium standard is diluted with floated silica powder. The concentration of uranium in the standard is 400 ppm with 95% confidence level (attached certificate in Appendix 5). However, in making the synthetic standard, the uranium concentration was diluted to 100 ppb (within the range that it is expected in typical aerosols) before validation. All chemicals used in the sample preparation were of analytical grade. The procedures used in preparation of simulates and the methodologies in training, validating and testing the developed model are presented and discussed.

4.2 Raman Spectromicroscopy Instrumentation

The instrumentation for this study consisted of confocal laser Raman Spectrometer (STR Raman Spectrum, Seki Technitron` Corp, Japan) equipped with a 300 mm imaging triple grating monochromator spectrograph with two lasers exciting at 532 nm and 785 nm. The 300 mm imaging spectrometer was equipped with 1800, 1200, 600-lines/mm grating and a backscattered-illuminated CCD camera for acquiring spectra within optimized time frames. Before any measurements were taken, the instrument was calibrated daily using a standard silicon wafer and the Raman scatter bands maintained at 520.5 cm^{-1} as shown in Figure 4.1.
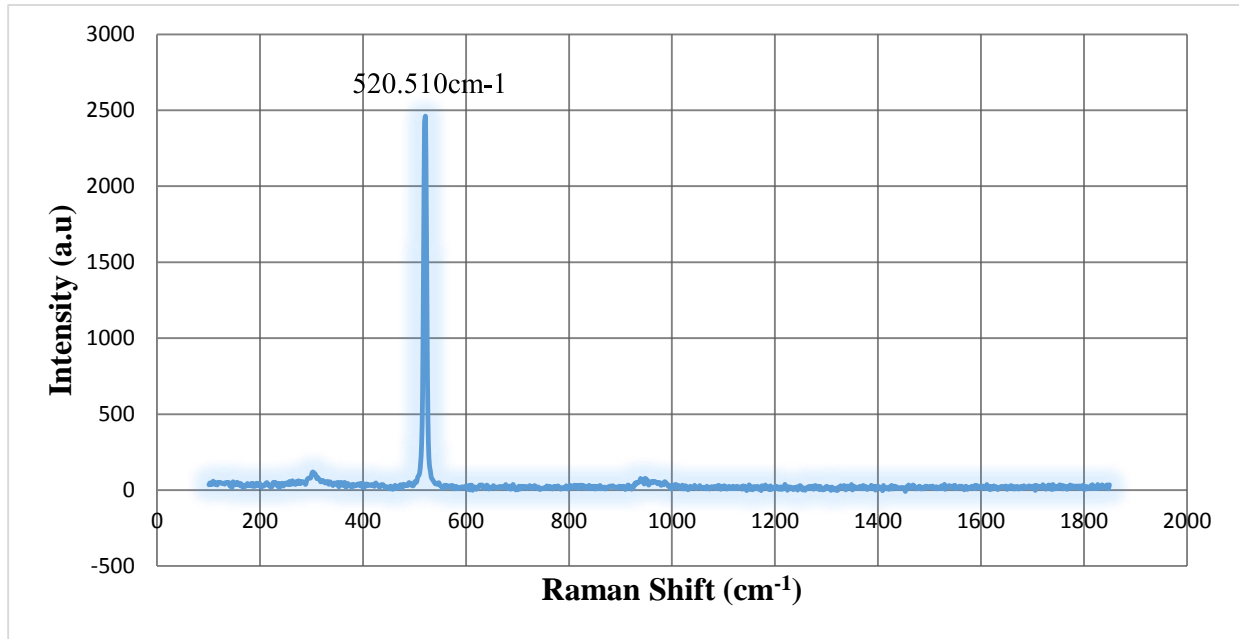
Figure 4.1: Raman spectrum of silicon wafer using 785 nm laser.

During measurements, either 785 nm laser was used or manually switched to 532 nm. Normally, a beam of either the red or the green laser light was delivered to the Raman optics through an optical fiber that gives the beam total internal reflection. Thereafter, the shutter then delivers the beam to the band pass filter of the laser being used. The band pass filter then conveys the beam of light to the beam splitter that splits it into two equal parts with 50 % being reflected and the other 50 % passing through the beam splitter to the sample enabling scattering as in Figure 4.2. All the measurements were taken in dark room to avoid background contribution due to fluorescence.
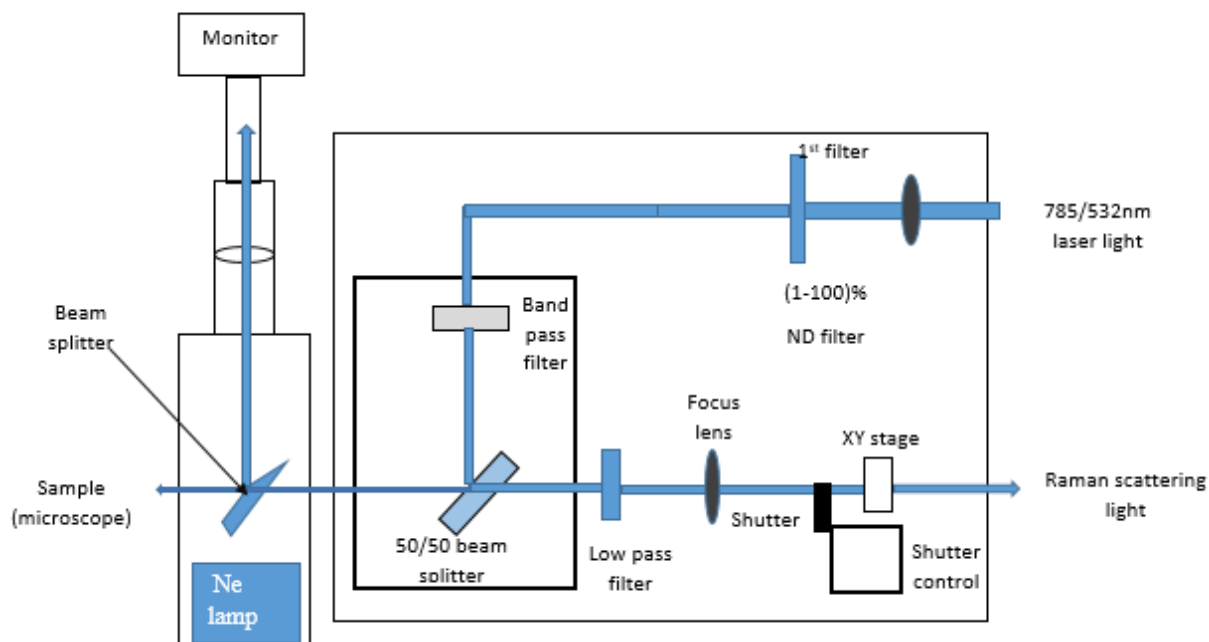
Figure 4.2: Basic Raman set up schematic (Technotron Corp Raman spectroscopy Manual 2012).

To control the movement of the focused laser spot on the screen, the set up was equipped with a microscope that uses a lever to regulate the motorized stage. Depending on the nature of the sample (either opaque or transparent), the spectrometer has two switches that enable one to observe the sample using light from above or below the sample.

Once the sample has been excited, the scattering of the weak Raman signal is measured by use of imaging spectrometer and CCD camera. Focusing of the sample was done by use of a motorized stage, the computer that is equipped with STR software and a microscope with a camera for visualization. The stage which was motor-driven helped in scanning across the sample and collecting data on specific uranium particles on the aluminium foil substrate.

4.2.1 Optimization of Raman Spectrometry Measurements

Optimization of the spectral window to be used depends on the region where most vibrational bands of the sample occur. The Raman spectrometer used in this study was equipped with a shift of 1800, 1200 and 600 lines/mm spectral windows. For this analysis, the grating window was set between (100-2000) cm^{-1} since this is the region where most Raman bands for most uranium compounds occur.

The excitation laser light intensity was controlled by use of neutral density filters that are equipped with different attenuators as shown in Table 4.1 below. The spectrograph was set at 256 X 1024 pixel CCD camera. The Orion Laser Power meter from Ophir photonics was used to measure the laser powers at different transmission intensities before and after the filter.

Table 4.1: Power of different lasers at different objectives

Objective	Numerical Aperture	Power to sample		Laser Spot size	
		785 nm (mW)	532 nm (mW)	785 nm (μm)	532 nm (μm)
X10	0.30	18.20	6.00	68.47	10.02
X20	0.45	17.02	5.33	33.34	5.76
X50	0.50	8.52	5.60	14.60	1.56
X50	0.80	11.74	5.02	12.76	1.77
X100	0.90	6.34	4.70	6.02	0.625

From equation 4.1 below, it implies that the 532 nm laser has a higher spatial resolution than 785 nm laser.

$$LSD = \frac{1.22\lambda}{NA} \qquad (4.1)$$

Where LSD is the laser spot diameter and NA is the numerical aperture. For simulate samples, 10 Raman spectra were acquired from the Coffee Ring at 5 different equidistant spots. The 50 spectra were then averaged in order to obtain a single spectrum. For each spectrum, the exposure time was set at 10 seconds.

Another factor considered in optimization was the SNR of the uranium-specific band. Several sets of number of accumulations and accumulation times were obtained to show which set gives the highest signal to noise ratio for both lasers. The SNR was calculated from the equation (4.2) (Carranza *et al.*, 2003).

$$SNR = \frac{I_p}{I_n} \qquad (4.2)$$

Where I_p and I_n refer to the intensity of the main band and the average intensity of ten adjacent small peaks that appear as noise. Since in Raman spectroscopy we talk of a band and not just a peak, such intensity was obtained (after a Gaussian fit) as the area under the said bands to be equivalent to the intensity.

4.3 Automated Scanning Raman Microspectroscopy

Field aerosol samples with cut size of 3.2 μm were subjected to Raman mapping coupled with multivariate curve resolution with the aim of recovering and giving a spatial as well as structural distribution information and interpretation of uranium in individual aerosol particles. Confocal

Raman spectrometer equipped with an Olympus x100 objective with numerical aperture of 0.9 was used. An equipped camera was used to feed the signal to a video monitor hence providing an optical view of the samples. A neon cooled CCD (2048 X 512 pixels) was utilized for detection. The microscope stage was XYZ-motorized for point by point scanning with a resolution of 625 nm using the 532 nm laser.

4.4 Preparation of Calibration Standards

One basic requirement in preparation of a calibration standard is that it should mimic the real sample as much as possible. The factors to consider are: (i) the embedding matrix should be as close to the real sample as possible and (ii) they should be homogeneous.

Reproducing monodisperse aerosol particles proved to be a daunting task besides the challenge of simulating uranium bearing particles without dissolving the uranium in a solvent (as aerosol particles are derived from gas/air and not liquid).

This work therefore employed the idea of Drop Coating Deposition Raman (Jiang *et al*., 2017; Bhandari, 2011) which is a technique that is highly reproducible and sensitive in obtaining Raman spectra from an analyte at very low concentrations. In this technique, an aliquot is dropped on a substrate and allowed to dry (using an oven or hot plate) and the spectra acquired from the Coffee Ring created normally after drying.

For this work different uranium concentration aliquots were micro-pippeted on a substrate and left to dry on a hot plate in a clean room to form a suspension. This technique though, did not produce monodisperse aerosol particles as shown in Figure 4.4.

Uranyl nitrate standard was mixed with analytical grade salts that embodies the main background anions in which uranium is embedded in aerosol particles. These include sulphate based uranium mineral zippetite, carbonate based uranium mineral andersonite, or phosphate based uranium mineral autinite. Since all salts used in this study were soluble in distilled water, de ionized water was used to homogenize all the particles into one soluble matrix. The process of making simulates involved making uranium stock solution and doing serial dilutions downwards using the serial dilution formula as shown in equation 4.3.

$$C_1 V_1 = C_2 V_2 \qquad (4.3)$$

Where C_1 and V_1 refers to the concentration of the stock and expected volume to be taken from the stock respectively while C_2 and V_2 are the expected concentration and the maximum volume in the beaker respectively. Figure 4.3 shows the steps followed in making the calibration standard.

The weights were measured carefully using a measuring balance whose sensitivity was 0.0001 g. The chemical compound was diluted to a volume of 10 ml in a 50 ml plastic beaker which was mixed using a magnetic stirrer to ensure complete homogeneity of the sample. For analysis purposes, 2 µl of the solution was micro pipetted on the substrate for analysis. The aliquot drop on the substrate made a suspension after drying. A summary of how the stock solution and other concentrations were made is in Appendix 6.

Stock solution (1500 ppm uranium)

100 ml of base matrix solution

Volume micropippeted to a beaker

Corresponding volume to a beaker

Total volume (Stock + base matrix)

Micropipette (1-1000µl)

Coffee Ring from the dried drop

Drying drop on a substrate (2 μl)

Hot Plate
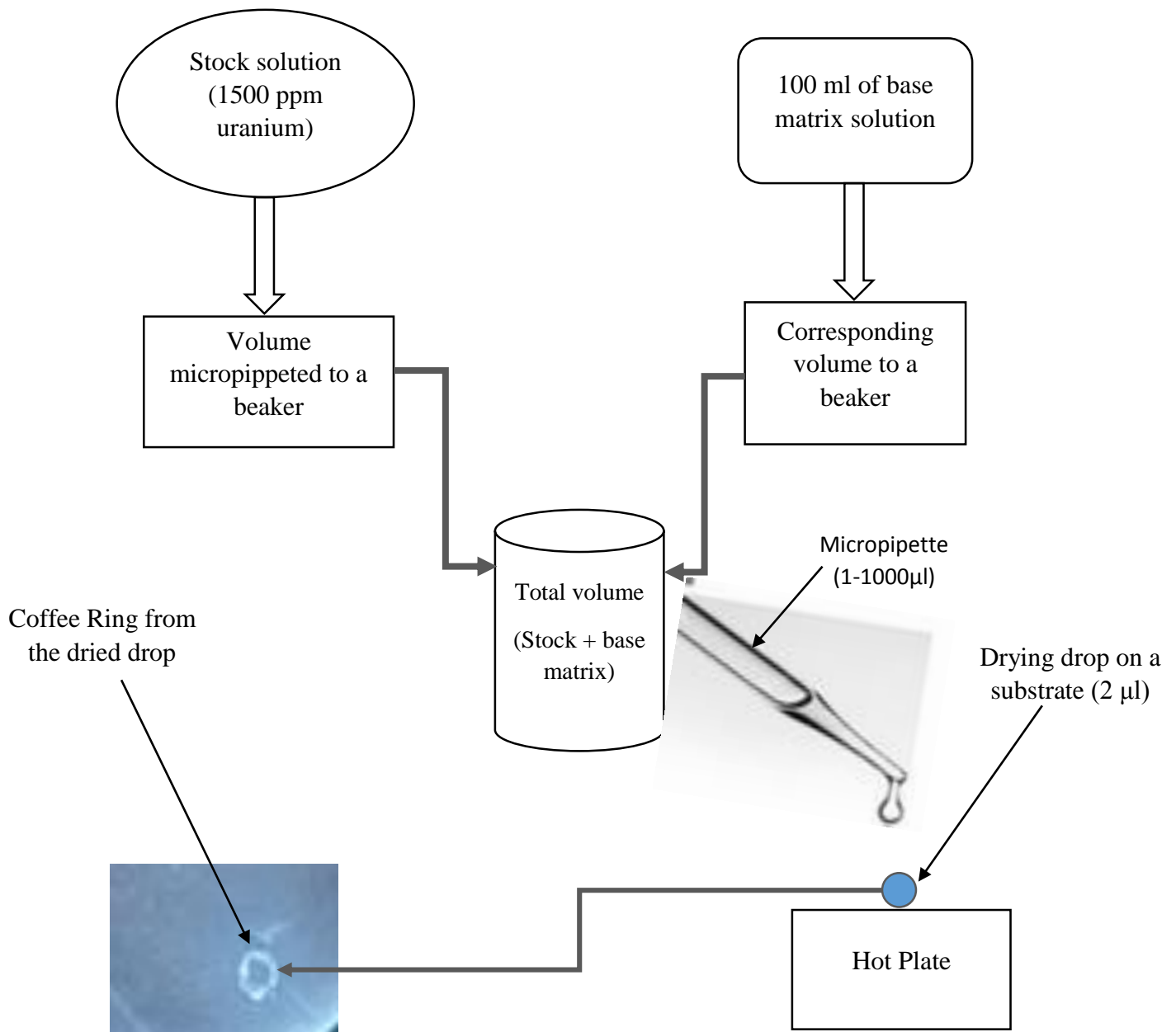
Figure 4.3: Schematic of the sample preparation procedure.

The typical matrix composition of simulates expected on the substrate would be the different anions that made the background matrix i.e. NO_3^{2-} (from ammonium nitrate salt), SO_4^{2-} (from the copper suphate salt), Cl^- (from sodium chloride salt). These anions form the basis through which

uranium is mostly expected to be embedded in the particulate matter from the field. The particles generated were however not monodisperse since at one point they agglomerated together during nucleation process. Figure 4.4 shows a typically simulated aerosol particles containing 10 ppm of uranium on a substrate.
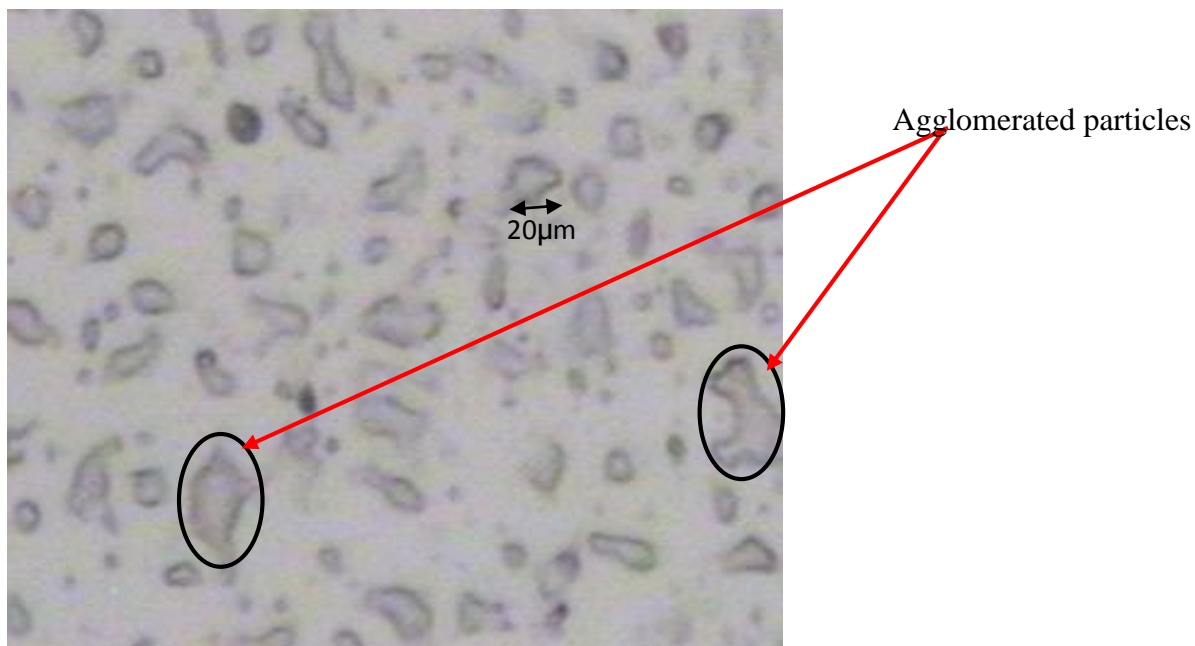
Figure 4.4: Photomicrograph of typical aerosol simulate having 10 ppm of uranium as observed in Raman using X50 magnification.

4.5   Preparation of a Synthetic Standard

A synthetic standard for uranium was made using certified reference material IAEA-RGU-1 as described in appendix 5. This was because, getting a laboratory standard of particulate matter having low levels of uranium deposited on the same substrate we used (aluminium substrate) for analysis was difficult. The RGU-1 had 400 ppm levels of uranium as per the certificate in Appendix 5.

However, since the RGU-1 uranium ore standard had no anions that embodies typical uranium bearing aerosol particles as was in the field particulate matter, there had to be a way of introducing these anions as part of the matrix. Furthermore, the uranium concentration had to be diluted to lower concentration of 100 ppb to comply with the concentration ranges in which the neural network was trained as well as the levels expected in aerosol particles. Based on these two reasons, analytical grade salts similar to ones used in making simulate samples i.e. sodium chloride (0.5 g) to provide chloride ions, copper (ii) sulphate (0.25 g) to provide sulphate ions and ammonium nitrate (0.25 g) to provide nitrate ions were used as embedding anions. These salts were dissolved in 10 ml double distilled water. 0.1g of RGU-1 (which is still equivalent to 400 ppm) was then put in a small beaker. Finally, 4 ml of the salts that were dissolved in distilled water was micropippeted and added to the beaker containing RGU-1 solid powder. Ideally, this reduced the concentration to 100 ppm. This concentration was diluted further using the serial dilution formula and as explained in appendix 6 to obtain 100 ppb. The final step involved micropippeting 2 µl of the homogeneous solution onto an aluminium substrate and left to dry on a hot plate so as to make a suspension as shown in

Figure 4.5 .
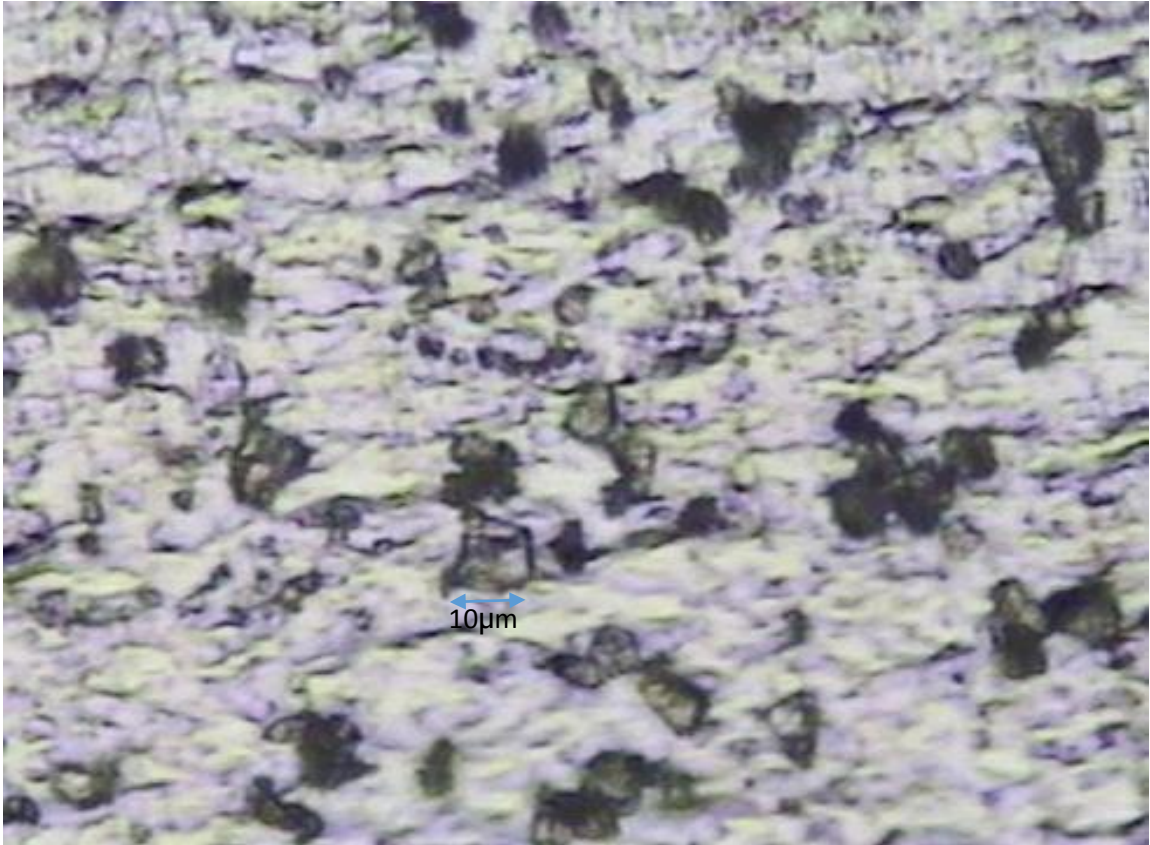
Figure 4.5: Pictograph of RGU-1 suspension on an aluminium foil substrate at X50 objective.

The Raman scatter bands associated with uranium molecules based on both 785 nm and 532 nm laser is as shown in Figure 4.6.
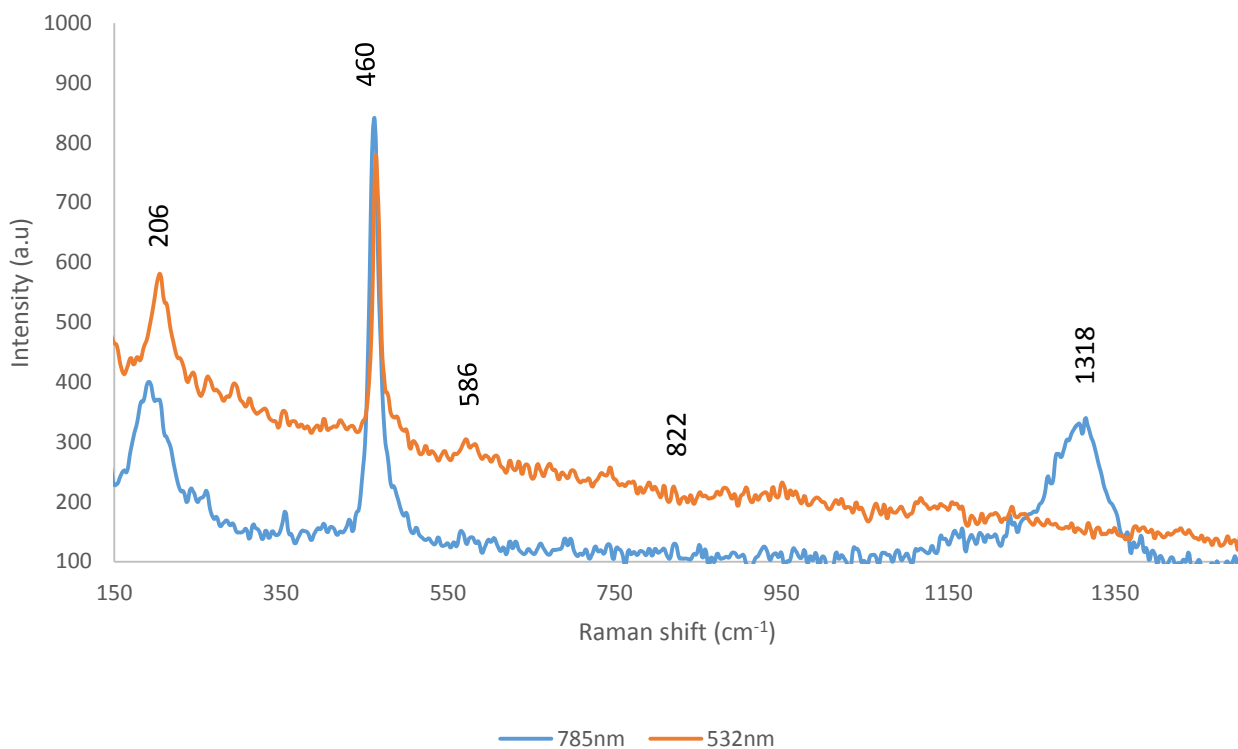
Figure 4.6: Raman spectra of RGU-1 synthetic standard using both 532 nm and 785 nm lasers.

From Figure 4.6, specific Raman scatter bands can be assigned as 206 cm^{-1} and 460 cm^{-1} for uranium attached to a chloride. However, owing to the very low uranium concentration in the synthetic standard (100 ppb) it is not surprising most of the Raman scatter bands associated with uranium (mainly between 810 and 870 cm^{-1}) are almost buried in the background.

4.6   Aerosol Sampling

Particulate matter from eight zones of South Coast Kenya which is classified as High Background Radiation Area (HBRA) were collected using low volume (2L/min) six stage cascade impactor aerosol sampler (Model 135 MiniMOUDI^{TM}) from MSP Corporation USA. In the vicinity of the sampling site, there is also titanium mining therefore we expect to have TE-NORM hence

enrichment of uranium in the ambient aerosols. The aerosol particles were sampled by tying the sampler on trees or on roof tops depending on the sampling location. Samples from the roof top of Physics Department (University of NAIROBI) herein referred to as Chiromo roof top about 525 km away from the sampling regions were used as the control.

Kwale County and particularly areas around Mrima Hill have been documented as having high levels of radioactivity, (Achola *et al.*, 2012; Mangala, 1987; Chege *et al.*, 2013). Sampling was done for five days (18th December 2016 to 23rd December 2016.) The sampling areas were as shown in the Figure 4.7 with the latitude and longitude positions.
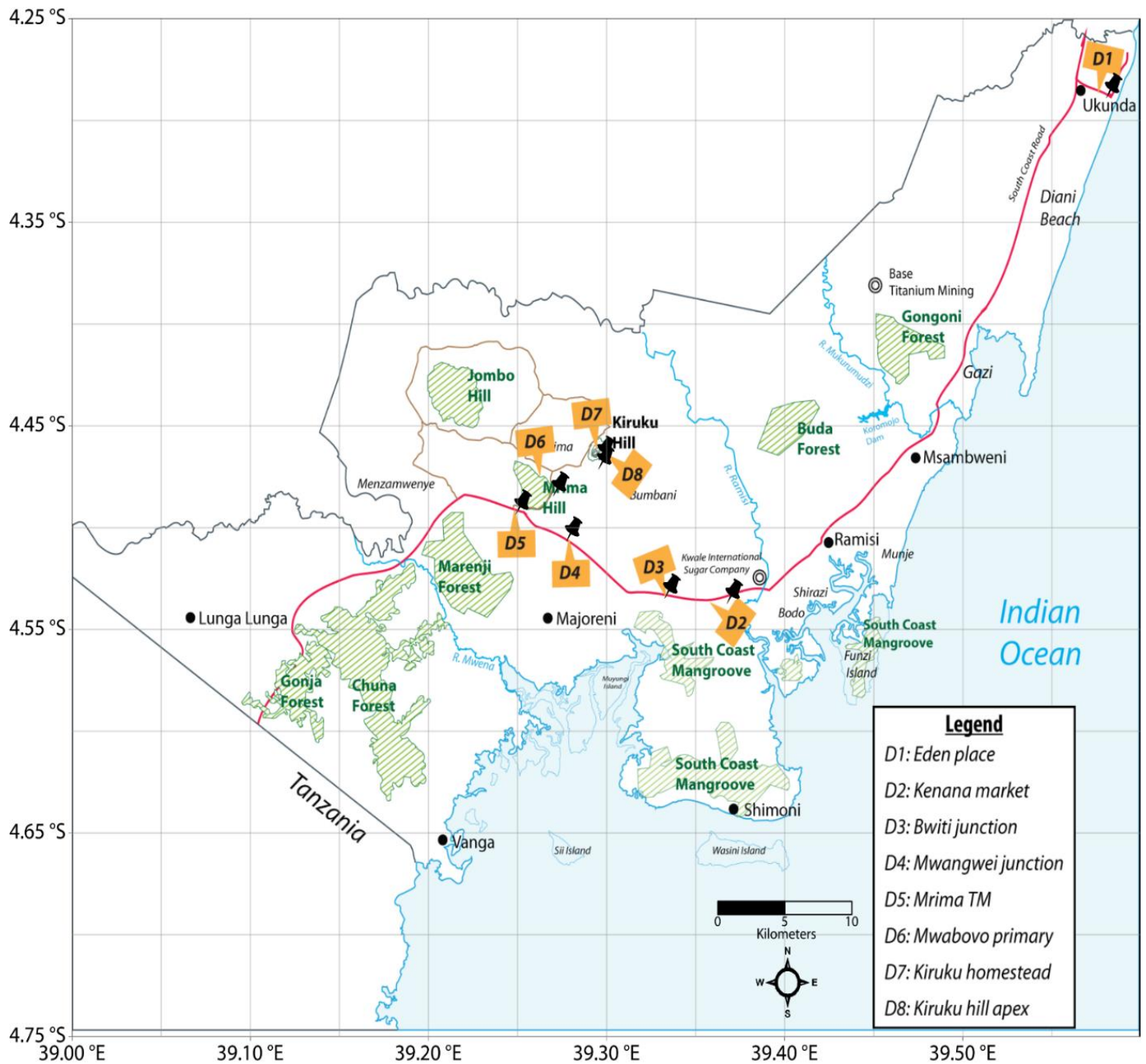
Figure 4.7: Sampling points from South Coast Kenya.

4.6.1 Low Volume Cascade Aerosol Sampler

The low volume sampler used in this work was a six stage cascade aerosol sampler (Model 135 mini MOUDI) with a flow rate of 2 L/min. The model was specifically designed with micro orifice nozzles in the lower stages to achieve nanometer size cut points with moderately low pressure drops. The stage configurations of the sampler could be used with a personal, battery operated sampling pump. Figure 4.8 shows the cascade sampler connected to the personal sampling pump.
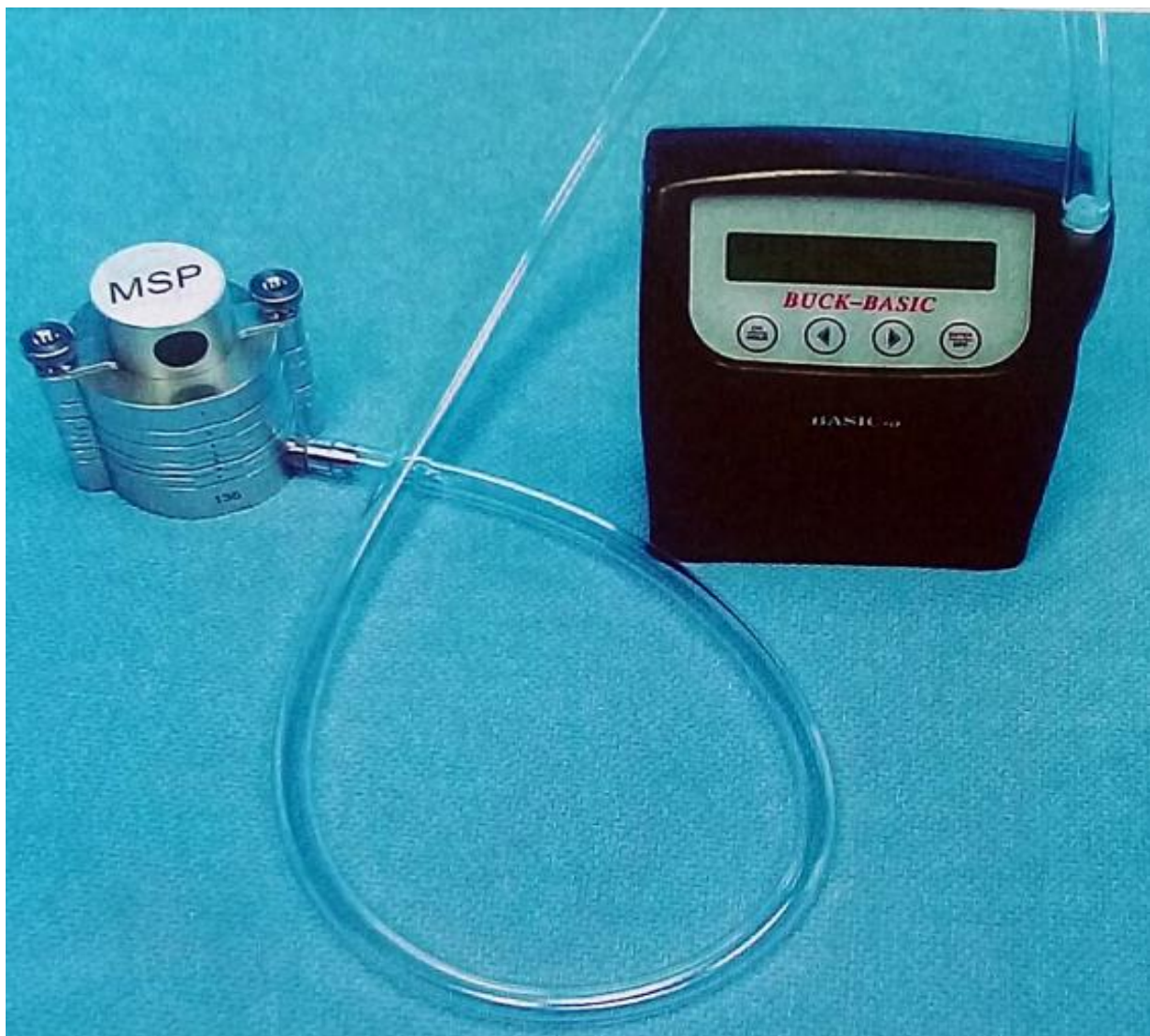
Figure 4.8: Cascade aerosol sampler connected to the battery operated sampling pump.

When mounting the aerosol sampler, the wind direction had to be considered. The nozzle of the sampler was aligned to face the direction in which the wind was blowing from in order to collect more particle loads. However, due to a constant flow rate, the wind direction had no influence on the volume of air sampled. The sampler used consists of six multiple – circular-nozzles in series. At each stage, jets of particle laden air impinge upon an aluminium substrate. Particles that are larger than the cut-size of that stage cross the streamlines and are collected on the impaction substrate below the nozzles while particles that are smaller than the cut size, flow and gets impacted to the next substrate that has smaller nozzles. This process continues on through the cascade impactor until the smallest possible particles unable to impact on the last impaction substrate are collected by a filter at the base.

 At every stage, the sampler was equipped with Al substrates (37 mm in diameter) that were manually unpacked after sampling for other substrates to be packed. To avoid contamination of the subsequent samples, after unpacking, the impactor parts were cleaned using acetone. After minutes of drying, the impactor was loaded with six new substrates ready for the next sampling.

Table 4.2 shows nominal cut sizes at 2 L/min inlet flow rate, the number of nozzles and the diameter of the nozzle for each impactor stage.

Table 4.2: Cut Sizes of the sampler nozzles.

Stage	Cut Size(μm)	Number of Nozzles	Nozzle diameter(cm)
1	10	2	0.381
2	5.6	2	0.260
3	**3.2**	2	**0.180**
4	**1.8**	2	**0.124**
5	1.0	3	0.0752
6	0.56	3	0.0447

Even though sampling was done for all the cut sizes, for purposes of this research, only stage 3 and 4 ($PM_{4.5}$ and $PM_{2.5}$ respectively) were used. In NF applications point of view, the two size particles are important since they can be sustained for very long in air and hence they are reliable when conducting source attribution. However, particle sizes less than $PM_{4.5}$ are important in health physics as the particle sizes are of the same dimension as the lung pore size and hence any particle less than $PM_{4.5}$ can be ingested.

4.7   Raman Analysis Procedure

High uranium concentration (1000-4000 ppm) simulates were first utilized so as to help identify the expected spectral response positions of uranium Raman scatter bands. For every simulate sample, five equidistant points on the Coffee Ring were used and for every point 10 spectra were obtained implying that 50 spectra were obtained for a single simulate sample. This was to compensate for any inhomogeneity that could be associated with the drop coating.

During acquisition of the Raman spectra, 10 seconds exposure time was used as per the optimized conditions. We also used x50 objective eye piece lens with a laser power of 5.6 mW for 532 nm

laser and 8.52 mW for the 785 nm laser as the best optimized combination for all my measurements. From the data acquired, Raman spectra were obtained and used to find limits of detection for uranium-specific bands using univariate methods.

4.8   Multivariate Chemometric Analysis of Raman Spectra

Raman spectra acquired from the simulate samples and field aerosol samples were subjected to multivariate chemometric analysis. For spectral data pre-processing purposes, we employed mean centering, smoothing and normalization of the data using Origin Pro (version 9.1) for simulate samples while for field samples all pre-processing was done using R. Multivariate data analysis was then performed using PCA, ANNs and MCR. MCR and the ANN algorithm were developed and implemented in MATLAB R2009a (Math works) while PCA was implemented in R. The MCR code implemented in Matlab was the one developed by Jaumot *et al.* (2015).

4.8.1 Multivariate Calibration Utilizing ANN

For ANN analysis, the calibration data was composed of 30 simulate samples. A network was designed for uranium utilizing its Raman scatter bands spectral region after feature selection. Using these regions, the data set was treated with two neural network architectures i.e. the cascade backpropagation algorithm and the backpropagation (BP-ANNs). The process of training consisted of assembling the data, creating the network object, training it and simulating the response to the new inputs. The two algorithms were compared based on how best they predict samples not exposed to the network and the most appropriate one adopted for use in the field samples.

The BP-ANNs was provided with three arguments that prompted the network to return the network object. A matrix of samples **S** was the first argument input vector while the second was the **T** target

vectors. The sample inputs and outputs were utilized in setting up the network input and output dimensions and parameters. The third argument consisted of a collection containing the sizes of each hidden layer. The output layer was derived from the targets.

The transfer function used for hidden layers which are non- linear was tansig while purelin was employed as transfer function for the output layer. The number of neurons in the hidden layer varied until the one that gave the least minimum square error (MSE) was adopted. For the newff training algorithm, we employed Levenberg – Marquardt where the training automatically stopped whenever validation error increased hence helping to avoid over fitting (Demuth and Beale, 2009). Since initial values of the input parameters were automatically generated randomly by the command, the predictions were always different whenever the algorithm was repeated. The training process was therefore repeated several times until the training network that provided the most reliable results was adopted. After adoption of the analytical model, results were first tested by simulating the output of the neural network with the input data measured. These results were compared with the measured outputs. Finally, the validation was carried out using an independent data set which was part of the simulate samples but not shown to the network. The schematic below shows a summary of all the chemometric techniques employed.
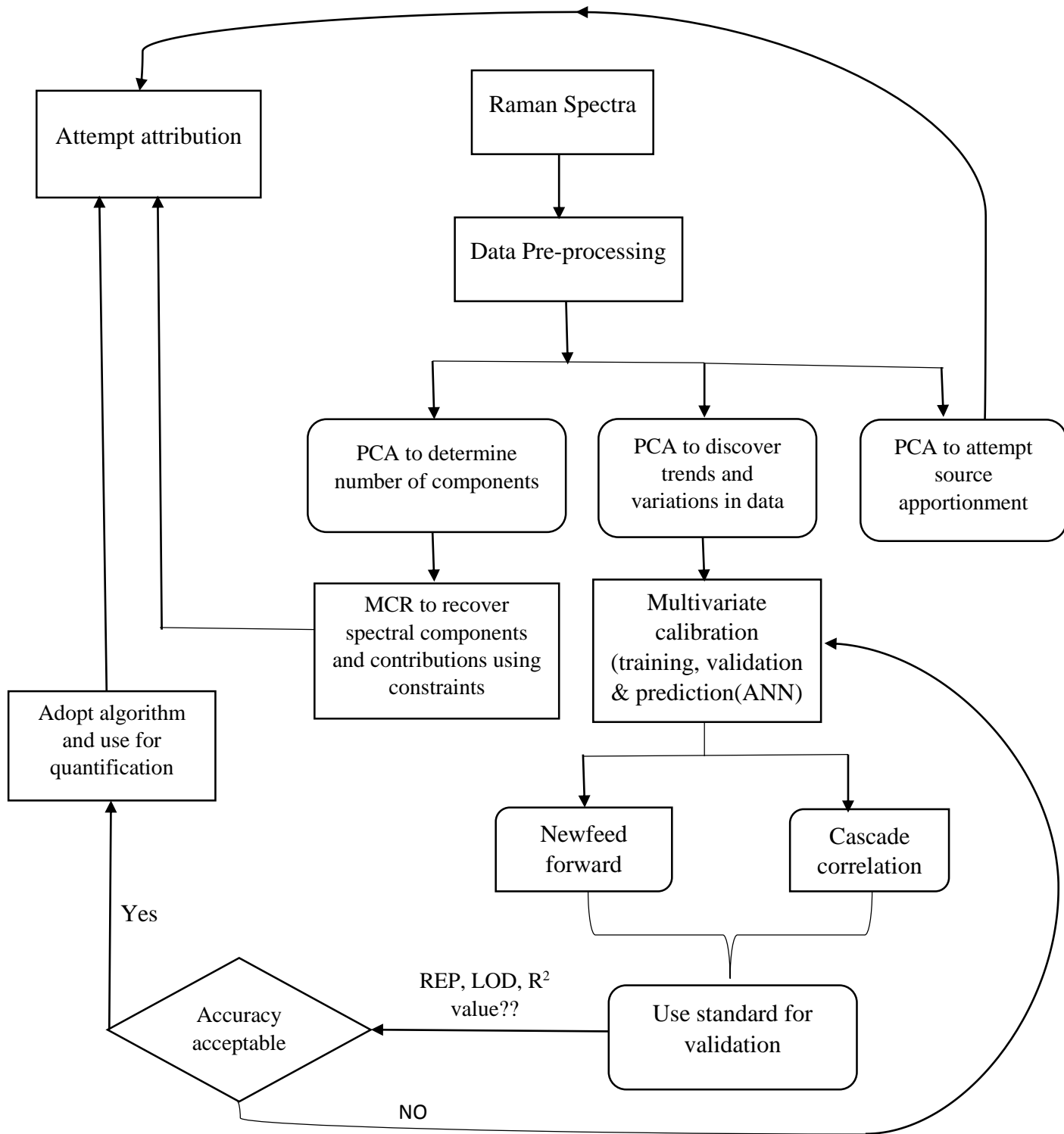
Figure 4.9: Schematic of chemometric methodologies employed towards calibration and attribution.

5 RESULTS AND DISCUSSION

5.1 Introduction

In this chapter, we present results of Raman microspectroscopy of simulates based on all uranium compounds and the spectra obtained from field aerosol samples. This is by utilizing concentration ranges from parts per billion to parts per million and exploratory analysis using multivariate chemometric techniques. Included are the results of Raman spectral data analyzed using PCA and ANN of simulate samples for method development.

5.2 The Coffee Ring Effect

The Coffee Ring as shown in Figure 5.1 depicts the distribution of the aliquot after the sample has dried on the substrate. It shows that the analyte distributes at the edges after drying forming a circular ring. The particles in the liquid suspension moves to the edges owing to time difference in drying. Hydrophilic surfaces such as those of perspex have a bigger retention ability and hence a smaller ring will be obtaned. The spectra therefore has to be taken from the edges as the central regions only gave the spectra similar to a blank substrate as shown in Figure 5.2.

Figure 5.1: Coffee Ring on an aluminium substrate for 100 ppm of uranium using 2 μl aliquot with the diameter of the ring≈430 μm while thickness ≈14 μm.

As shown in Figure 5.1, the drop coated spot is circular in shape, with a thicker outer region (composed of the analyte) and a thin center region (with no sample) as depicted by the spectra obtained in Figure 5.2. Both the spectra are characteristic of noise.
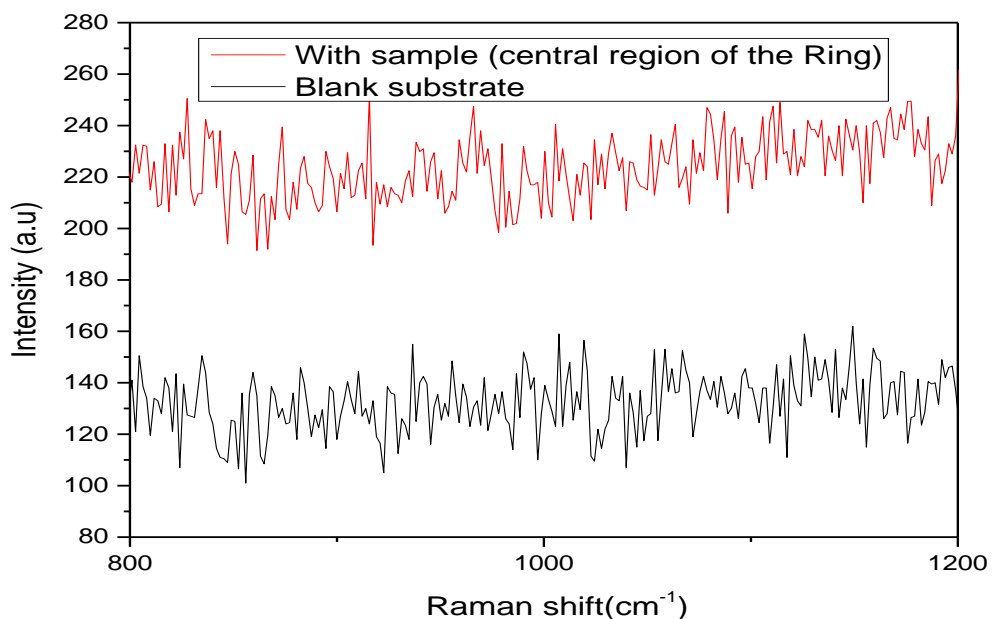
Figure 5.2: Spectra of a blank substrate compared to spectra from the central region of the Coffee Ring with sample.

5.3   Effect of Aliquot Size on Raman Intensity

The volume of aliquot micropippeted onto the substrate greatly influenced the intensity of the Raman signal. In this work, we investigated the response of the Raman active bands based on three different sample volumes (2 μl, 4 μl, 6 μl). A part from the Raman intensity, it was noted that the width of the ring increased as the volume of the sample increased as shown in Figure 5.3. A wider ring would probably mean that the analyte of interest has spread more to the edges.

	Scale Indicator		
	Aliquot Volume (μl)	Diameter of the Ring (μm)	Maximum thickness (μm)
	2	160	6
	4	430	14
	6	580	20
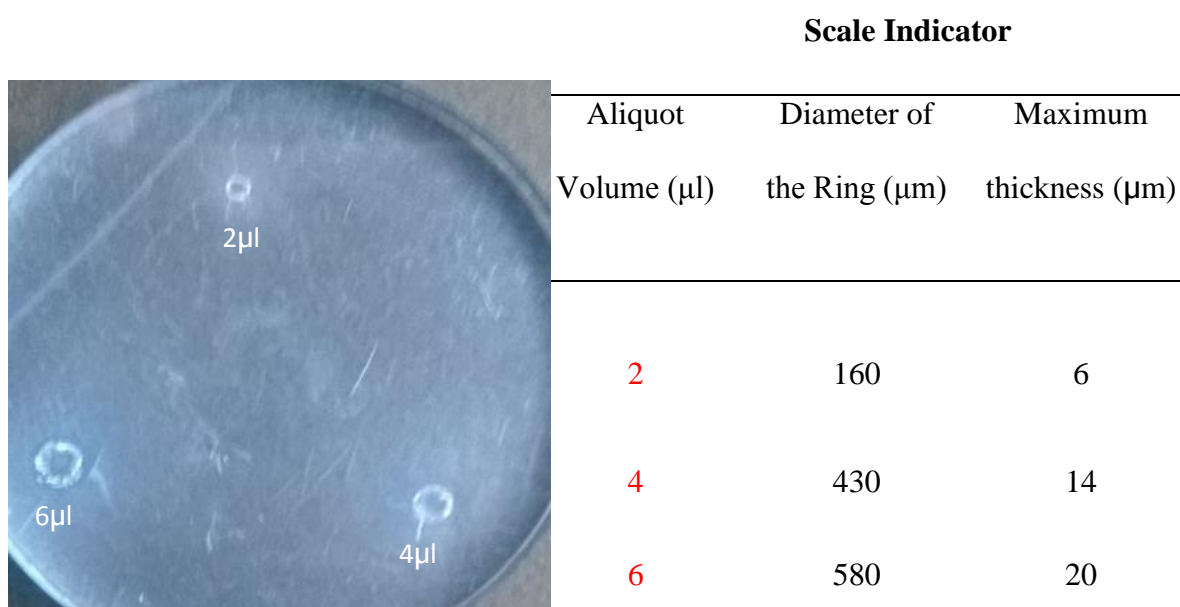
Figure 5.3: Coffee Rings of three different aliquot volumes having 100 ppm of uranium with their ring diameters and thickness measured using Raman spectroscopy.

The width of the ring generally increases as higher aliquot volumes are used so that most of the particles are pushed away from the center to the margin. This is the same reason the spectra taken at the center of the ring depicted no signal corresponding to the analyte. Instead it showed the signal that belonged to the substrate. The coffee ring occurs due to the difference on the rate of evaporation where the liquid evaporating from the edges is replaced by the one coming from the interior surface hence more particles get laddened on the edges.

As shown in Figure 5.4 however, the intensity of the Raman signal reduces with an increase in sample volume. We can attribute this observation to the fact that for small volumes, the Coffee Ring created is small and hence the analytes concentrates in a small area which increases the surface density. Consequently, after drying on the substrate, almost all the particles absorb the radiation (due to good laser and analyte interaction) and hence the resulting spectra becomes amplified. Moreover, since the focal volume of the focused laser beam is very low, the laser can interact with a bigger portion of the analyte hence generating an amplified signal. The ring diameter and maximum thickness were obtained using the size measuring component of the Raman vedio monitor.
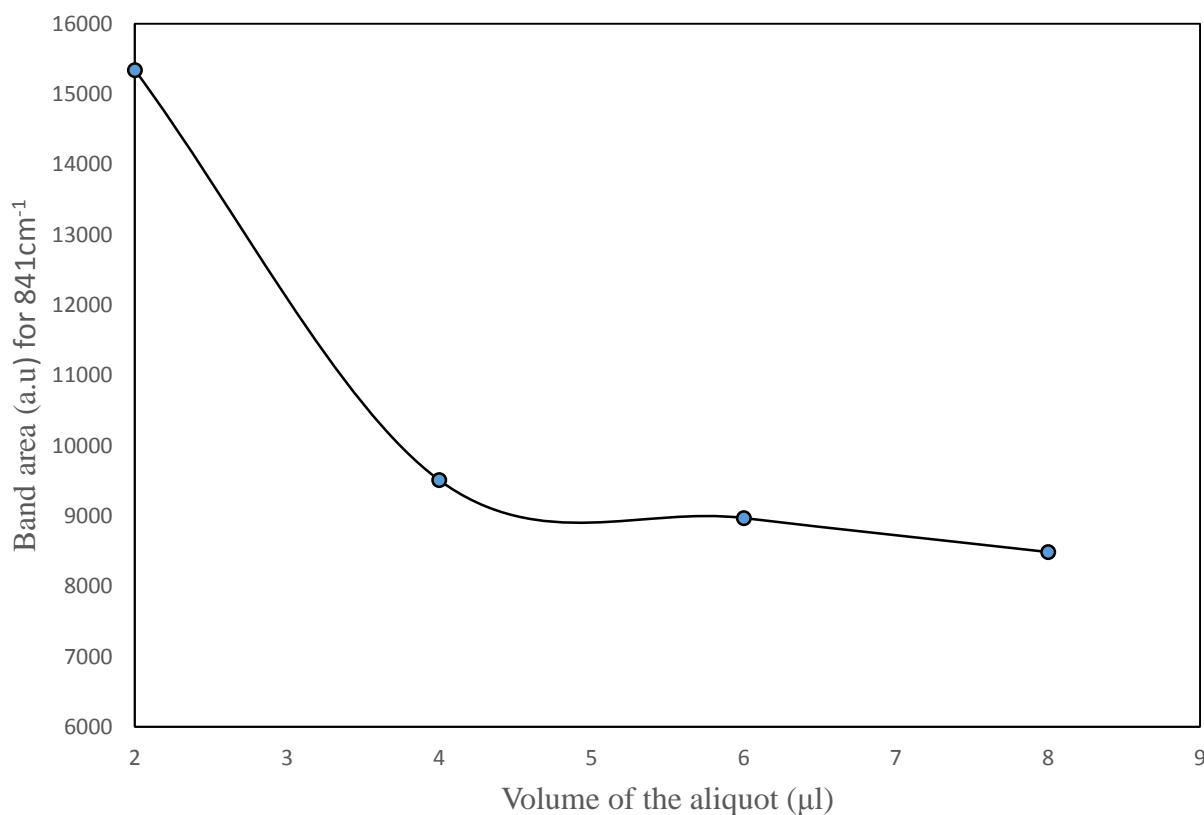
Figure 5.4 Effect of aliquot volume on intensity of the U-O band at 841cm^{-1}.

Following the above observations, 2 µl sample volume was used as an optimized parameter for all the prepared simulates.

5.4 Effects of Substrate on the Uranium Signal Intensity

The efficacy of the application of drop coating deposition Raman technique relies significantly on the choice of the substrate used. Some substrates are known to enhance signals of bonds of molecules that are Raman active yet inhibit signals of other compounds. Other substrates like glass suffer from a lot of fluorescence irrespective of the excitation laser employed (Ru and Etchegoin, 2009). Figure 5.5 shows the comparison of the uranium specific Raman scatter bands when different substrates are used. The uranium concentration is 10 ppm. In Figure 5.5 (b) the spectra for the aluminium foil has been offset to show the broadening of the spectral band.
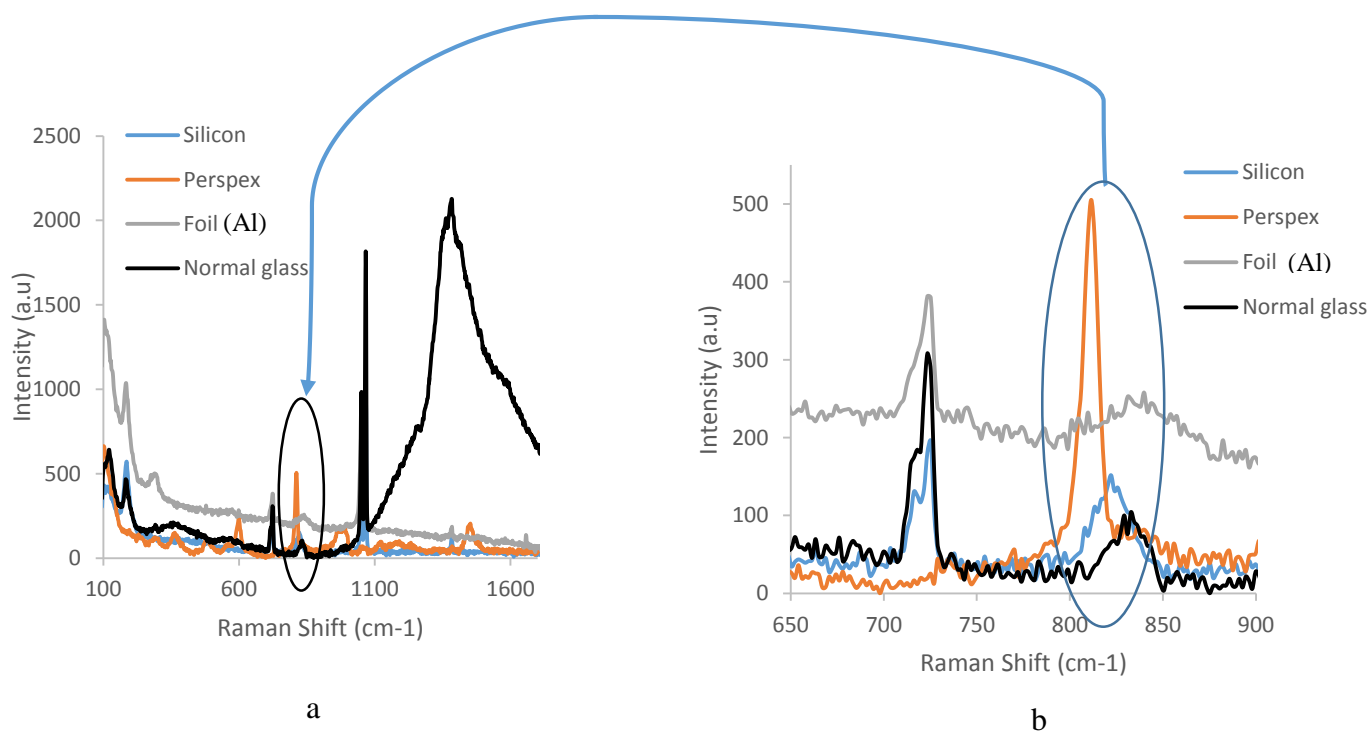
Figure 5.5: Substrate effects on Raman signal for 10 ppm uranium using 785nm laser.

It can be observed that perspex was the best in enhancing the signal as compared to the other three substrates. Firstly, perspex is quite hydrophobic, therefore a deposited drop of aqueous solution won't spread like in the case of glass slides. Besides its hydrophobic nature, we can deduce that perspex has a high optical reflectance such that each photon has a chance of interacting with the sample twice (incident and reflected). By that, the signal is enhanced (Zhang *et al.*, 2003). In drop coating deposition Raman, a good substrate should have a low solvent ability such that there is a no wetting interaction with the analyte solution. For perspex, the deposited solution did not spread so much as compared to other substrates. This ensured that the deposited analyte concentrates in a small area significantly increasing the surface density consequently improving the detection limit. The improved uranium band signal using perspex also suggests that it had little/ no background signal interferences. The intensity of Raman signal also depends on the square of the electric field intensity (i.e. I= $[E]^2$). The difference in signal intensities from the four substrates could also be as a result of differences in the spatial distribution of the electric field at the substrate-sample surface. The substrate alters the spatial location of maximum field enhancement around the sample molecules (Mikoliunaite *et al.*, 2015). Perspex materials can therefore be used in making good substrates not only for laboratory use but also for future aerosol sampling. Generally, the Raman scatter band positions shifted a bit for the different substrates owing to the fact that substrates change the spatial distribution of the electric field at the substrate/analyte interface hence a shift in position and a difference in intensity.

5.5 Raman Spectra of Simulate Samples

Figure 5.6 shows a Raman spectrum of a simulate sample (having uranium in the presence of the mixture of anions (NO_3^{2-}, SO_4^{2-}, Cl^-). The observed uranium-specific spectral bands were quite informative in developing the calibration strategies for quantification purposes. Since samples

from the field are expected to have very low uranium concentrations (in the ppb range as explained in literature), the developed model first had to utilize elevated concentrations (1000 - 3000ppm) so as to identify the regions of expected spectral responses from uranium. For the simulate samples, uranium existed in the form of uranyl nitrate. Aluminium substrate was used for all the simulate samples as it will still be useful in field sampling.
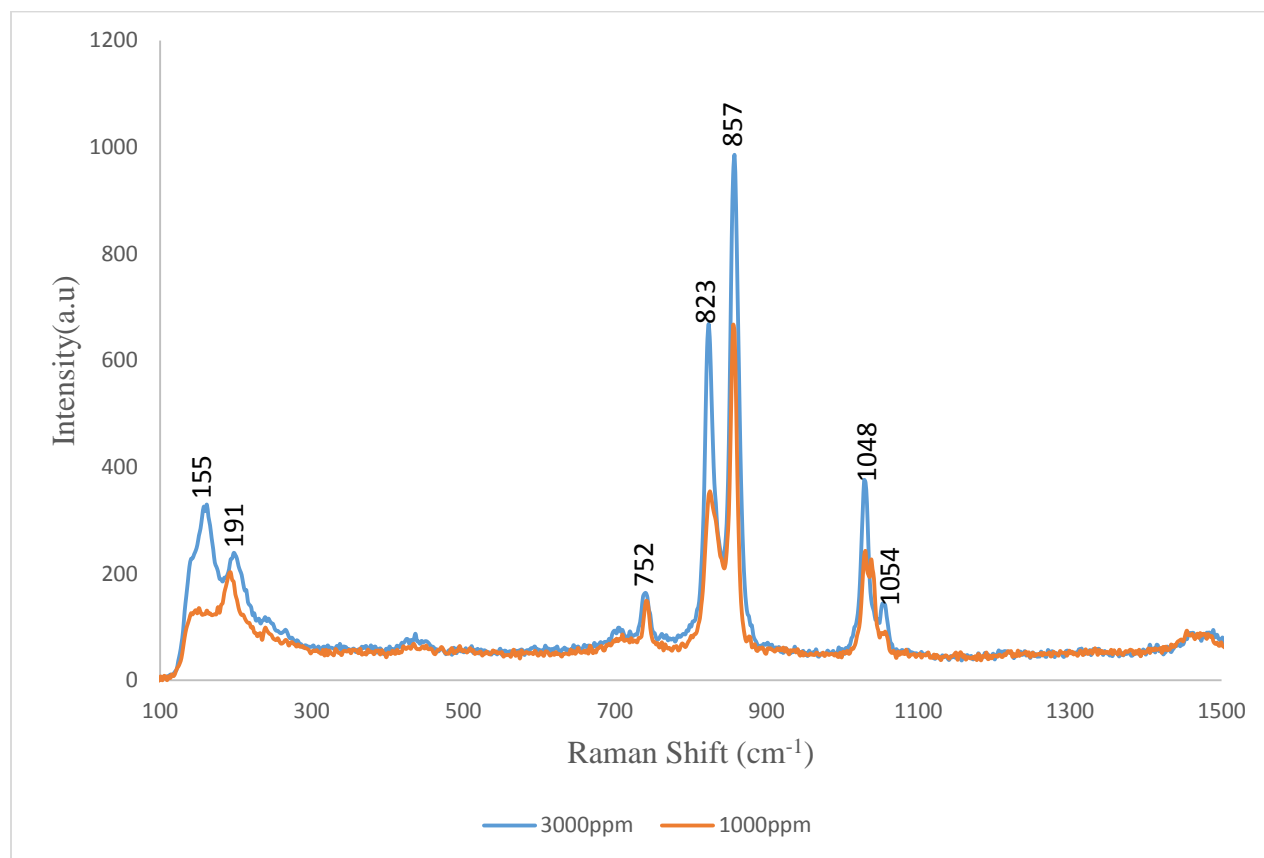
Figure 5.6: Typical Raman spectrum of a simulate sample for 1000 ppm and 3000 ppm uranium on an aluminium substrate using 785 nm laser.

From the spectrum, we can assign 823 cm^{-1} to uranium trioxide (U-O stretching vibration) (Palacios and Taylor, 2000), while 857 cm^{-1} can be assigned to uranyl (UO$_2^{2+}$ symmetric stretch, NO3^{2-}bound) (Bullock and Parrett, 1970; Nguyen Trung *et al.*, 1992) while 191 cm^{-1}, 752cm^{-1},

and 1048 cm^{-1} can be assigned to Cl^{-1}, NO$_3^{2-}$ and SO$_4^{2-}$ ions respectively as background anions within which uranium is embedded (Lu *et al.*, 2016; Stefaniak *et al.*, 2009; Aksenenko *et al.*, 1986).

5.6   Qualitative Laser Raman Analysis of Different Uranium Compounds

Raman spectra for four uranium compounds (uranyl nitrate, uranium trioxide, uranyl sulpahte and uranium trioxide) were acquired using both 532 nm and 785 nm excitation lasers and analyzed to study the Raman band associated with each of the uranium compound bonds. These scatter bands associated with each of the uranium compounds and their assignments are summarized in Table 5.1 and 5.2. All uranium compounds were prepared as suspensions by diluting 0.1g of each uranium compound in 10 ml of distilled water and dried on Al substrate. All the uranium compounds were of analytical grade from British Drug House.

5.6.1 Uranium Trioxide

The Raman spectrum of uranium trioxide shows the U-O stretching band at 839 cm^{-1} for 532 nm laser and 841cm^{-1} for 785 nm laser. The intensity of the Raman scatter band is however more intense for 532 nm laser as compared to 785 nm laser because a small laser wavelength is expected to give a higher intensity since intensity is expressed as the invest. However, as shown in Figure 5.7, 532 nm laser has spectral interference from fluorescence. This shows that the two lasers provide the same Raman scatter band but with slight shift in band position.
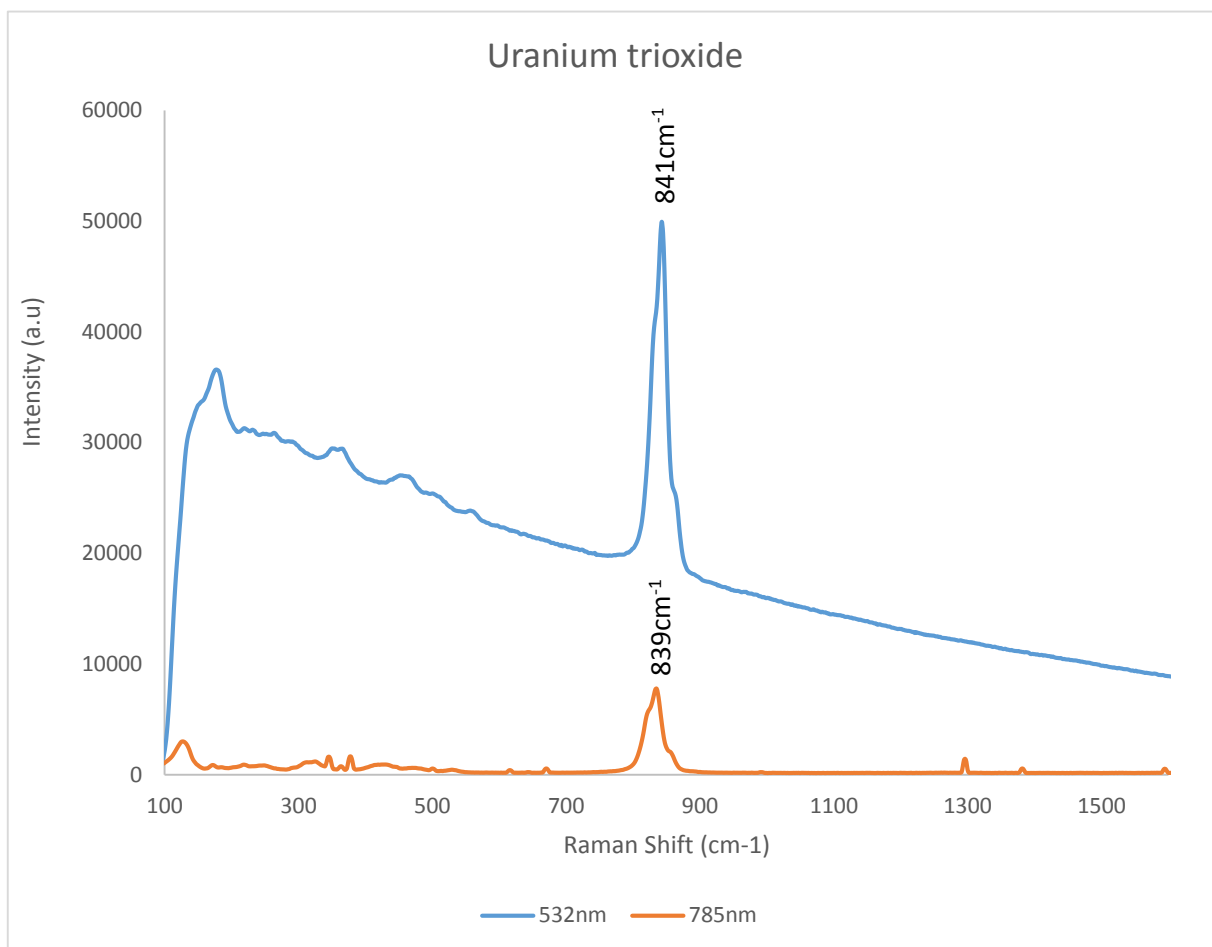
Figure 5.7: Raman spectra of uranium trioxide using 532 nm and 785 nm Laser.

5.6.2 Uranyl Nitrate

The Raman scatter band associated with uranyl nitrate as shown in Figure 5.8 was observed at 865 cm^{-1} and 860 cm^{-1} for 532 nm and 785 nm laser respectively while the band associated with the nitrate anion was observed at 1048 and 1054 cm^{-1} for 785 nm laser and 1028 and 1038 cm^{-1} for the 532 nm laser. Other than these bands, another band could be observed at 752 cm^{-1} which was assigned to the nitrate ion.
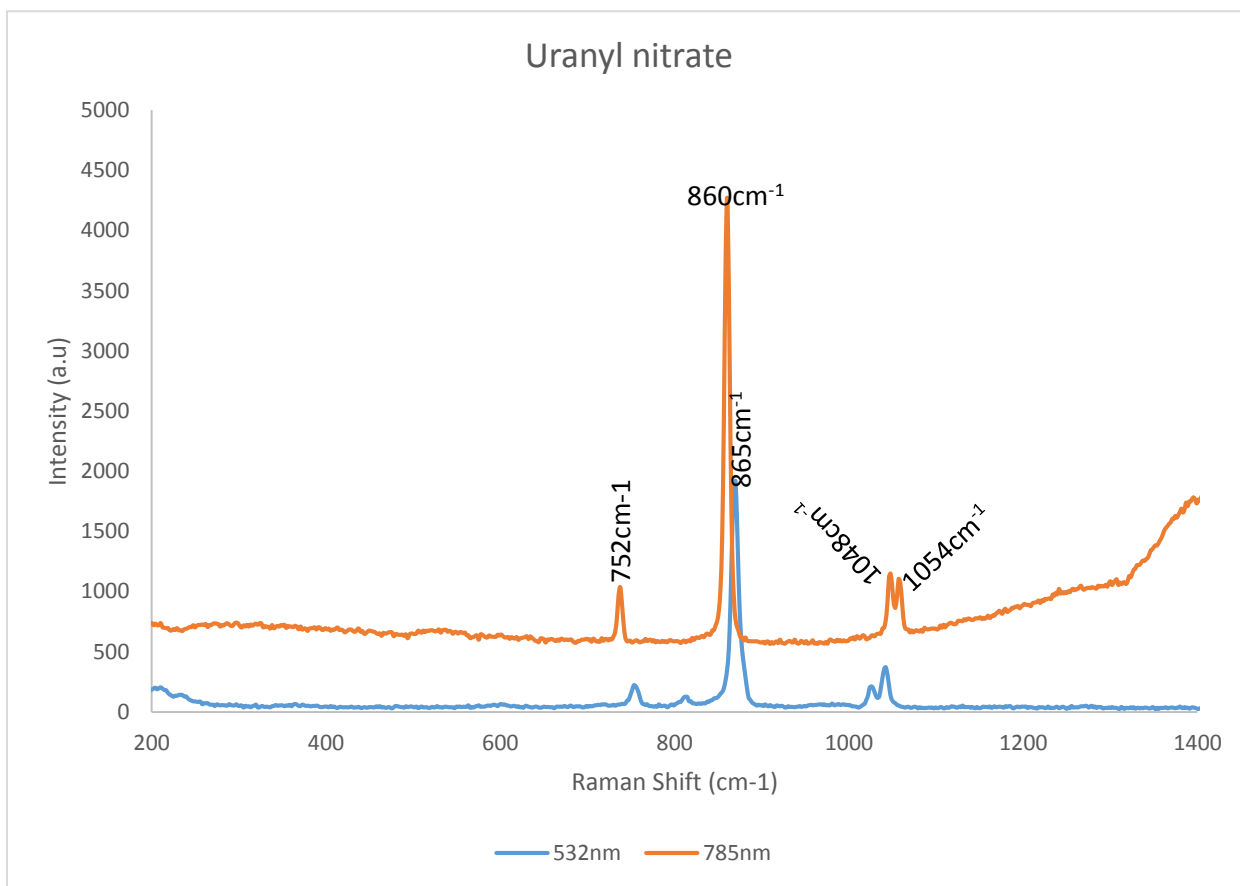
Figure 5.8: Raman spectra of uranyl nitrate using 532 nm and 785 nm laser.

5.6.3   Uranyl Chloride

The Raman spectra from uranium chloride shows a uranium band at 814 cm^{-1} when using the 532 nm laser though this band could not be detected by 785 nm laser where it instead appeared as a small band at 822 cm^{-1}. Of particular interest is the peak at 604 cm^{-1} for 532 nm and 659 cm^{-1} for 785 nm which has previously been reported to be assigned to uranitite and also associated with oxidation of uranium chloride to uranium dioxide (Stefaniak *et al.*, 2008) which explains the existence of U-O bond from uranyl chloride. The peak at 1154 cm^{-1} has previously been reported in the literature as 1150 cm^{-1} and associated with uranium dioxide and assigned to U-O bond

(Pointurier and Marie, 2010b). The peak at 998 cm^{-1} on the other hand is specific to vibrational mode of chloride ion.
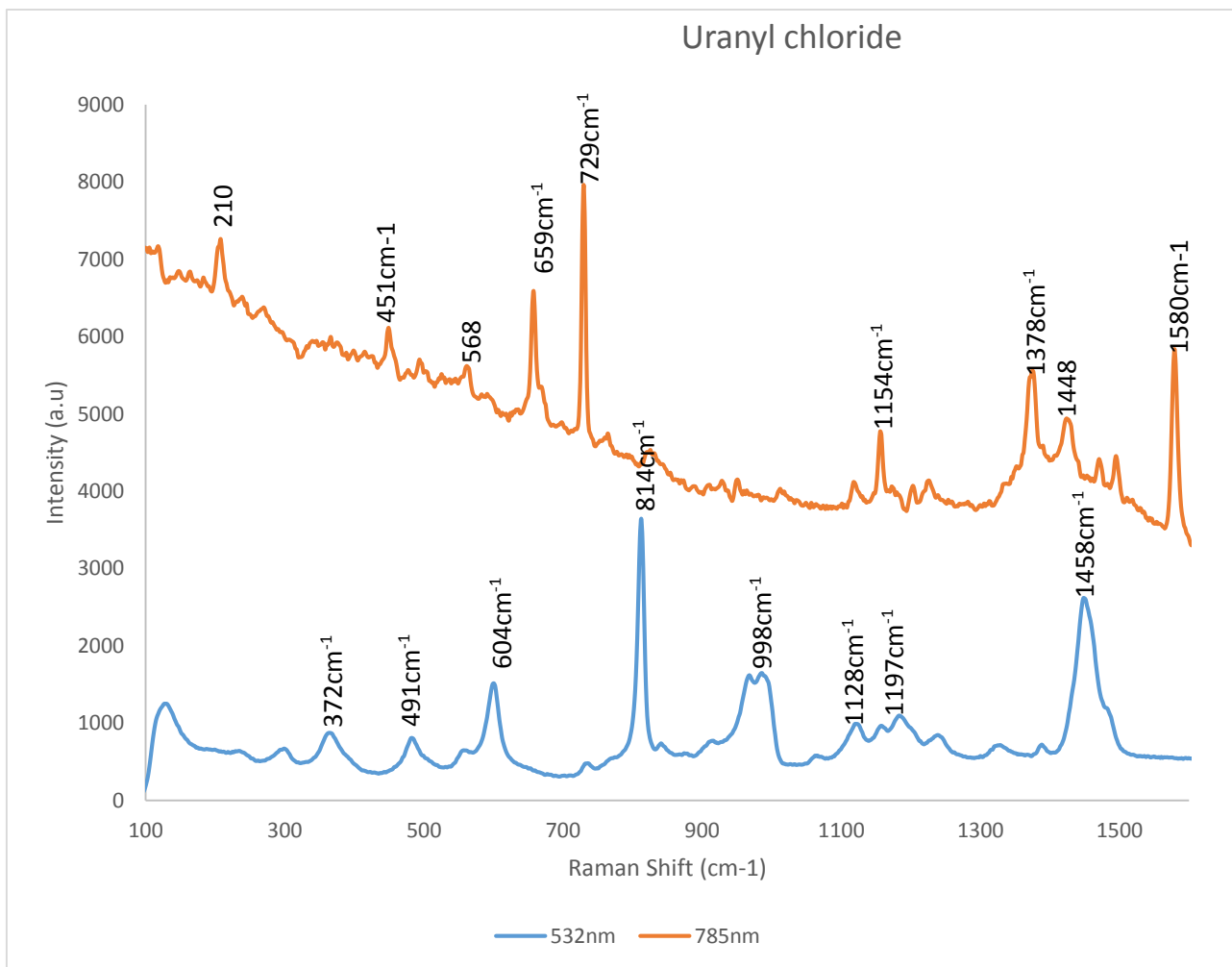
Figure 5.9: Raman spectra of uranyl chloride using 532 nm and 785 nm laser.

5.6.4 Uranyl Sulphate

The Raman scatter bands associated with $UO_2\,(SO_4)$ could be noted at 814 cm^{-1} and 868 cm^{-1} when using 532 nm laser. These bands however could not be detected using the 785 nm laser. The bands assigned to uranitite could be detected at 610 cm^{-1} for 532 nm laser and 659 cm^{-1} with 785 nm laser though shifted by +15 cm^{-1} while the band associated with the sulphate anion was 998/1004 cm^{-1} and 1458 cm^{-1}.
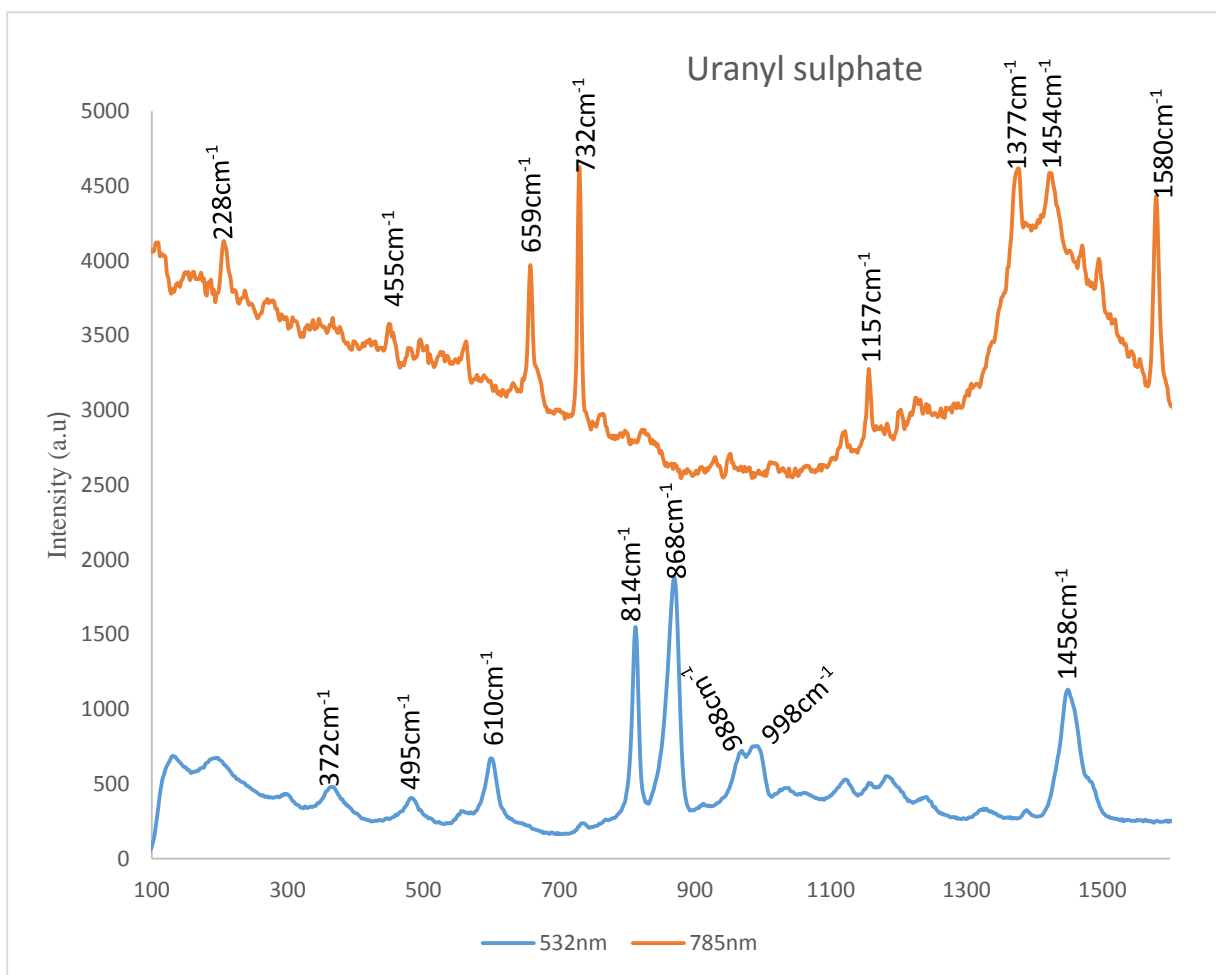
Figure 5.10: Raman spectra of uranyl sulphate using 532 nm and 785 nm laser.

5.6.5 Interpretation of Results

The main objective of undertaking qualitative analysis of all the uranium compounds was to identify uranium scatter bands that uniquely belong to uranium as will be expected in typical uranium bearing aerosols. The identified uranium bands were used as the nuclear forensic signatures from Raman scatter. The Raman scatter bands associated with the shifting of the very bands as a result of various anions helped in attempting attribution in the context of in-field nuclear forensics. Spectra from all the uranium compounds reveal characteristic Raman features that can uniquely be identified with uranyl species having vibrational frequencies ranging from 750 to 870 cm^{-1}. As shown from the spectra in uranium trioxide and uranyl nitrate, the vibrational frequencies are independent of the laser excitation wavelength. This may be attributed to the two uranium compounds having similar bond strengths as well as the polarizability. However, the intensity of uranium scatter band is larger for the 532 nm laser as compared to the 785 nm laser. This is for the fact that Raman scattering intensity is inversely proportional to the fourth power of the excitation wavelength.

Table 5.1: Raman scatter bands for different uranium compounds using 532 nm laser

Speciation	Vibrational mode	Wavenumber		Reference
		This work	Literature	
$UO_2(NO_3)_2.6H_2O$	Bound NO_3^{2-}	206	209	(Bullock and Parrett,
		756	751	1970)
	UO_2^{2+} symmetric	1048	1048	
	stretch	1054	1052	
				(Nguyen Trung *et al.*,
		865	868	1992)
	U-O symmetric	372	unavailable	
UCl_3	stretching	491	494	(Driscoll *et al.*, 2014)
	vibration	604	636	
		814	808	(Lu *et al.*, 2016)
		1154	1154	
		1458	1454	
Cl^-	Free Cl^-			
		604	unavailable	
		729	732	(Lu *et al.*, 2016)
		998	998	
UO_3	U-O stretching	841	841	(Palacios and Taylor,
	vibration			2000)
		372	372	
		495	494	
$UO_2(SO_4)_2.3H_2O$		659	656	
		814	808	(Lu *et al*., 2016)
		868	863	(Maxime and Laurent,
				2013)
		1458	1458	
NO_3^{2-}	Free NO_3^{2-} (υ_1)	1048	1048	(Aksenenko *et al.*, 1986)
		1051	1054	
SO_4^{2-}	Free SO_4^{2-}	746	752	
		951	982	(Stefaniak *et al.*, 2009)

Table 5.2: Raman scatter bands for different uranium compounds using 785 nm laser

Speciation	Vibrational mode	Wavenumber		Reference
		This work	**Literature**	
$UO_2(NO_3)_2.6H_2O$	Bound NO_3^{2-}	206	209	(Bullock and Parrett,
		753	751	1970)
		1054	1054	
	UO_2^{2+} symmetric stretching	860	868	(Bhatt *et al.*, 2017; Nguyen Trung *et al.*, 1992)
UCl$_3$	U-O symmetric stretching vibration	451	450	(Palacios and Taylor, 2000)
		659	658	
		1154	1154	
		1454	1454	(Stefaniak *et al.*, 2013)
Cl$^-$	Free Cl$^-$	604	604	
		729	732	
UO$_3$	U-O stretching vibration	839	841	(Palacios and Taylor, 2000)
$UO_2(SO_4)_2.3H_2O$		659	658	
		1454	1458	(Stefaniak *et al.*, 2013)
NO_3^{2-}	Free NO_3^{2-} (υ_1)	1041	1047	(Aksenenko *et al.*, 1986)
		1051	1053	(Bhatt *et al.*, 2017)
SO_4^{2-}	Free SO_4^{2-}	732	729	
		988	982	(Stefaniak *et al.*, 2009)

5.7   Quantitative Analysis of Uranium in Simulate Samples

In order to determine the detection limit of uranium in the simulate samples, a calibration curve was plotted. Since the detector experienced saturation effects, a small concentration range was chosen based on a single uranium band (at 841cm^{-1}). I settled on this band owing since it was conspicuous and formed the most important forensic biomarker for all the uranium molecules. Figure 5.11 shows the linear fit calibration curve (R^2=0.982) with error bars indicated. The error bars were obtained as standard deviations associated with five different spots on the same substrate. The limit of detection of uranium was obtained based on the equation 5.1.
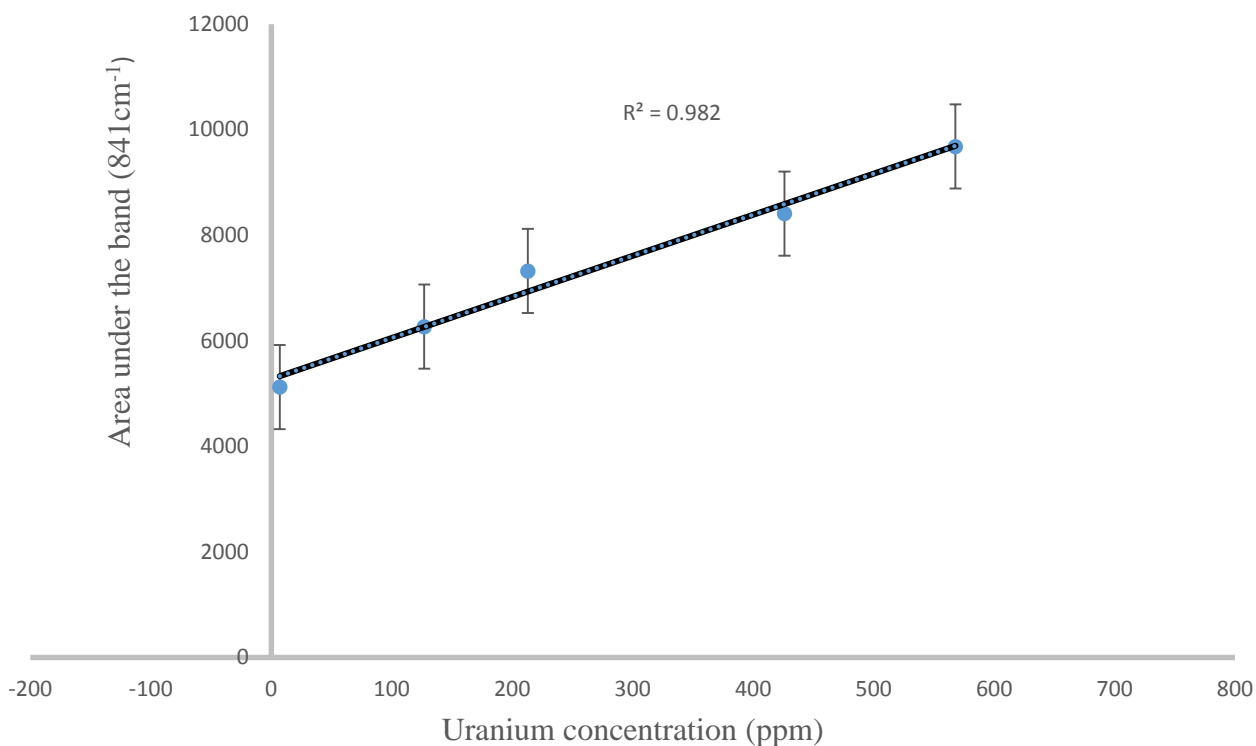
Figure 5.11:   Signal intensity vs uranium concentration in uranium simulates using uranyl nitrate.

$$LOD = \frac{3\sigma}{S}$$ 5.1

Where σ is the average standard deviation of six blanks and S is the sensitivity. In utilizing the equation, limit of detection for uranium in simulates based on the Raman scatter peak was obtained to be 1.43 ppm. At this LoD, it becomes a great challenge to use Raman microspectroscopy for direct quantification of the ultra-trace uranium levels in aerosol particles.

5.8 Artificial Neural Network on Aerosol Simulates Samples

ANN based on two algorithms (new feed forward and cascade correlation) was utilized in developing calibration models. The algorithm that gave the most reliable predictive ability was adopted. The models were based on building a relationship between the desired concentrations of the uranium molecule in a sample and its corresponding spectral data. This was aimed at enabling prediction of trace levels of uranium in the aerosol field samples based on the observed characteristics in the simulate samples.

The R^2 value which is a measure of how well the disparity in the output is explained by the targets helped in determining the efficiency of the model in predicting new samples. If the numerical R^2 value is close to 1, then the conclusion is that the targets and the outputs correlate well. The best model was characterized by low mean squared error by utilizing few neurons in the hidden layer. The bands utilized for this work were based on the bands that uniquely belong to aerosol particles. The spectral window chosen were specific for uranium scatter bands centered around 808/814, 838/846, 865/868 and 1154 cm^{-1}.

5.8.1 Spectral Pre-processing Before Model Development

Since multivariate chemometric methods rely on the shape of the peak/ Raman band to a very small extend, band overlaps and other spectral matrix effects are resolved through spectral pre-processing to remove spectral noise. The first step was to do spectral data compression by only selecting appropriate spectral regions of interest. Since there were no shifts in band positions during measurements owing to the stable spectrometer, the feature selected regions were consistent for all sets of data. Non –linearity of data was not a big issue as unlike partial least squares, ANN is rarely affected by non-linear data (in terms of how the signal intensity responds with analyte concentration). Outlier detection was an important aspect before a calibration strategy was employed. Smoothing of data was then employed in Origin pro using Savitzky and Golay so as to reduce the random noise from the instrumental signal. During smoothing, a polynomial of order 2 was employed. Other signal processing techniques such as mean centering were not employed as they were found to negatively influence the prediction ability of the calibration model.

5.8.2 ANN Based on New Feedforward Algorithm

The BP-ANN was developed on two sets of simulates; one in the ppm range while another set of samples were developed in the ppb range. The former model was adopted and used to predict uranium concentration in the IAEA RGU-1 standard as the uranium concentration in the standard was within the range of the model while the latter model was developed and adopted hence utilized for predicting uranium in aerosol field samples. The accuracy of the second model was based on its ability to predict uranium concentrations of simulate samples whose concentration values (still in ppb range) were not shown to the network.

The BP-ANN algorithm was based on 4 neurons in the hidden layer after optimization. By varying the number of neurons by increasing by one, several trials were made by training, testing and validating to achieve the smallest error in training as a function of the addition of neurons to the intermediate layer. Figure 5.12 shows how the mean square error decreased to lower values until the network converged.
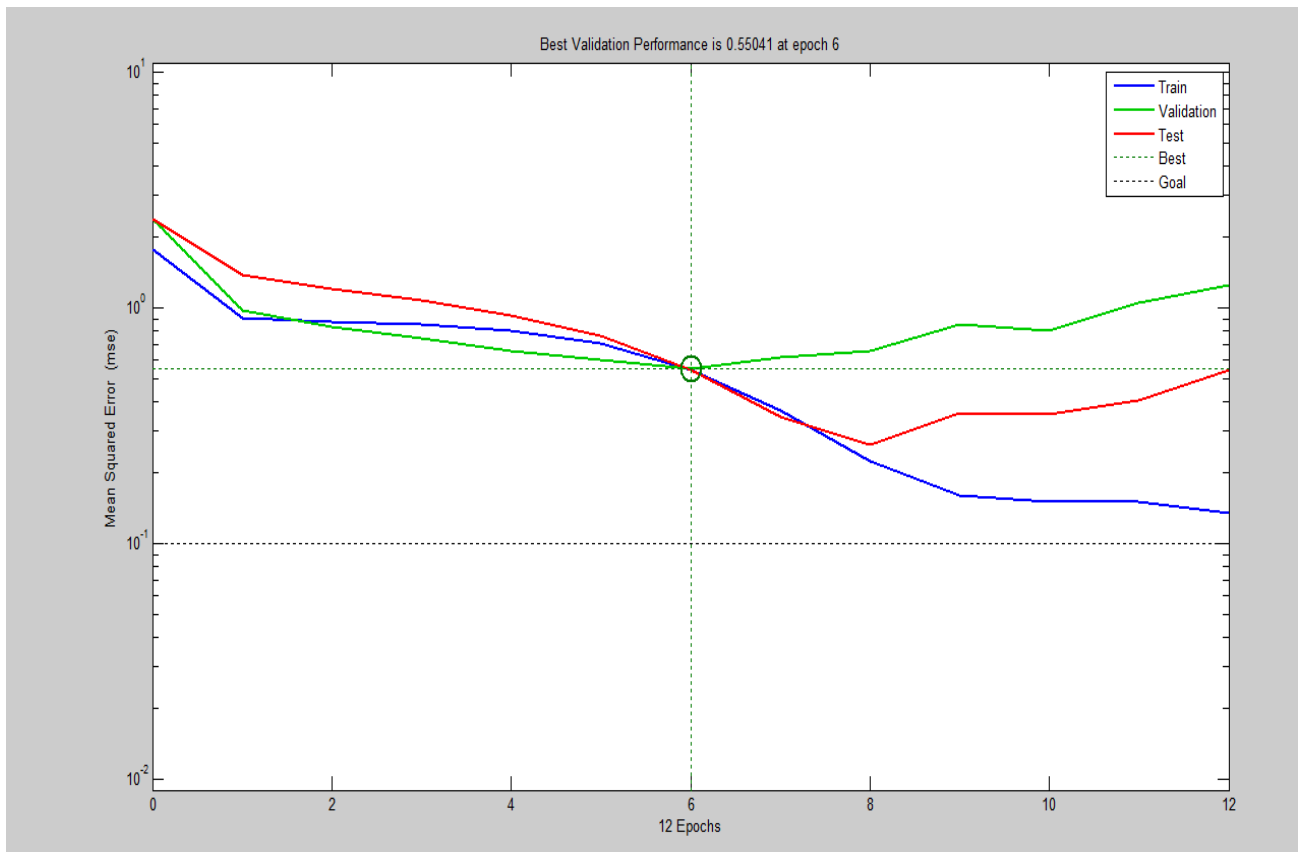
Figure 5.12: Performance plots for ANNs training errors for 4 neurons using newfeed forward.

The blue line is linked to the training, the green linked to the validation while the red was linked to the testing analysis of the model and as a result of the input data fed into the network bring divided into three sets; 60% of the data for training the network, 20% for validating the network performance on the input data while 20% of the data was to test the performance of the algorithm

on the data. Table 5.3 shows how various neurons in the hidden layer influenced the performance of the network with efficiency focused on the R^2 value as it shows the correlation between targets and outputs. A very high number of neurons in the hidden layer would result into over-fitting while very few would not classify correctly. For this algorithm, 4 neurons were selected since they gave low MSE and a consistently R^2 value close to 1.

Table 5.3: Analytical performance indices for different ANN models based on BP-ANN

Model	Number of neurons in hidden layer	MSE for best validation performance	Number of epoch	Correlation coefficients			
				Training R^2 value	Validation R^2 value	Test R^2 value	Overall R^2 value
J	1	115.32	2	0.941	0.901	0.940	0.920
K	2	95.08	3	0.981	0.886	0.817	0.912
L	3	71.64	2	0.945	0.951	0.894	0.943
M	**4**	**55.04**	**6**	**0.993**	**0.968**	**0.982**	**0.985**
N	5	17.97	4	0.918	0.931	0.922	0.961

By the 6th epoch, there was no extensive over-fitting as both the test and validation sets were similar. The response of the network and its corresponding targets were investigated and the results are shown in the regression analysis in

Figure 5.13. The parameters indicated as red were the optimized parameters for the model.
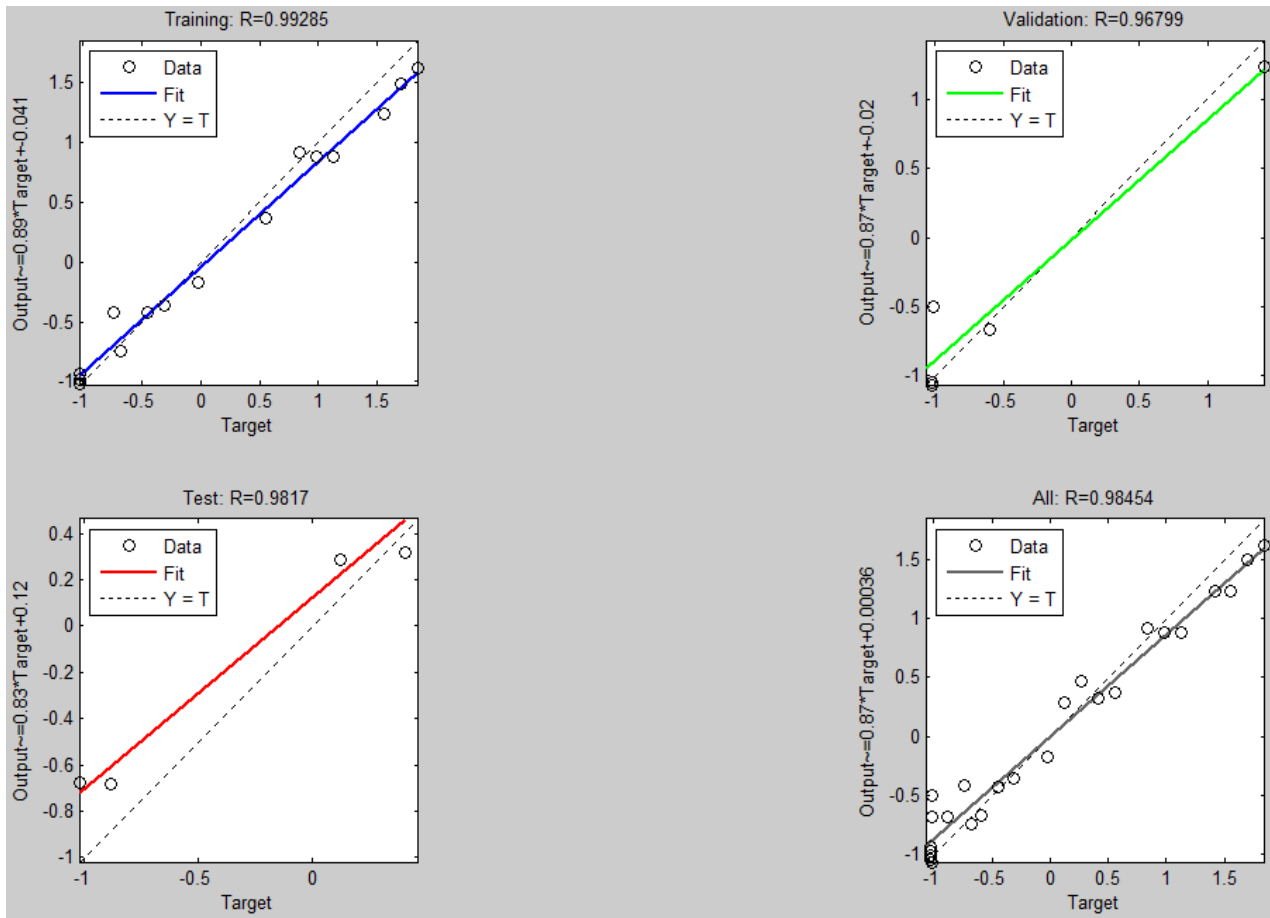
Figure 5.13: Linear regression of ANN and the corresponding targets based on uranium bands using new feedforward.

As shown Figure 5.13, the feedforward architecture enabled the network to simultaneously train the model for the element of interest with an R^2 value of 0.993 which is very close to 1. This was successively followed by good validation and prediction R^2 value of 0.968 and 0.982 respectively. This resulted to an overall R^2 value of 0.985. Figure 5.14 shows the performance of the model based on simulates with uranium in the ppm range. The ANN prediction results were closer to the true values of the spiked uranium concentrations.
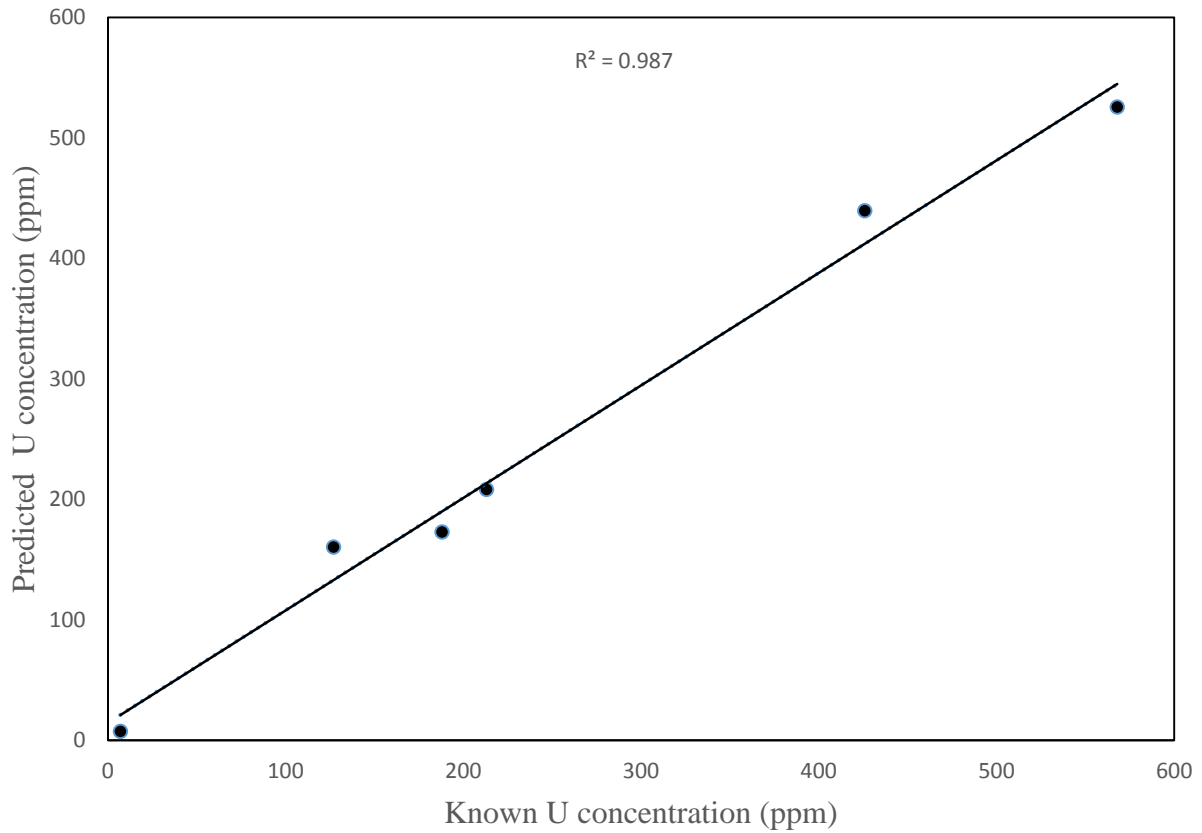
Figure 5.14: ANN regression plot for predicted verses known utilizing uranium scatter bands.

The predicted verses known regression plot in Figure 5.14 show the BP-ANN model predicted the

uranium in simulate samples and the likelihood of how it will predict for the uranium in aerosol

particles having a similar matrix.

5.8.3   Cascade Correlation for Quantitative Analysis of Uranium in Simulates

Based on the optimization of the network architecture, for cascade correlation, the predictive ability of the model was based on 3 neurons in the hidden layer. The optimization was achieved at epoch 2 as shown in Figure 5.15.
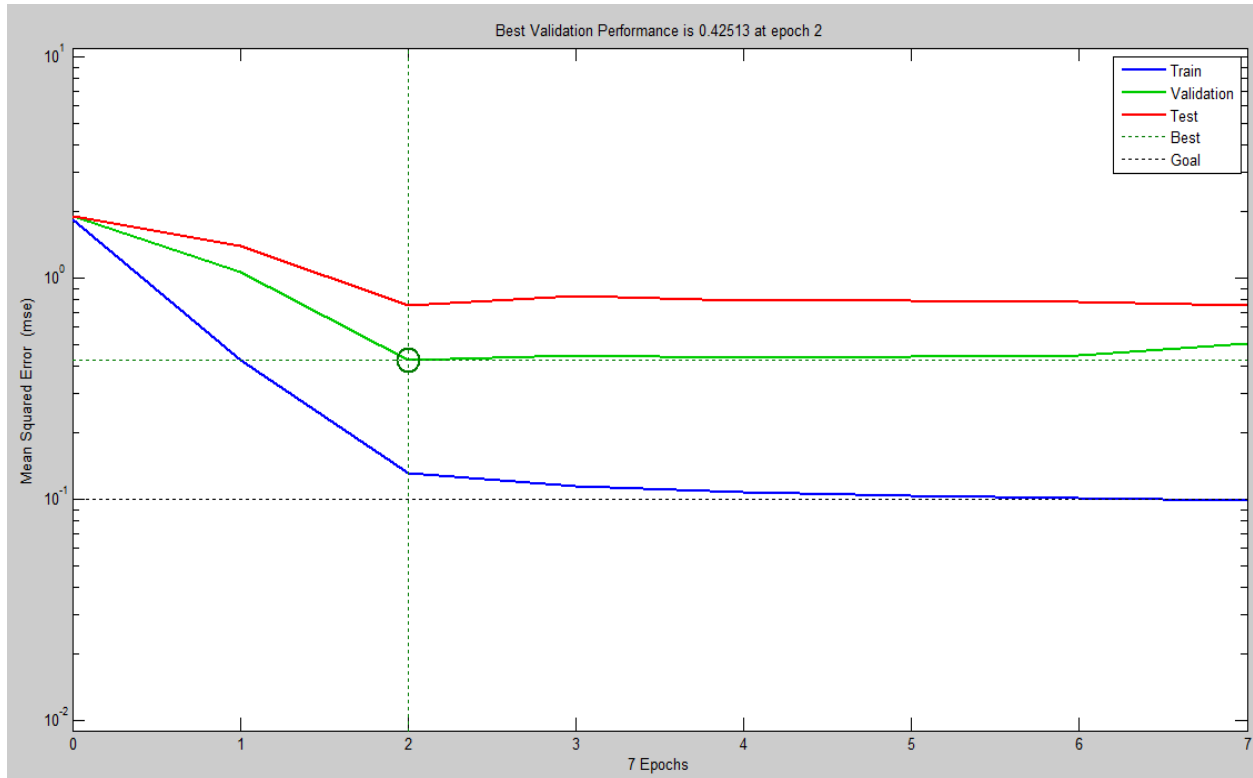
Figure 5.15: Performance plots for ANNs training errors for cascade correlation.

From the plot, the blue line shows the training, the green shows the validation while the red line shows the testing analysis of the model. All the lines are as a result of the input data fed into the network getting divided into three sets; with 60 % for training the network, 20 % for validating the ability of the network to generalize and 20 % testing how the network will predict new sets of samples/ data. For this algorithm, the number of neurons were optimized at 3 since many neurons is often accompanied by over fitting while the contrast would not be able to do accurate classification.

Table 5.4: Analytical performance indices for different ANN models based on cascade correlation

Model	Number of neurons in hidden layer	MSE for best validation performance	Number of epoch	Correlation coefficients			
				Training R^2 value	Validation R^2 value	Test R^2 value	Overall R^2 value
A	1	96.29	1	0.832	0.731	0.840	0.841
B	2	87.08	2	0.881	0.866	0.816	0.852
C	3	68.64	2	0.765	0.851	0.824	0.861
D	4	45.27	3	0.892	0.868	0.772	0.835
E	5	23.93	1	0.787	0.841	0.842	0.821

The model with 3 neurons was used since it had the least mean square error that gave same R^2 value (0.86 threshold) for many trainings. Over-fitting automatically stopped when the validation error increased beyond the limit expected. The regression analysis showing how the network responded between the responses of the network with respect to the corresponding target is shown below.
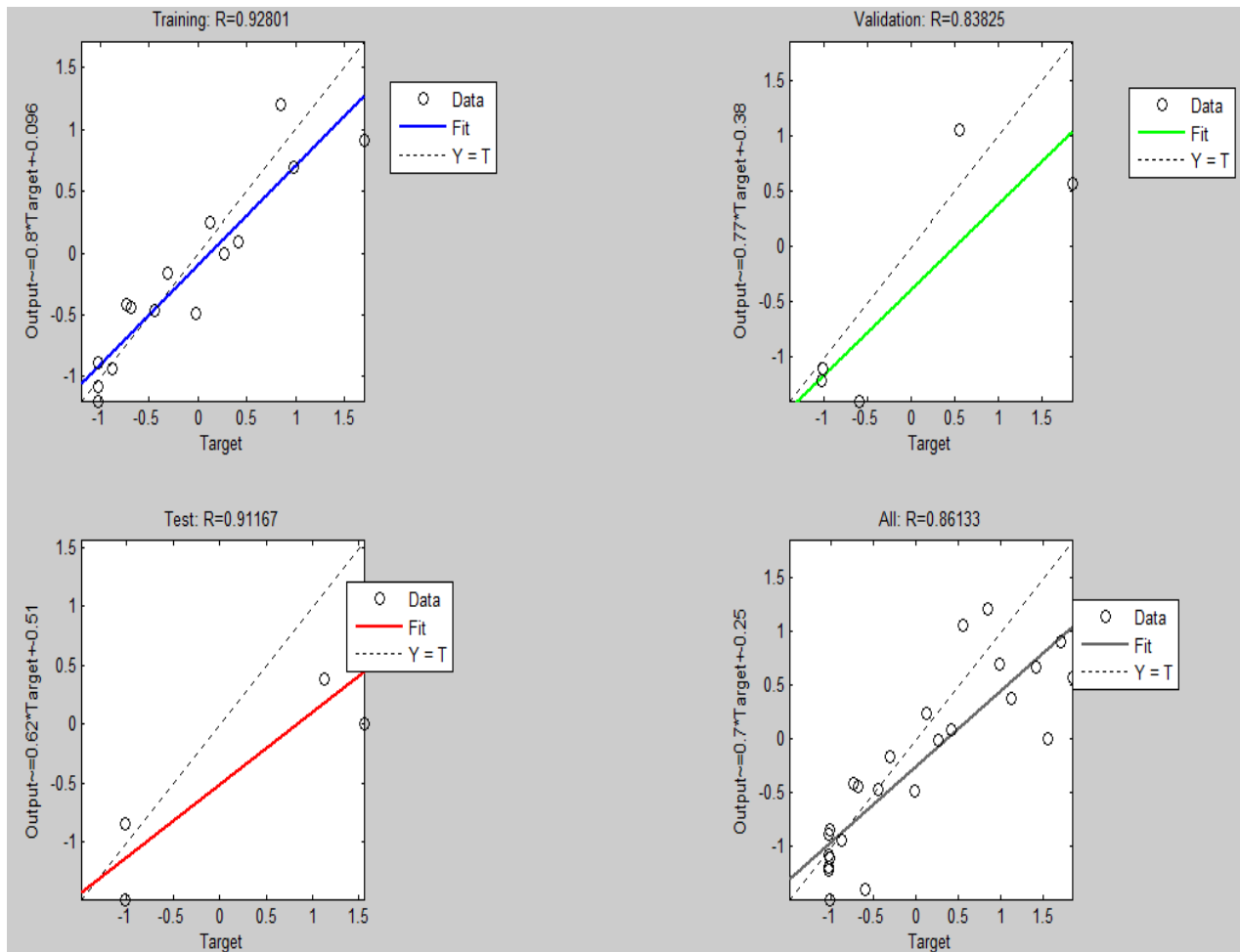
Figure 5.16: Cascade correlation regression plot for predicted verses known utilizing uranium bands.

It can be inferred that the cascade correlation doesn't give R^2 values close to 1 as it was for the BP-ANN. Both for training, validation and prediction respectively. This can be manifested with the overall R^2 value which was less than 90 % for the total response. Figure 5.17 shows the performance of the model on simulate samples.

R² = 0.974
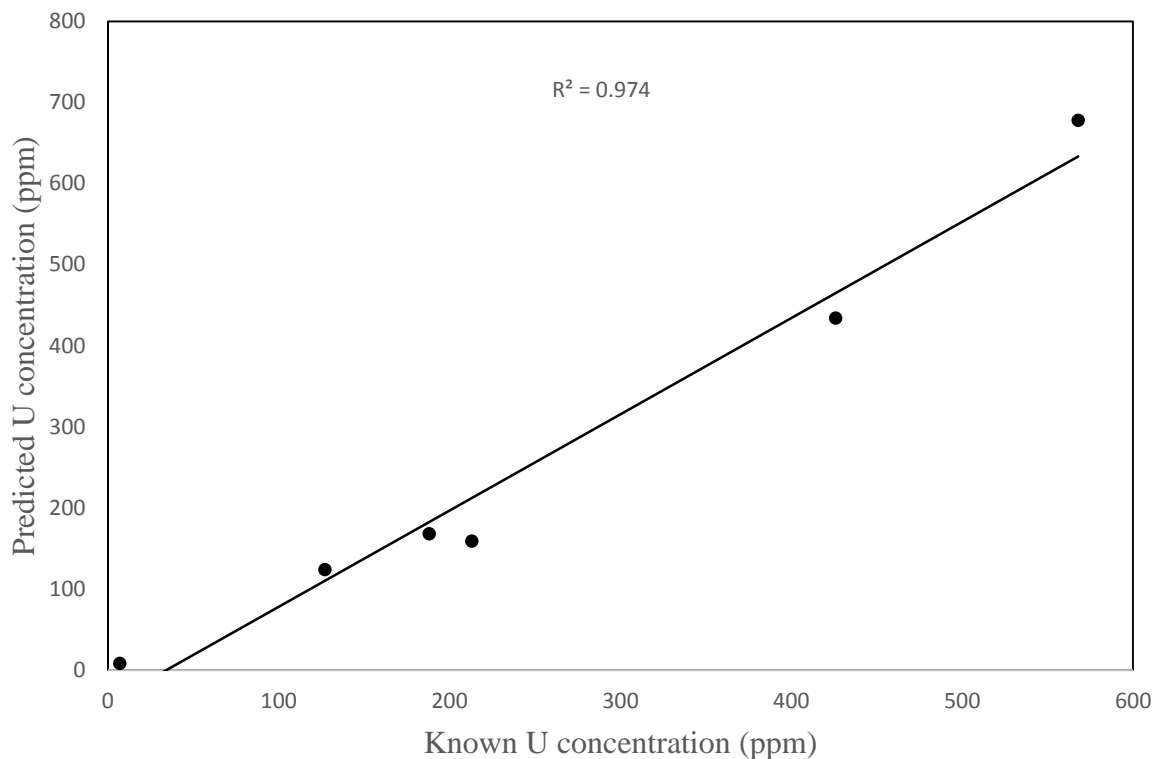
Figure 5.17: Cascade correlation regression plot for predicted against known uranium concentration using uranium bands.

After training the network based on the two algorithms (BP-ANN and cascade correlation), more simulate samples were made (most in the ppb) ranges to conform to the typical levels obtained in the field samples. The new feed forward algorithm was adopted in developing the calibration curve. The network was trained many times as it did not learn as fast as it did for high uranium concentrations. The network was however adopted after it predicted at an R^2 value of 0.896 as shown in Figure 5.18.
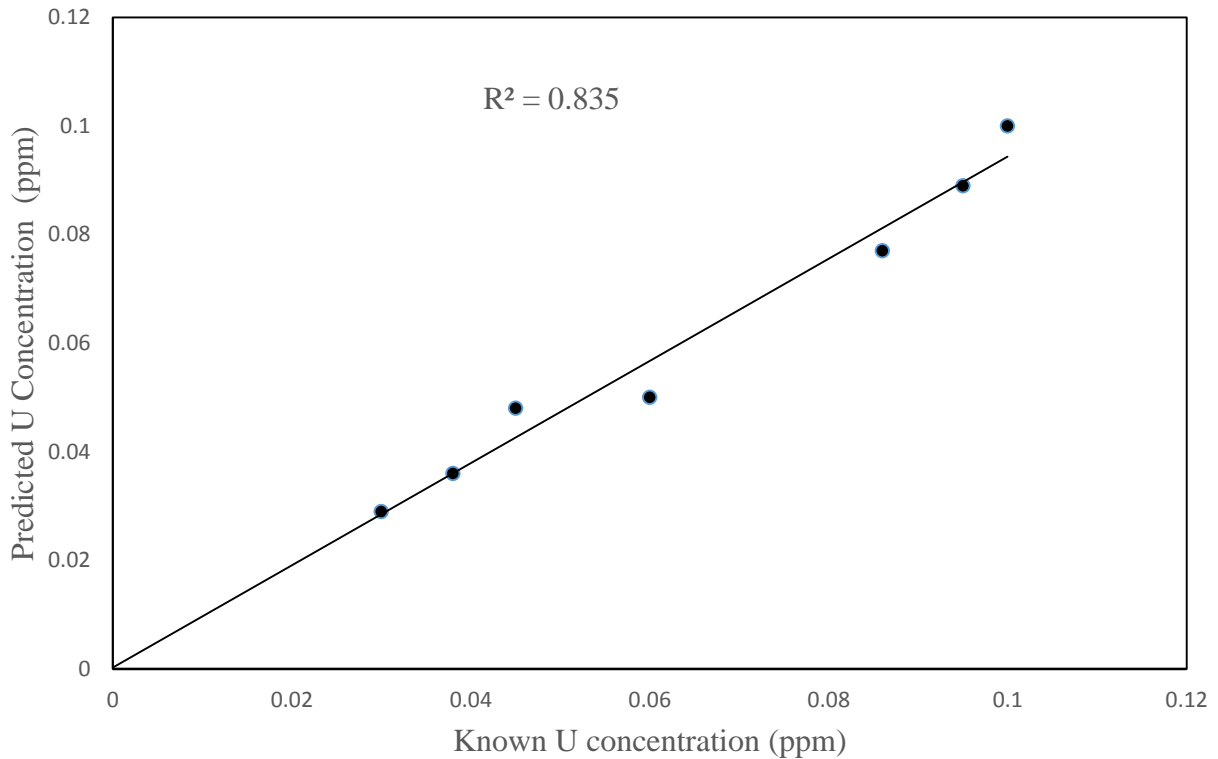
Figure 5.18: New feedforward regression plot for ppb concentration levels.

The observation we make is that BP-NFF algorithm performance is better than cascade correlation since it takes shorter time with a better predictive ability. The argument we can give is that since the CC automatically increases the number of hidden neurons, it took time for the network to learn and adapt to the new hidden neurons. Since the algorithm trains a single hidden layer at a time, the residual output errors took long to be eliminated hence affecting its predictive ability. On the other hand, since BP-ANN allows one to set his own number of hidden neurons, it took less time to adapt to learn. The accuracy of the model was validated using the relative error of prediction based on equation 5.2 by Dingari *et al.* (2012).

$$REP = \frac{100}{N} \sum_{i=1}^{N} \left| \frac{\hat{c_i} - c_i}{c_i} \right|$$

$$(5.2)$$

Where $\hat{c_i}$ is the predicted concentration while c_i represents the measured(real) analyte concentration. N refers to the number of samples hidden from the network. The REP was obtained to be 8.76%.

5.9 Raman Spectra of Field Samples

Raman spectra were acquired by focusing the laser successively on well selected particulates after measuring their sizes using the measuring component of the Raman video monitor. The individual particles were measured from end to end and the value given in μm. For every cut size, twenty particles were chosen and for every individual aerosol particle, fifteen laser shots were acquired and averaged into one spectrum.

As shown in Figure 5.19 and Figure 5.20, the Raman scatter peaks for field samples for the uranium bands were not clearly noticeable both for $PM_{4.5}$ and $PM_{2.5}$. This were attributed to the very low concentrations of uranium in the aerosols. There was no difference in the spectral profiles when both lasers were used. However, multivariate techniques have the potential to extract information of the analytes from such spectral data.
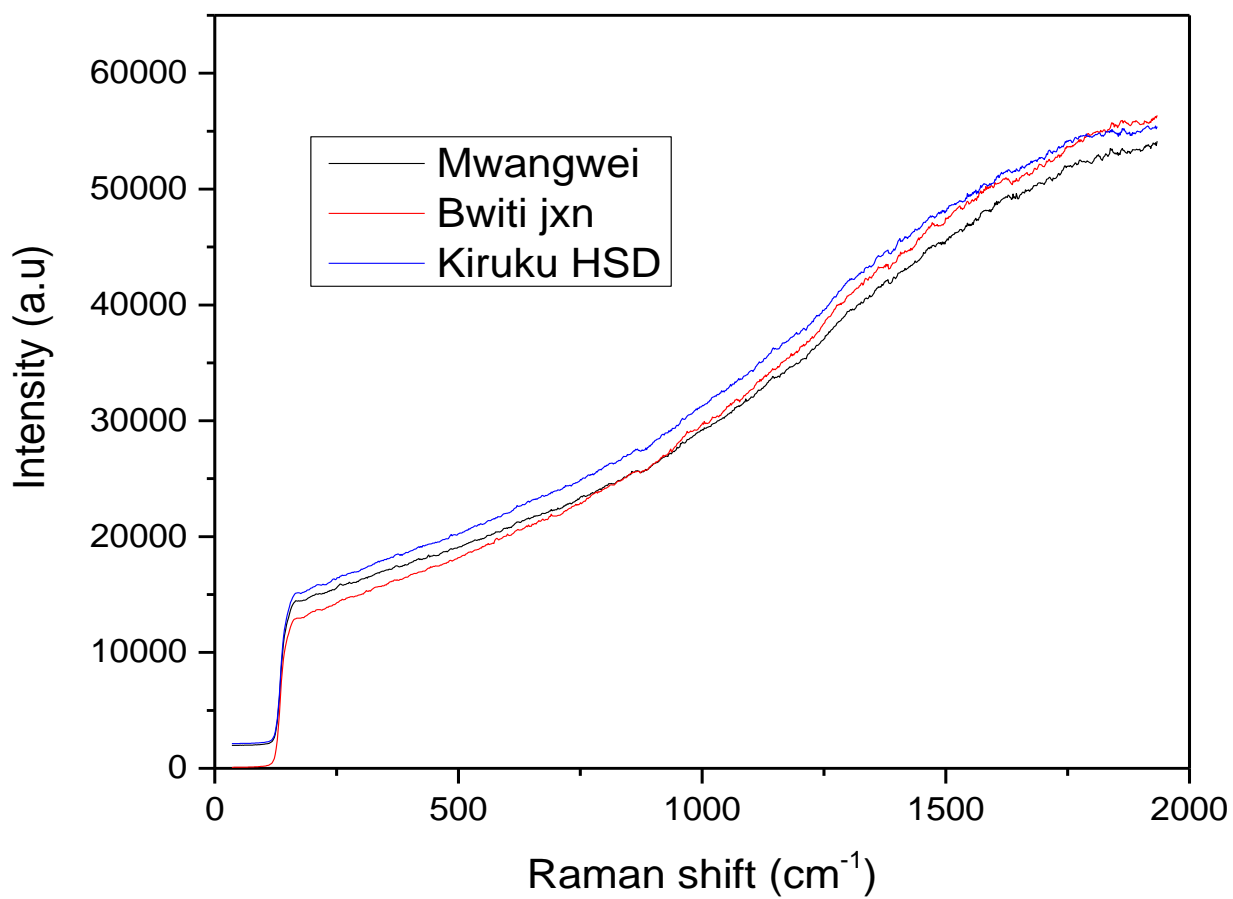
Figure 5.19: Raman spectra of PM$_{2.5}$ field aerosol samples using 532 nm laser.
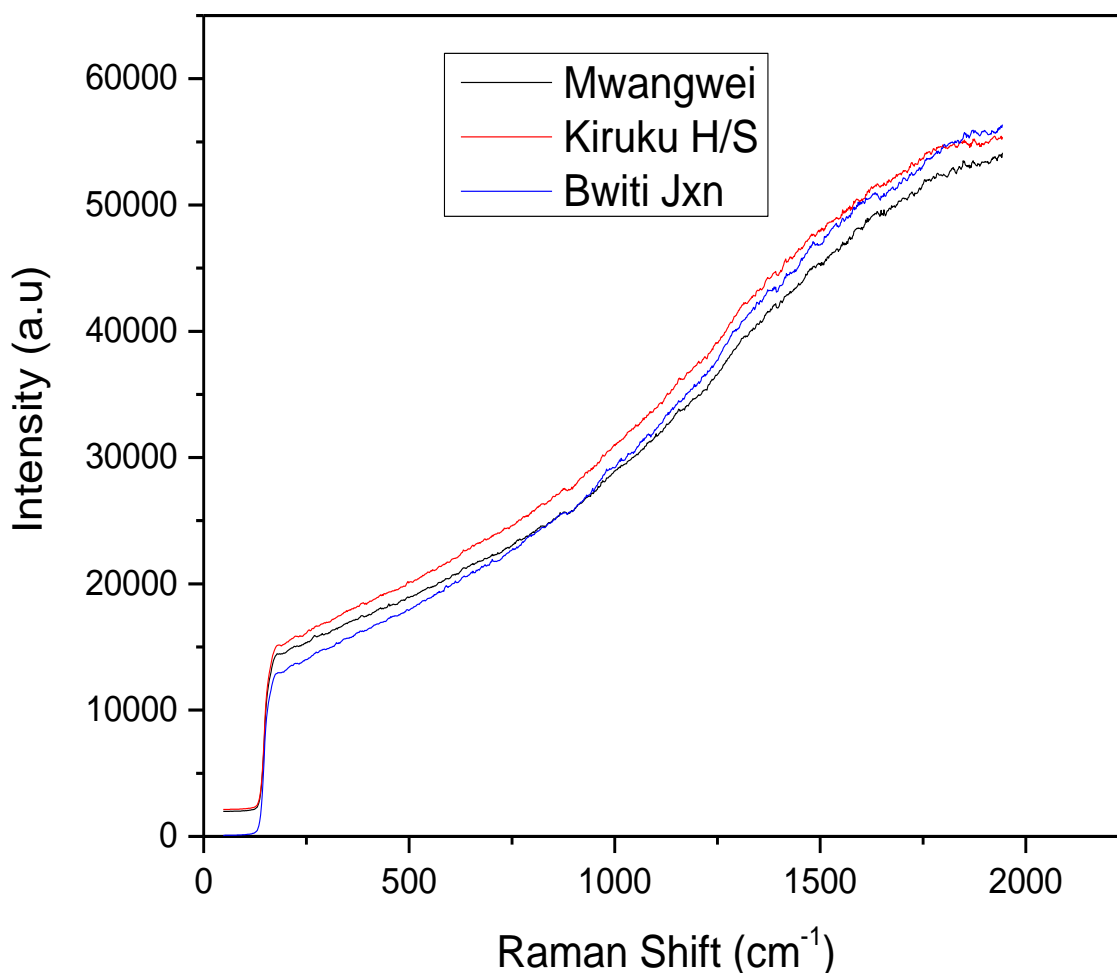
Figure 5.20: Raman Spectra of $PM_{4.5}$ field aerosol particles using 532 nm laser.

The absence of not only the uranium scatter bands but also those of the anions normally associated with aerosol particles, presents the technicality that there is in carrying out quantitative analysis using Raman by relying on the "peak" intensity. Even though confocal laser Raman spectroscopy has the potential to carry out quantitative analysis, there lies a challenge when the sample concentrations are in trace levels. This lack of bands motivated the use of MCR-ALS that has the potential to resolve the peaks relevant for uranium as will be discussed in section 5.14

5.10 Pictograph of Aerosol Samples

Figure 5.21 shows the photomicrographs of blank substrate and a loaded substrate. From the graph of the loaded substrate, it is clear that the particles could be clearly seen using the microscope. This therefore made it possible to focus a laser on individual particles by utilizing the laser spot diameter.
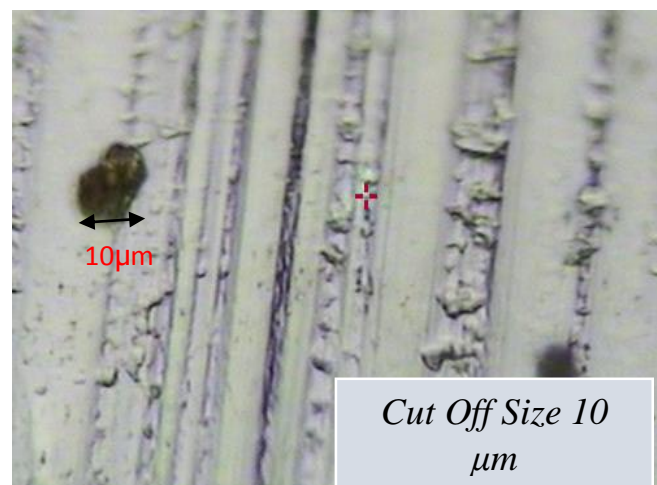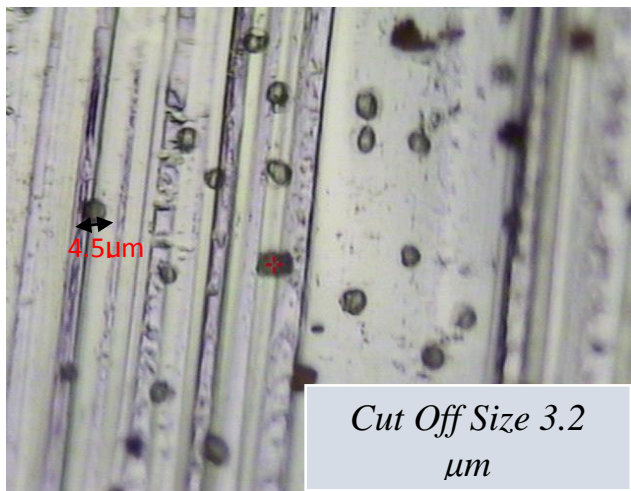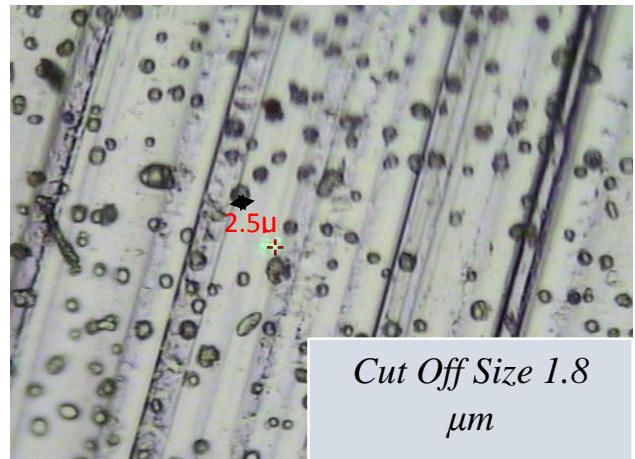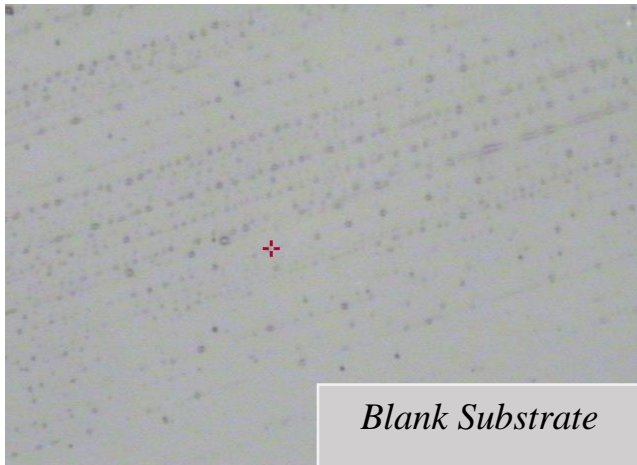
Figure 5.21:Pictographs of aerosol particles impacted under different cut sizes as observed using x50 objective lens.

It can be seen that the number of particles impacted on the substrates progessively decreases with the increase in cut size . This could be attributed to the ambient environment having more particles in the fine and hyperfine range as compared to the coarse range. Also, since the sampling time allowed was limited putting in mind that the sampler we had was a low volume aerosol sampler, the bigger particles that need a higher streamline force to be impacted rarely got to the substrate.

It could also be explained from the impaction force and the nature of the substrate. Bigger particles could not be sustained by the substrate hence some particles fell off.

5.10.1 Agglomeration of Aerosol Particles

One of the advantages of utilizing Raman is the ability to focus on individual aerosol particles. However, as seen Figure 5.22, agglomeration can be a great challenge in achieving this. In this work, we limited the sampling time to avoid particle agglomeration so that individual particles could be seen when carryimg out Raman measurements. However, for most of the samples on the road site, there was a lot of agglomeration of particles, most of which were full of black carbon as a result of the smoke emanating from the passing vehicles and motorcycles. Such places also experienced a lot of dustlift and as such the substrate loadings bore a higher mass as compared to other regions away from the road sides (Table 5.9). Figure 5.22 shows a sample from Mwangwei centre, for 4.5 µm cut size. At points with such agglomeration, it was not possible to do point spectroscopy on individual aerosol particles. This was very contrary to particles collected from fields away from the road sides such as the Kiruku hill apex. Morphology therefore is an imporatant aspect that helps in explaining source attribution. To achieve this, agglomerated regions were avoided and focus shifted to individual size fractions.
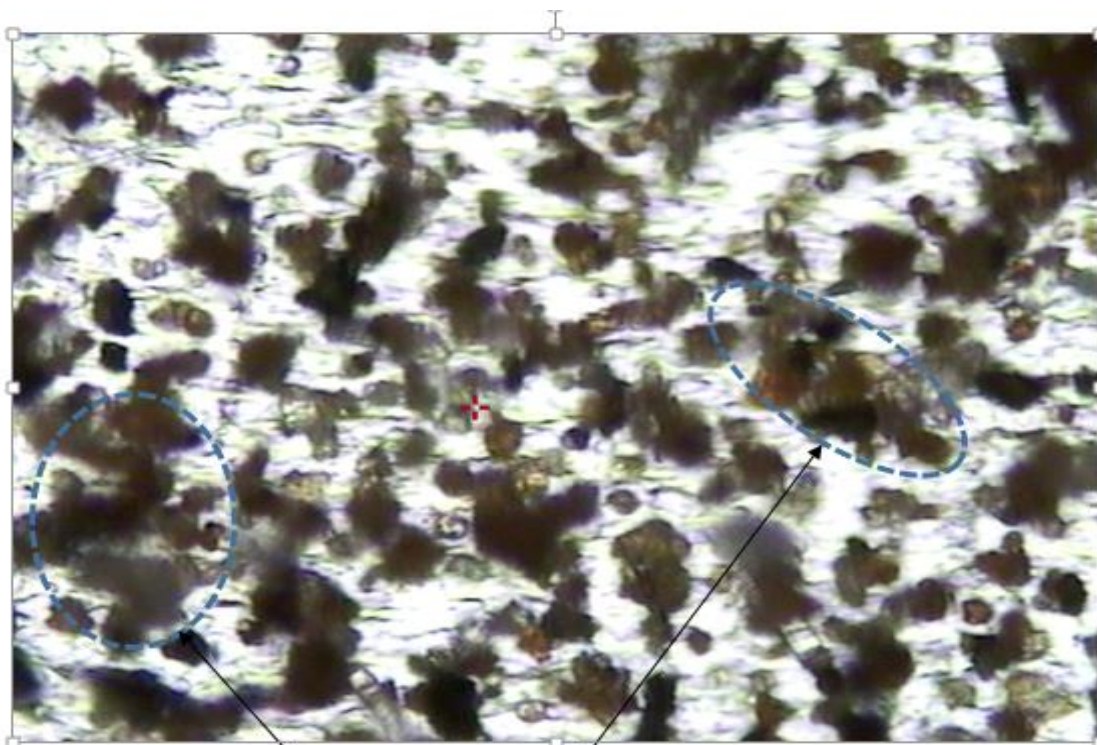
Particles that have undergone
agglomeration

Figure 5.22: Microscopic image showing agglomeration of particles.

5.11 PCA Analysis on $PM_{2.5}$ and $PM_{4.5}$ Aerosol Particulate Matter

PCA was employed on all the field samples for both $PM_{2.5}$ and $PM_{4.5}$ (before feature selection) to explore the size distribution of atmospheric particulates, together with their intrinsic chemical characteristics that are responsible for any variations within the two particle sizes. The aim of this PCA was therefore to help analyze the size distribution of atmospheric particulates with their associated chemical content and to identify the potential sources of the particulates based on their

scores and loadings with the aim of understanding their role in NF. The score plot is as shown in Figure 5.23.
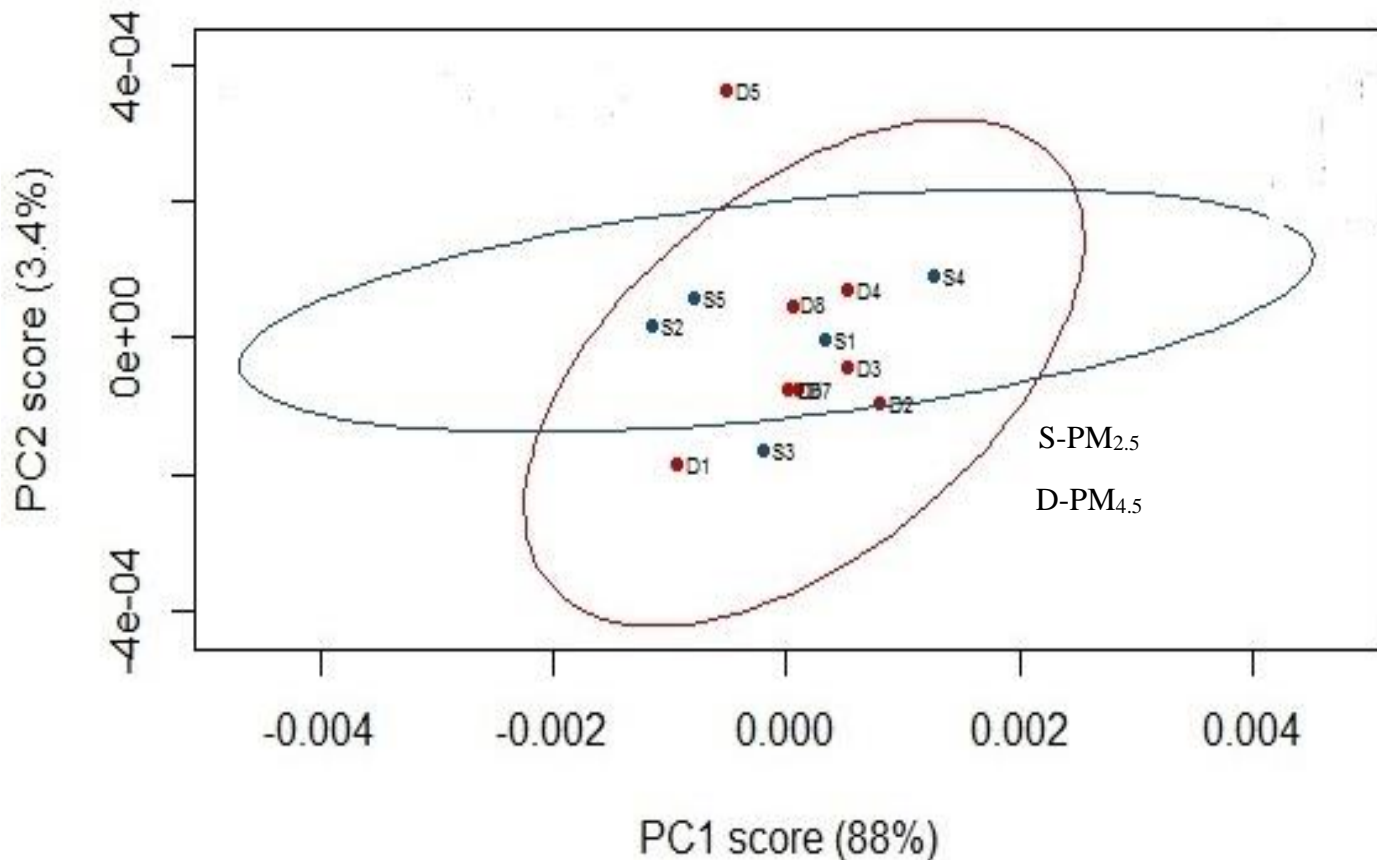
Figure 5.23: PCA score plot for field samples for PM $_{2.5}$ and PM$_{45}$.

From the score plot, there is no distinct cluster of the two particle sizes. However, the positive of PC-1 has received a lot of influence from most of the PM$_{4.5}$ particles other than D1 which is a control as well as D5 (from Mrima tarmac) which is an outlier. From the loadings plot, the positive of PC-1 has been influenced by Raman scatter bands from 600 to 890. This is a mixed of influence from both U-O bands as well as bands associated with chlorides. On the other hand, the negative side of PC-1 is as a result of Raman scatter bands from 900 to 1200. Even though most of bands here are associated with anions, a band around 1180 has been associated with uranyl chloride as

per table 5.1. This implies that the sampling source field was dominated with chloride based uranium particles.
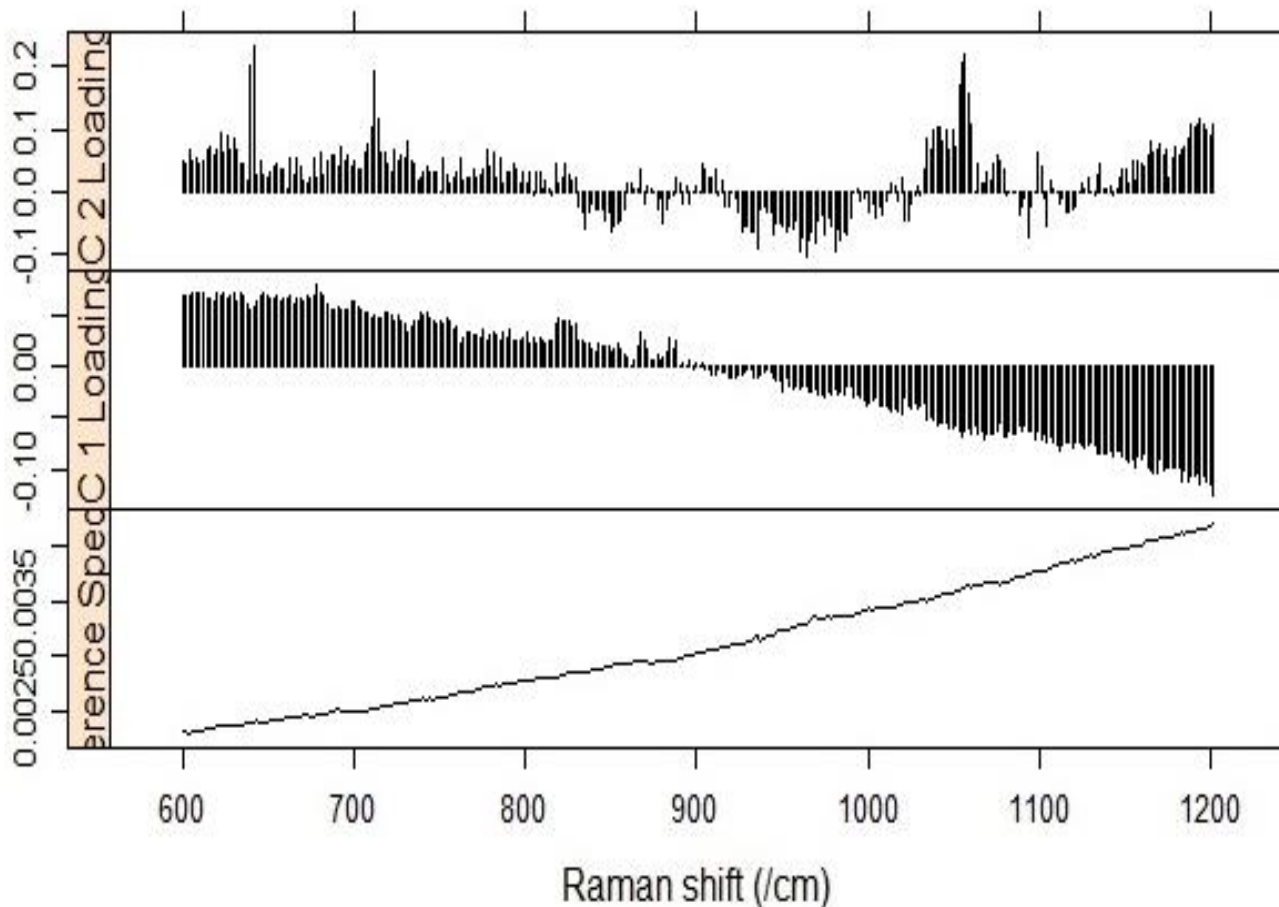
Figure 5.24: Loadings plot for PC-1 and PC-2 for field samples.

The general PCA before feature selection has therefore proven not to be an efficient way to apportion the two particle sizes in view of nuclear forensic applications.

5.11.1 PCA on PM$_{2.5}$ and PM$_{4.5}$ after Feature Selection

PCA was employed on uranium specific bands that were identified as nuclear forensic signatures expected in typical uranium bearing aerosol. The purpose of this PCA was to apportion different

particulate sizes to "a nuclear facility" based on their uranium signature. The score plot shows two

clusters with $PM_{2.5}$ clustered together other than S2 that was a sample from a control cite. The

clustering can be explained based on PC-1 alone. The score plot is shown in Figure 5.25.
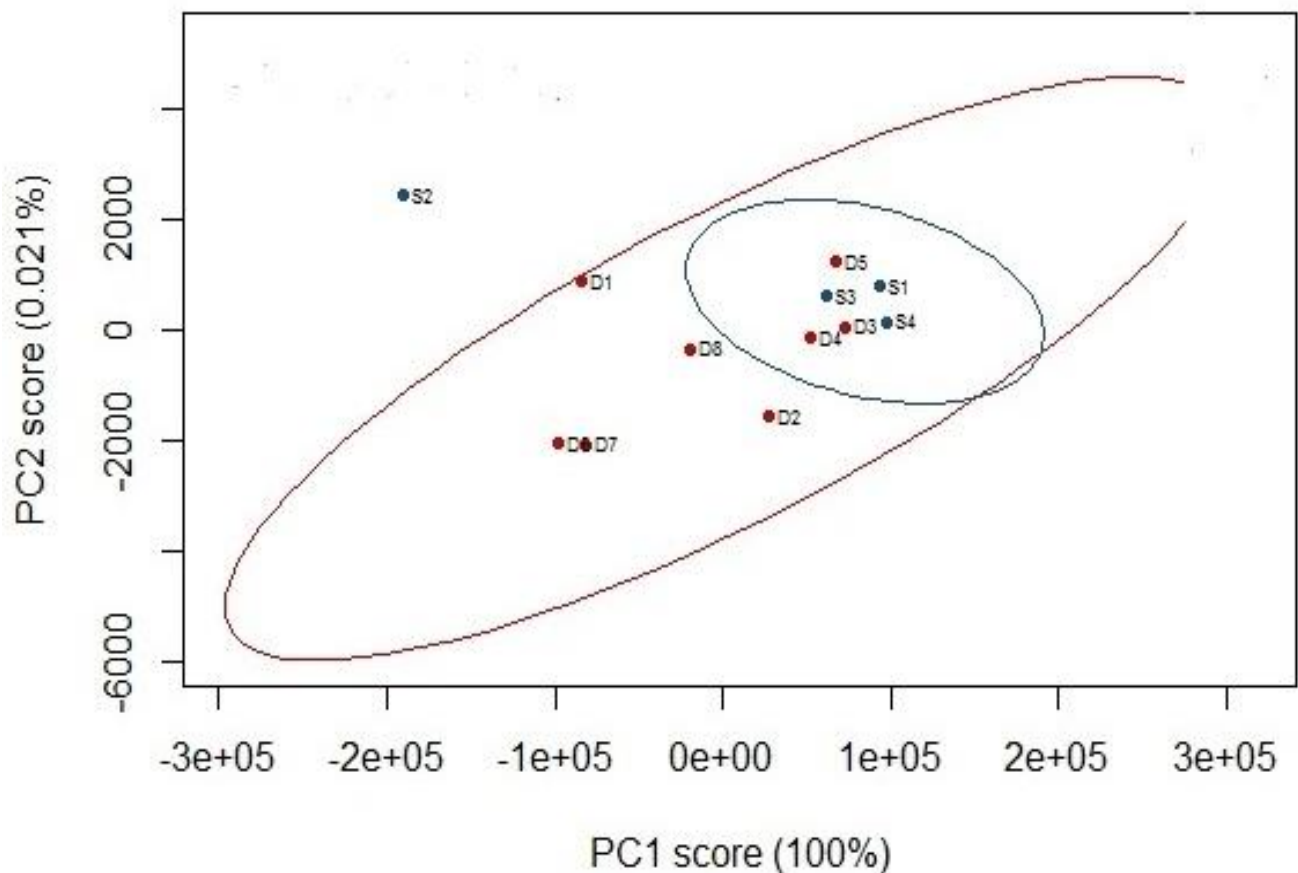
Figure 5.25: PCA on $PM_{2.5}$ and $PM_{4.5}$ after feature selection.

From the score plot, all $PM_{2.5}$ particles (other than the control, S2), and some $PM_{4.5}$ particles (D2,

D3, D4 and D5) which were sampled from Kiruku homestead, Kiruku apex, Mwavobo primary

and Mrima tarmac are on the positive side of PC-1. From the loadings plot in Figure 5.26, the

positive side of PC-1 is characterized by scatter bands 808/814, 840/846 and a band around 858cm-

[1]. These bands have been assigned to uranyl chloride, U-O, and uranyl chloride respectively. The

PM$_{4.5}$ on the negative side of PC-1 are samples from Eden Place, Mwangwei junction, Kenana

market and Bwiti junction. All these samples are from road sides and are characterized by a band
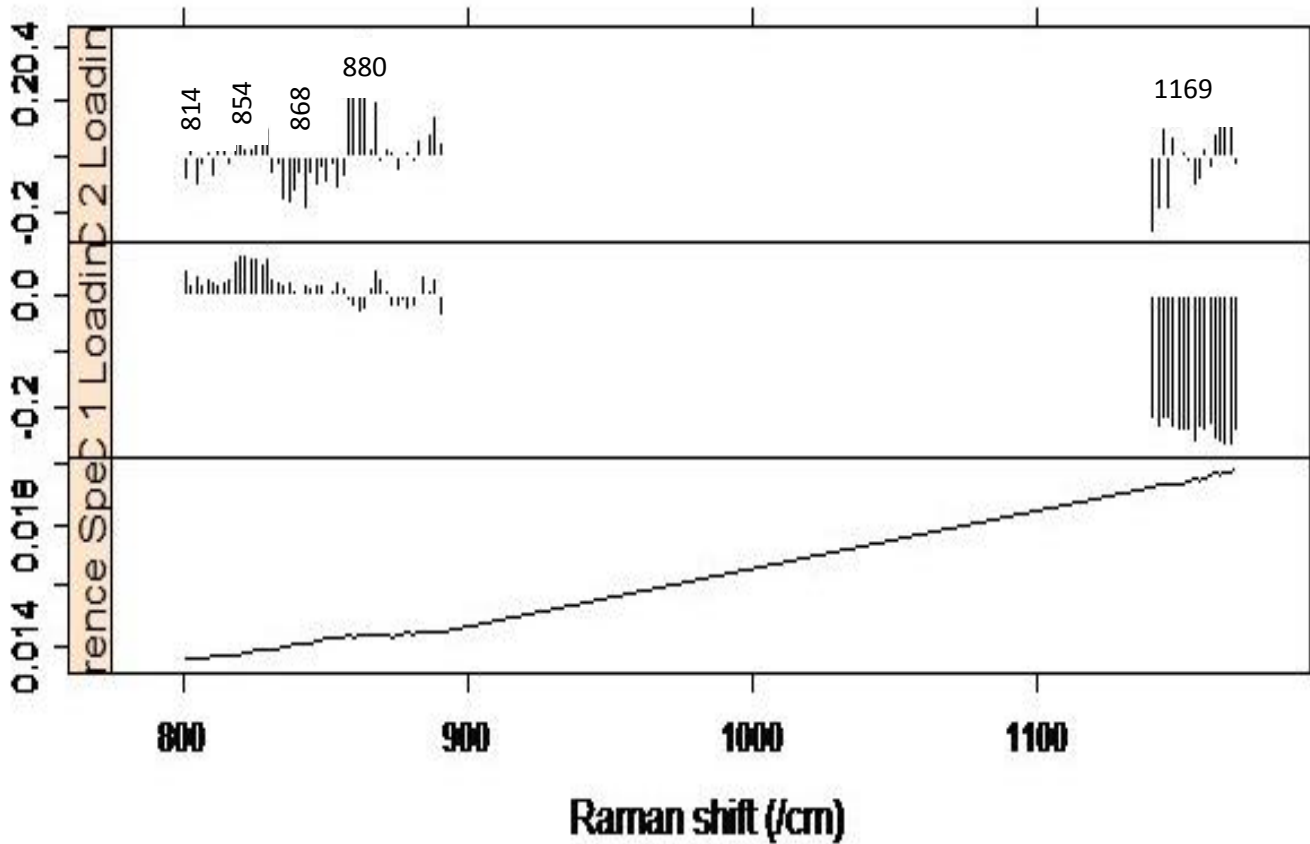
at 1169cm^{-1} which is specific for uranyl chloride that always overlaps with a C-O bond.

Figure 5.26: Loadings plot for PM$_{2.5}$ and PM$_{4.5}$ after feature selection.

Based on the scores and loading plot above, we can conclude that most PM$_{2.5}$ cluster together with

PM$_{4.5}$ that were sampled away from road sides and all are characterized by uranium specific bands

and especially uranyl chloride. On the other hand, PM$_{4.5}$ sampled from road sides have a common

intrinsic feature (probably full of C-O Raman scatter bands) and that is why they cluster together

away from other particulate matter. An interesting feature is how all PM$_{2.5}$ (both from road sides

and away) are clustered together and the loadings plot show that the influence of this cluster is as

a result of uranyl chloride Raman scatter bands.

5.11.2 PCA on PM$_{4.5}$ after Feature Selection

PCA was employed on PM$_{4.5}$ particle data so as to: identify particle clusters that can be differentiated on the basis of their chemical composition with a view of evaluating the differences among the seven sampling sites. The PCA was based on the feature selected finger print region of uranium. The information on the clustering can be explained by 64 % PC-1, 12 % of PC-2 and 6.2 % PC-3 which forms close to 83 % of the information which was enough to explain the clustering.
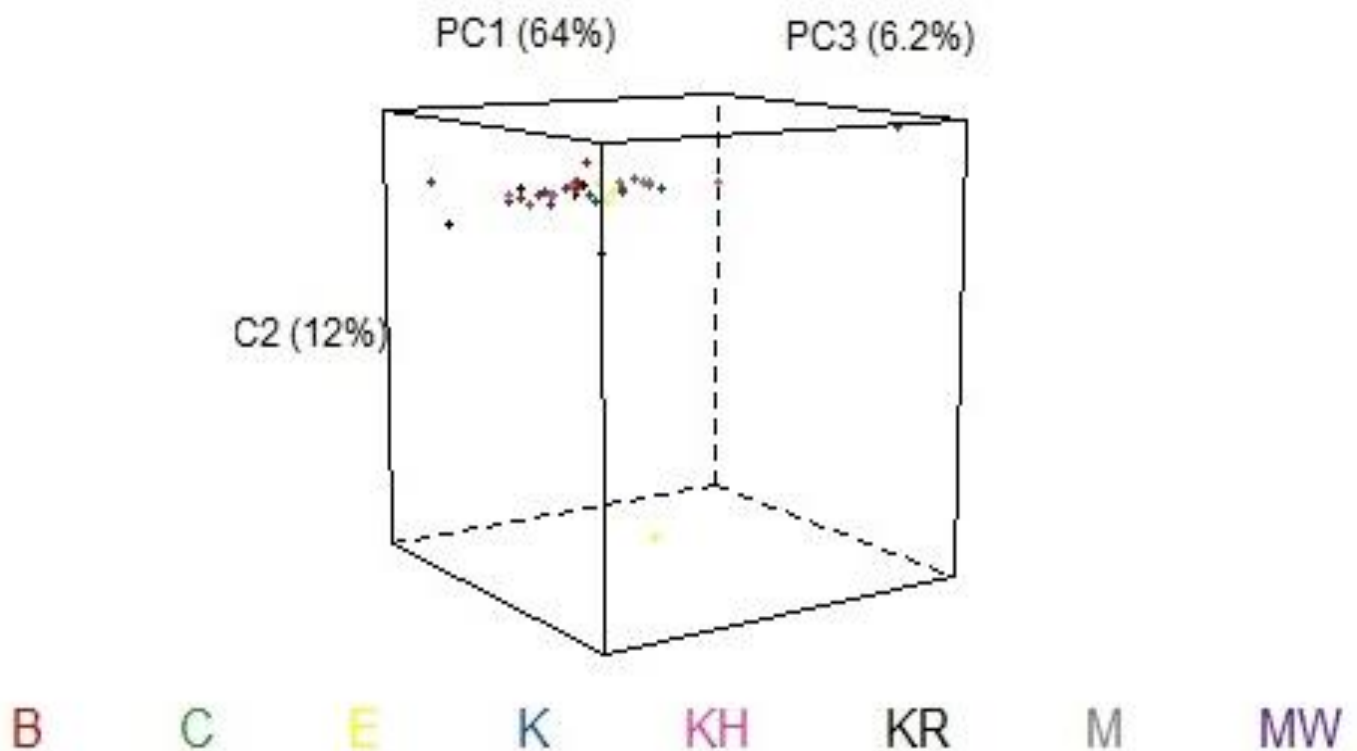
Figure 5.27: 3-D Score Plot for PM$_{4.5}$ particulate matter.

B-Bwiti junction

C-Chiromo

E-Eden place

K-Kenana market

KH-Kiruku homestead

KR-Kiruku Apex

M-Mwangwei junction

MW-Mwavobo primary

From the score plot, the field samples clumped together in such a way that it was hard to obtain their distinct clusters. Almost all of the samples (other than few from Bwiti junction, Kiruku hill and Kiruku Homestead) are classified on the negative side of PC-1. From the loadings plot, the negative PCs from PC-1 are influenced by peaks at 1352cm^{-1} which is for standard graphite carbon probably from moving vehicles along the sampled roadways. The clustering of the control sample together with the other samples shows the great influence that motor vehicle emissions have on particulate matter. The clustering can be explained from the loadings plot in Figure 5.28.
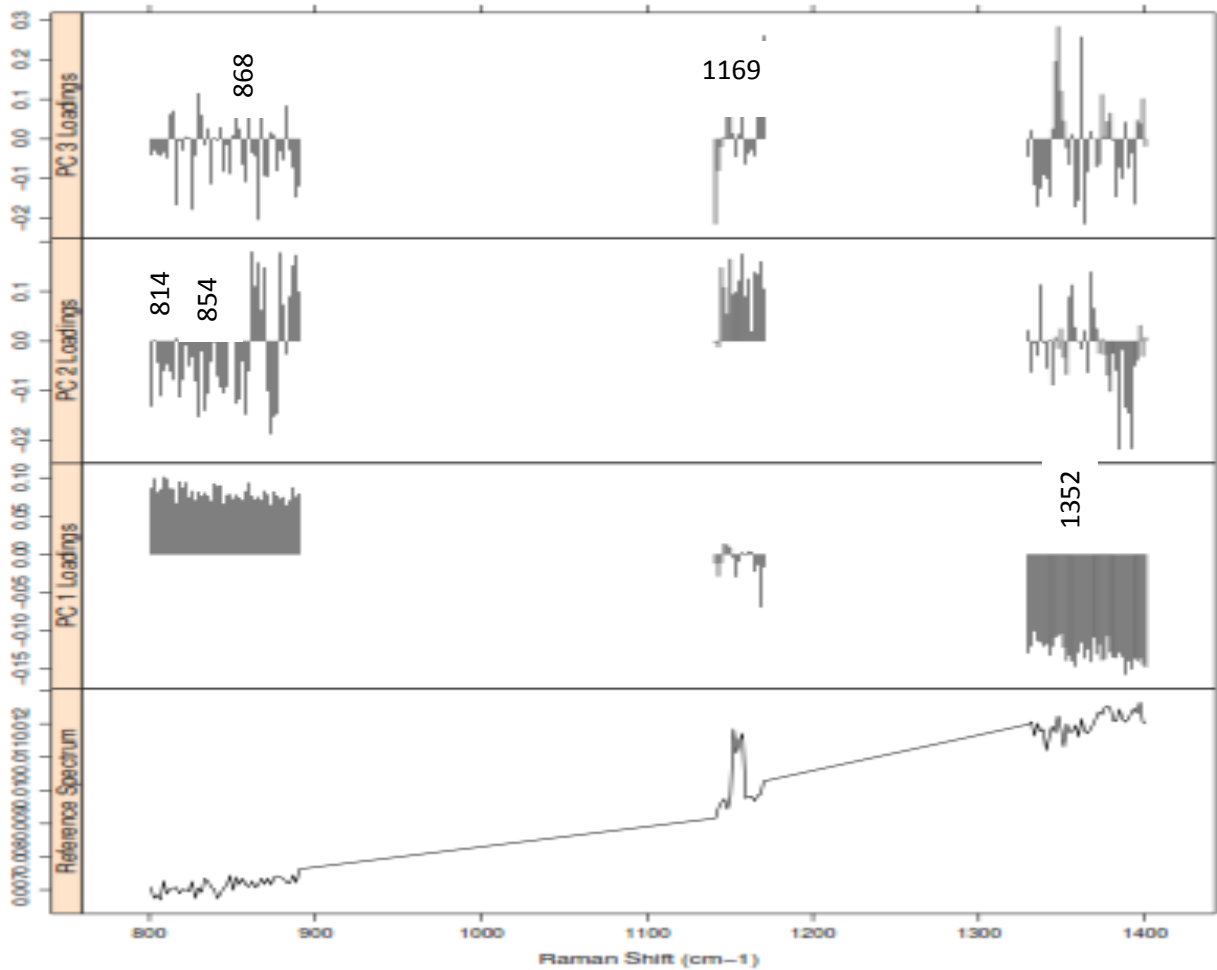
Figure 5.28: Loadings plot for PC-1(64%) PC-2 (12%) and PC-3 (6.2%).

5.11.3 PCA on PM$_{2.5}$ After Feature Selection

The objective of carrying out PCA on PM$_{2.5}$ was similar to the PCA for PM$_{4.5}$. Moreover, the PCA

was carried out to try and provide information on the sources of PM. Fig 5.26 shows the score plot
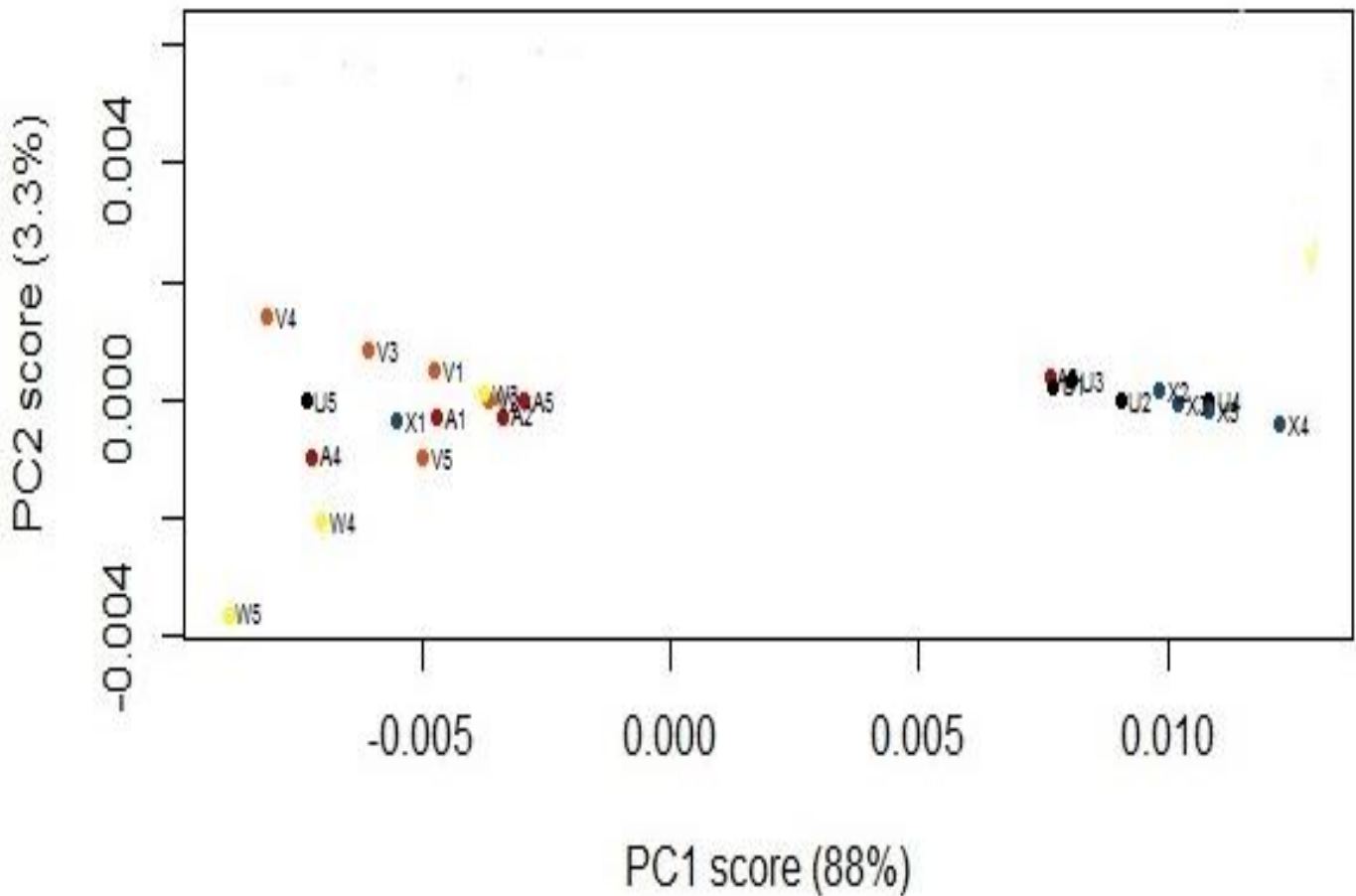
Figure 5.29: PC-1(88%) and PC-2(3.3%) for all PM$_{2.5}$ aerosol particles.

X- Kiruku Hill Apex

U- Kiruku homestead

W- Mwavobo

V- Kenana market

A- Mwangwei junction

All samples from Kiruku Apex(X) and Kiruku homestead (U) have been delineated from the other samples basing on the positive of PC1 which accounts for 88 % of the variables. From the loadings plot, this clustering is based on a band at 868 cm^{-1}, 890 cm^{-1} and 1154 cm^{-1} that are assigned to uranyl chloride, un-assigned and uranyl chloride/sulphate respectively. Therefore, this suggests that samples from Kiruku hill Apex and Kiruku Homestead have a higher likelihood to have been influenced by sea spray. All other PM$_{2.5}$ particulate matter are on the negative side of PC-1. From the loadings plot, the negative side of PC-1 is still as a result of uranium scatter bands. The bands are at around 808/814 and 846 cm^{-1} all of which are assigned to uranyl chloride as shown in the summary Table 5.1 and 5.2. This implies that PM$_{2.5}$ samples are enriched with sea salt ions as a result of sea spray.
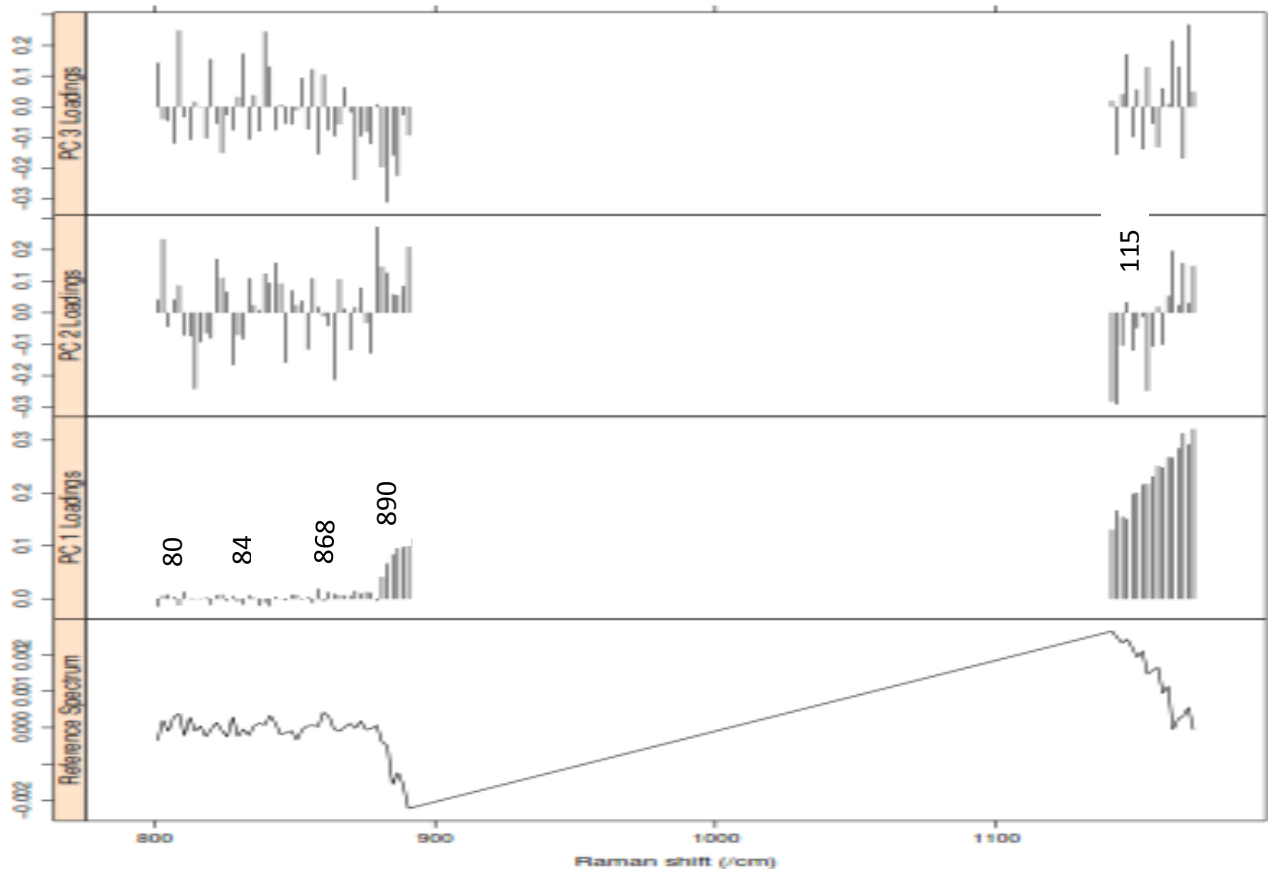
Figure 5.30: Loadings plot PC1 (88 %) and PC2 (3.3 %) for PM$_{2.5}$ aerosol particles.

In view of Nuclear Forensics, the PCA results shows that the developed method can be applied to distinguish samples with similar composition yet they are from different nuclear facilities. The results can also extend to imply that PCA algorithm (based on feature selected uranium fingerprint region) can be used to distinguish samples that have the same composition but yet produced by different facilities or even different countries.

5.11.4 The Sea as a Source of Uranium

The potential for uranium extraction from sea water is vast owing to advances in nuclear technology. The Pacific Northwest National Laboratory for example extracted 5g of yellow cake from ordinary sea water which was a major breakthrough in nuclear energy (Furness, 1990). In high background radiation areas, the sea bedrock; just like the adjacent land (rock and soil) has elevated levels of uranium. During evaporation of surface water, the water condenses around particles in air and travel long distances. Owing to the presence of Raman scatter bands associated with uranium and chloride bonds in the loadings plot, it could be concluded that the source of uranium is associated with sea spray.

5.12 Analysis of IAEA RGU-1 mix using ANNs

Triplicate synthetic standards were developed. The accuracy of the developed method was evaluated through analysis of the synthetic standard reference material (IAEA-RGU-1) uranium ore that was prepared under the same conditions of the simulate samples. The uranium concentration was obtained to be in good agreement (<10%) with the certified value. Developed model predicted the concentration as 89± 3.2 ppb while the certified value was 100 ppb. The percentage deviation from certified value was 9.25%.

5.13 Uranium Concentration in Field Samples

After exploration of data using PCA, testing and validating the developed quantitative analytical model, the data from field samples was input into the model to predict the uranium concentration. Table 5.5 summarizes the data obtained from the field and the subsequent uranium concentrations obtained using the developed model.

Table 5.5: ANN Predicted uranium concentrations in the aerosol samples from the field

Sampling Points	Sampling time	Load (mg)	Uranium concentration (ppb)		Volume of air sampled (L)
			$PM_{4.5}$	$PM_{2.5}$	
Eden Place	4 hrs 01 min	0.096	168.2±12.4	102.5±4.8	976.0
Mwavobo Primary School	1 hr 57min	0.094	800.4±40.6	684.6±38.9	470.0
Kiruku (homestead)	2 hrs 50 min	0.093	642.8±24.8	356.8±14.2	683.5
Kiruku hill (apex)	3 hrs 20 min	0.095	504.6±32.7	380.6±11.7	780.0
Mwangwei centre	3 hrs 54 min	0.092	487.4±23.4	298.3±17.8	938.2
Bwiti junction	3 hrs	0.094	490.0 ± 43.8	302.7±11.9	720.0
Kenana market	3 hrs 01min	0.092	426.8±12.2	243.1±11.6	727.0
Chiromo (control)	4 hrs	0.096	BDL	BDL	975.0

An important outcome of the results is the consistent high uranium concentrations in the bigger particles ($PM_{4.5}$) as compared to the smaller particles. This fractionation/partitioning can be related to the aerosol formation mechanism (Di Lemma *et al.*, 2015). The concentration in the bigger particles could have been enhanced since most of the particles were as a result of the dust lift and the crustal resuspension from the parent materials (soils or rocks) – especially for roadside samples and human related activities such as farming (for homesteads). On the other hand, $PM_{2.5}$ particles generally had lower uranium concentrations since most were characterized by high sea salt ions (refer to section 5.11) implying that they were not from the immediate ambient. The sampling sites that were along the roads (Kenana market, Mwangwei junction and Bwiti junction) had the uranium levels that were very close. Along these roads, the geology of the soils (hence subsequent similarity in crustal resuspension) were the same and therefore there were no external factors that could have influenced a big variation in the levels. The closeness of the uranium levels also proves that the sampled particulates were from the ambient environment which is HBRA.

The uranium levels obtained using the model for the aerosol samples were consistent with what other authors have obtained in the vicinity of nuclear facilities. Concentration of uranium in aerosols near a nuclear facility has been reported as (364 – 542 ppb), 364.5ppb to 542.7 ppb (Jeambrun *et al.*, 2012) and 810 ppb (Bellis *et al.*, 2001).

5.13.1 The Average Concentration of Uranium in ppb/cm³.

Measures of aersol concentrations are normally given in some integral form which in this case will be ppb/cm³. Since the particles were selected carefully based on the sizes (measured using Raman), and several laser shots shot for about ten particles per sampling point, the uranium concentrations presented are an average of the ten particles having the same size from the same sampling site. To

convert from ppb for the individual particles to ppb/cm^3, the formula used was by Clerbaux *et al.*

(2009) as $1\,ppb = 2.46*10^6\,molecules\,/\,cm^3$. Based on the formula, the concentration

levels with their uncertainty was as in Table 5.6.

Table 5.6: ANN predicted uranium concentrations (in ppb/cm^3) for the aerosol samples from the field.

Sampling Points	Sampling time	Load (mg)	Uranium concentration (ppb/cm^3)	
			PM$_{4.5}$ (x 10^8)	PM$_{2.5}$ (x10^8)
Eden Place	4 hrs 01 min	0.096	4.41±0.8	2.52±0.4
Mwavobo primary School	1hr 57min	0.094	19.69±3.8	16.84±2.8
Kiruku homestead	2 hrs 50 min	0.093	15.79±2.4	8.78±2.4
Kiruku hill (apex)	3 hrs 20 min	0.095	12.41±1.9	9.36±3.6
Mwangwei centre	3 hrs 54min	0.092	11.99±0.2	7.34±1.6
Bwiti junction	3hrs	0.094	12.05±2.1	7.43±2.7
Kenana market	3 hrs 01min	0.092	10.49±1.3	5.98±2.2
Chiromo(control)	4hrs	0.096	BDL	BDL

5.14 Spectral and Spatial Characterization of Aerosols

The purpose of this section was to characterize aerosol particles in order to identify the pure chemical components (uranium-specific) by use of multivariate curve resolution and alternate least squares (MCR-ALS). Data acquisition entailed point by point (approximately 0.1 μm step size) Raman scanning acquisition on 4.5μm particles generating a set of 158 pixel spectra as shown in Figure 5.31 by using 532 nm laser with x100 0bjective (0.55 numerical aperture). Each pixel Raman spectrum is characteristic of the information obtained from an approximately 1 μm^2 sample surface. As shown in Figure 5.31, the spectra in the D-matrix has completely no peaks characteristic of the chemical components within the aerosol particles. Qualitatively, this implies that it is difficult to spectrally detect any of the chemical species including uranium. We tried to overcome this challenge by utilizing the Raman scatter bands specific for uranium compounds.
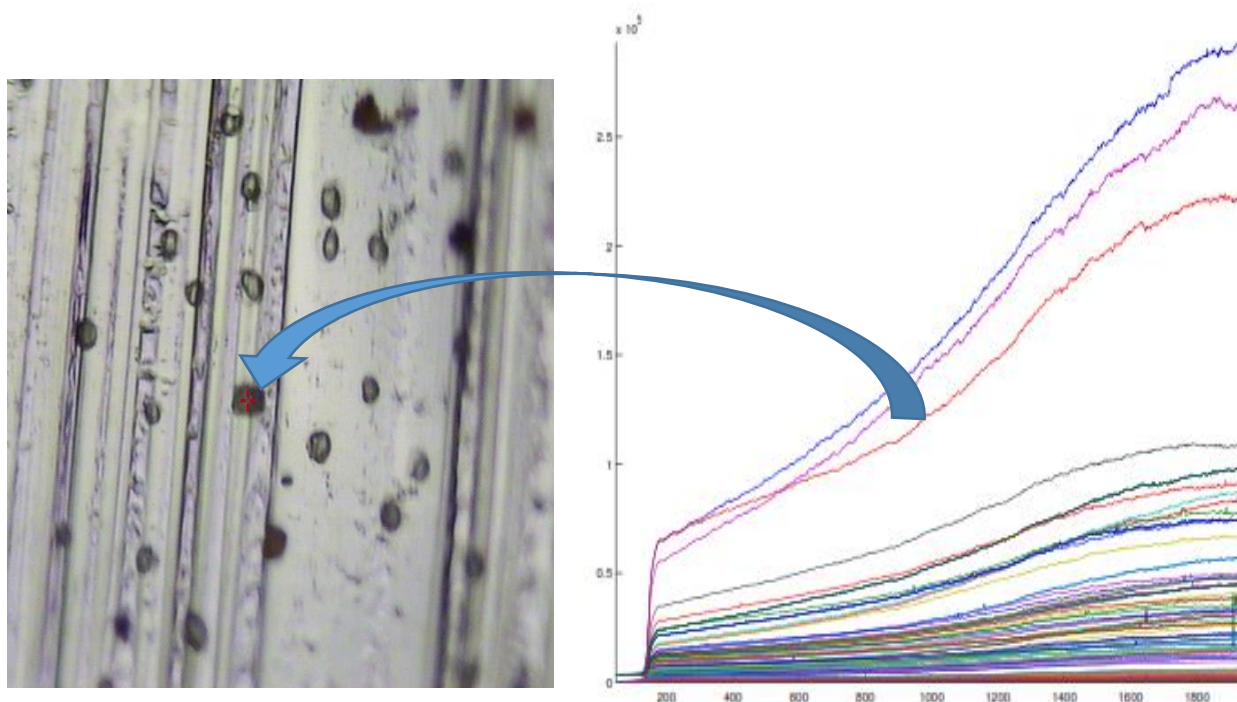
Figure 5.31: Analyzed region (Left) and the resolved D-matrix (Right).

5.14.1 Resolved Spectra (S) and Concentration Profiles of Aerosol Particles

No pre-processing technique was employed on the data since when they were used, there was no good correlation achieved between the resolved component spectra and the reference spectra. The number of components required to describe the data set was set at four components based on prior knowledge of data required to describe the data set. The four components denoted uranium embedded to either an oxide or to the three anions as it were during simulate preparation (sulphate based, chloride based or nitrate based). The resolved spectra and concentration profiles is as in Figure 5.32 and Figure 5.33 respectively. The lack of fit was 9.56 % while the explained variance was 80.883 %. The two factors were considered satisfactory for characterizing the aerosol particles. The resolved peaks in the spectral profile from component 1 to component 4 show that the aerosol particles is a heterogeneous mixture of many uranium scatter bands as a result of different uranium compounds though dominated by uranyl chloride owing to the identified visible peaks. The spatial distribution of uranium in the particles is shown in the total intensity map and the individual resolved component maps.

5.14.2 Resolved Spectral Profiles

Even though the raw spectra for the aerosol particle had no peaks obtained using Raman, MCR-ALS has the potential to resolve the most informative Raman scatter bands associated with the uranium molecule. Figure 5.32 show the resolved spectra of both uranium embedded to other anions and free anions as well as resolved spectra when the uranium compound is either attached to an oxide or to other anions. The resolved peaks have been identified based on the ones used during model development.
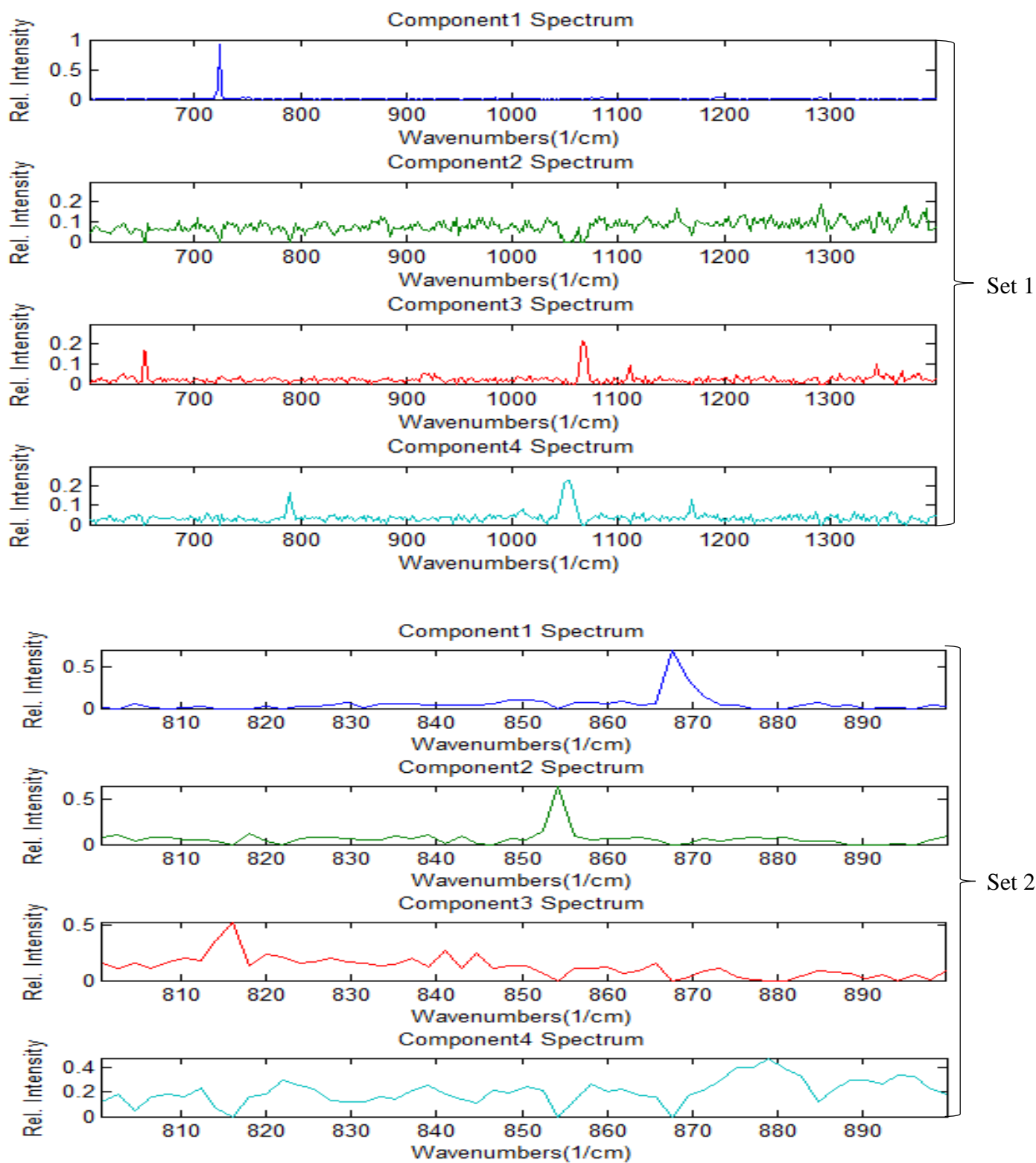
Figure 5.32: Resolved spectral profiles for different Raman scatter bands specific to uranium.

From Figure 5.32, MCR-ALS was able to resolve the spectra of the heterogeneous aerosol particle by giving the structural distribution information of uranium and the embedded/free anions. However, the resolved spectra specific for most uranium scatter bands (800-870cm^{-1}) has very small Raman scatter bands most of which are buried in the background. This could be attributed to the fact that the spatial resolution optimal for the Raman imaging is 1µm and hence mapping a 4.5 µm will imply that small number of photons will be focused on the particle generating a low signal to noise ratio (Piliarik and Sandoghdar, 2014). Furthermore, due to the photon wavelength, the diffraction limit prevents observing the details about the sub-micron sized particles (Offroy *et al.*, 2015) especially for the low concentration levels hence low intensity signal for the uranium specific bands. However, based on set 2 (specific for uranium fingerprint region), the following Raman scatter bands were well resolved using the MCR-ALS; 868 cm^{-1} (specific for uranyl nitrate), 854 cm^{-1} and 814 cm^{-1} (assigned to uranyl chloride). This can be concluded as the typical nuclear forensic signatures that can be used in a forensic investigation of environmental samples.

5.14.3 Resolved Concentration Profile

The resolved concentration profile will bring out the spatial distribution of uranium based on the individual components. The two sets in Figure 5.32 show the distribution of uranium in the aerosol particle for uranium specific bands (set 2) as well as having anions (set 1).
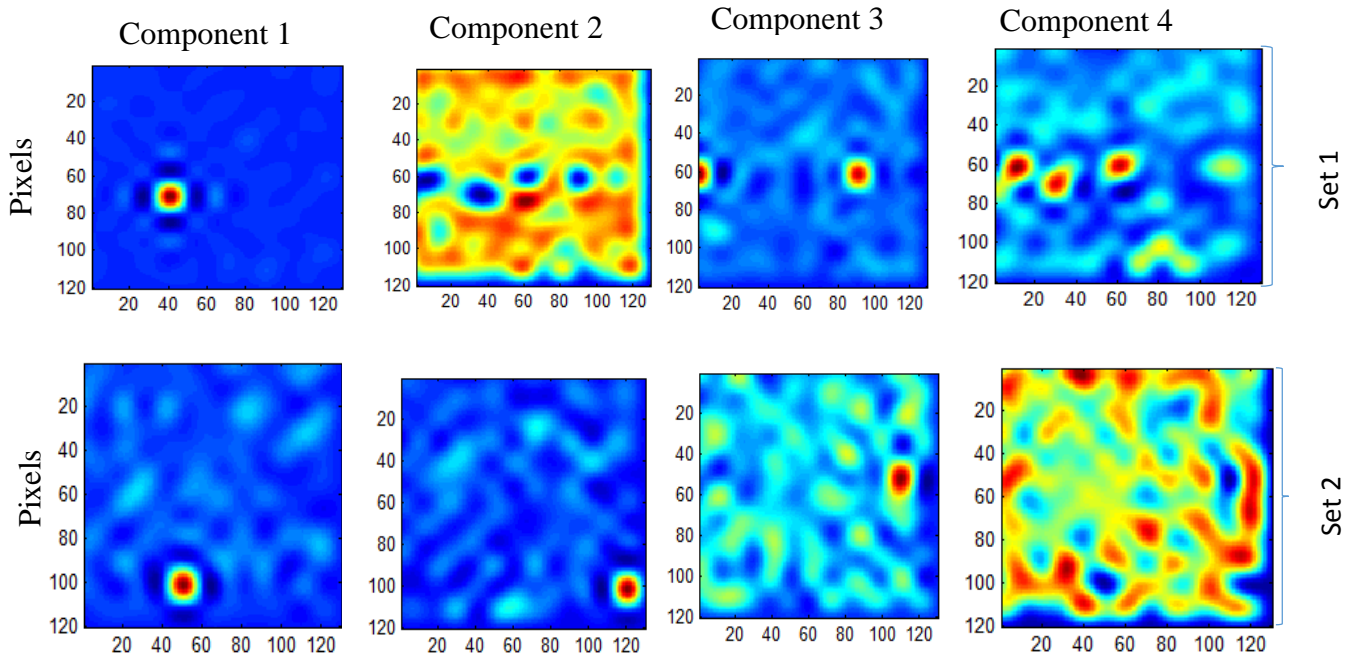
Figure 5.33: Resolved components showing spatial distribution of uranium in aerosol particle.

Color code:

Intense red color- High uranium concentration

Yellowish color- Uranium fading away

Blue- matrix background

From the resolved components, the region having a big range of spectrum (including anions) show a higher uranium distribution only in component 2. However, with a focus in the specific uranium

Raman scatter bands as in set 2, the uranium becomes intense (as shown in component 4, set 2). A higher uranium distribution is also shown in component 3 even though the intensity is not so much.

ALS resolved concentration images: set 1 is for the resolved spectral profiles (600-1400 cm^{-1}) while set 2 is for the resolved spectral profiles based on the nuclear forensic signatures specific for uranium in aerosol particles. The corresponding assignment of the uranium bonds associated with the spatial distribution of the ALS resolved images in set 2 can be assigned as 868 cm^{-1} (uranyl nitrate), 853 cm^{-1} (uranyl chloride), 814 cm^{-1} uranyl chloride. From the analysis, uranyl chloride dominates in almost all the components in both the resolved spectral profiles and the corresponding spatial distribution maps. Owing to the many Raman scatter bands associated with uranyl chloride, we can conclude that most of the PM$_{2.5}$ aerosol particles were chloride based uranium particles. The source of these materials could be the condensation of the particles from sea salt. This results show that spatial distribution of uranium in a particle (size-resolved) can be used as a NF signature in nuclear security and safeguards.

6 CONCLUSIONS

This work has shown that it is possible to quantify uranium in coarse and fine particulate matter based on drop- coated uranium bearing aerosol simulate samples and artificial neural network. The work has also shown that confocal Raman microspectroscopy is an important analytical tool in obtaining spectra from samples with limited sizes. Unlike other techniques, Raman spectroscopy has proved to be non-destructive and needs no tedious sample preparation procedures. Based on the two laser excitation wavelengths, different uranium compounds were well characterized and assigned as would be expected in any nuclear forensic analysis.

From this work, we also conclude that unlike cascade correlation, newfeed forward artificial neural network architecture is reliable as it provides predictions with better accuracy. Furthermore, the BP-ANN takes shorter time to learn and hence can still be used for bigger dimensional data.

The results on quantification of uranium in particulate matter indicated that $PM_{4.5}$ had more uranium concentrations as compared to $PM_{2.5.}$ This was attributed to way the particles were immobilized. Whereas $PM_{4.5}$ were as a result of dust lift, the $PM_{2.5}$ were immobilized from majorly the sea spray salt. The PCA carried out on the particulate matter indicated that the two particle sizes can be delineated based on specific uranium scatter bands. Unlike the $PM_{2.5}$, $PM_{4.5}$ had a lot of influence from the road sides. On the other hand, all the $PM_{2.5}$ clustered together and were heavily influenced by Raman scatter bands associated with uranyl chloride. This demonstrated the importance of PCA in source apportionment of uranium in aerosol particles of different sizes. The role of PCA was very important as it can be used to trace particular aerosols to a particular nuclear facility based on its uranium signature.

The sampled aerosols also showed large heterogeneity of the individual particles which was resolved based on multivariate curve resolution. The multivariate curve resolution helped in yielding information about the pure uranium species present (spectral resolution) and where they are located (spatial resolution) within the $PM_{4.5}$ aerosol particle after point spectroscopy. Based on MCR-ALS, the Raman scatter bands associated with uranium were resolved as 814 cm^{-1}, 854 cm^{-1} and 868 cm^{-1}. On the other hand, Raman scatter bands associated with anions were resolved as well. The results obtained for MCR-ALS were consistent with those obtained for the PCA. This shows that a combination of the two chemometric techniques can be used to attempt source attribution of environmentally sampled particulate matter for nuclear forensic applications.

The spectral features identified in this work would provide useful information in a national nuclear forensics library (NNFL) in cases when visual information concerning the source, e.g. a source serial number, for various reasons might be limited or not available. This thesis has demonstrated that the precursor of development of such a library is the ability to identify such radioactive materials in their small quantities.

We also conclude that unlike other techniques that are destructive and requiring sizeable samples (besides the tedious sample preparation procedures), Raman microspectroscopy is more reliable since it can do direct, rapid analysis of micro-size particles such as aerosols which is a powerful tool in monitoring undeclared nuclear activities. Confocal Raman microspectrometry which combines the molecular analysis capabilities of Raman scattering and the spatial resolution of optical microscopy is well adapted for obtaining direct molecular information on individual micron size aerosol particles under ambient condition.

The results have also demonstrated that anionic impurities and other minor constituents of suspected radioactive materials can be used as unique forensic signatures that can be used to answer two important forensic question: What is the materials? Where did it come from?

6.1 RECOMMENDATIONS for FUTURE WORK

A more robust and effective monodisperse aerosol generator is recommended for future simulation of aerosol particles. Methods used to generate such monodisperse aerosol particles may include use of vibrating orifice aerosol generator, use of electrospray technique or spin coating. This will ensure that different models are developed for different particle sizes which will ensure more reliable quantification of uranium in particulate matter. Such models will be more reliable in conducting size resolved quantification of uranium in aerosol particles. More so, since this study was initially meant to be carried out on Mrima hill apex and its immediate surroundings, and considering that uranium concentration in $PM_{4.5}$ was as a result of the immediate environment such as dust lift, it is recommended that future studies involve a comparative study of levels of uranium on the three hills i.e. Mrima, Kiruku and Jumbo to provide insights of which area has more levels. Nevertheless, the information obtained in this study can be used as a base line upon which uranium concentrations can be characterized.

This study also recommends sampling for a longer time so that more load can be obtained on the substrate from which comparative uranium concentrations can be obtained based on a different technique such as XRF or EDXRF. Future studies can also involve *in-situ* measurements of uranium levels in aerosol particles by use of *in-situ* techniques.

Since the methodology has proved to be reliable in detecting trace radioactive materials in their embedded matrix, we recommend that the developed algorithms could in future be incorporated in hand held Raman equipment for early in-field detection of nuclear and radioactive materials.

REFERENCES

Achola, S. O., Patel, J. P., Mustapha, A. O., and Angeyo, H. K. (2012). Natural radioactivity and external dose in the high background radiation area of Lambwe East, Southwestern Kenya. *Radiat. Prot. Dosimetry* **152**, 423–428.

Aksenenko, V. M., Murav'ev, N. S., and Taranenko, G. S. (1986). Raman-scattering study of nitric-acid solutions. *J. Appl. Spectrosc.* **44**, 70–72.

Baranwal, V. C., Sharma, S. P., Sengupta, D., Sandilya, M. K., Bhaumik, B. K., Guin, R., and Saha, S. K. (2006). A new high background radiation area in the Geothermal region of Eastern Ghats Mobile Belt (EGMB) of Orissa, India. *Radiat. Meas.* **41**, 602–610.

Batonneau, Y., Sobanska, S., Laureyns, J., and Bremard, C. (2006). Confocal Microprobe Raman Imaging of Urban Tropospheric Aerosol Particles. *Environ. Sci. Technol.* **40**, 1300–1306.

Bellis, D., Ma, R., Bramall, N., and McLeod, C. W. (2001). Airborne emission of enriched uranium at Tokai-mura, Japan. *Sci. Total Environ.* **264**, 283–286.

Bem, H. and Bou-Rabee, F. (2004). Environmental and health consequences of depleted uranium use in the 1991 Gulf War. *Environ. Int.* **30**, 123–134.

Betti, M., Tamborini, G., and Koch, L. (1999). Use of Secondary Ion Mass Spectrometry in Nuclear Forensic Analysis for the Characterization of Plutonium and Highly Enriched Uranium Particles. *Anal. Chem.* **71**, 2616–2622.

Bhandari, D. (2011). Surface-Enhanced Raman Scattering: Substrate Development and Applications in Analytical Detection. *Dr. Diss.*

Bhatt, B., Angeyo.H.K, and Alix, D. (2017). Rapid Nuclear Forensics Analysis via Laser Based Microphotonic Techniques Coupled with Chemometrics. *Int. Youth Nucl. Congr. 2016* **127**, 76–86.

Bleise, A., Danesi, P. R., and Burkart, W. (2003). Properties, use and health effects of depleted uranium (DU): a general overview. *J. Environ. Radioact.* **64**, 93–112.

Brereton, R. G. (2003). "Chemometrics: Data Analysis for the Laboratory and Chemical Plant." John Wiley & Sons.

Bullock, J. I. and Parrett, F. W. (1970). The low frequency infrared and Raman spectroscopic studies of some uranyl complexes: the deformation frequency of the uranyl ion. *Can. J. Chem.* **48**, 3095–3097.

Bumbrah, G. S. and Sharma, R. M. (2016). Raman spectroscopy – Basic principle, instrumentation and selected applications for the characterization of drugs of abuse. *Egypt. J. Forensic Sci.* **6**, 209–215.

Burneau, A. and Teiten, B. (1999). Surface-enhanced raman spectra of both uranyl(VI) and 2-(5-bromo-2-pyridylazo)-5-diethylaminophenol in silver colloids. *Vib. Spectrosc.* **21**, 97–109.

Carranza, J. E., Iida, K., and Hahn, D. W. (2003). Conditional data processing for single-shot spectral analysis by use of laser-induced breakdown spectroscopy. *Appl. Opt.* **42**, 6022–6028.

Chege, M. W., Hashim, N. O., and Merenga, A. S. (2013). Physico-Chemical Analysis of Groundwater in the Gazi-Mrima Hill Region of Kwale County, Kenya.

CHEN, S. and BILLINGS, S. A. (1992). Neural networks for nonlinear dynamic system modelling and identification. *Int. J. Control* **56**, 319–346.

Clark, R. J. H. and Dines, T. J. (1986). Resonance Raman Spectroscopy, and Its Application to Inorganic Chemistry. New Analytical Methods (27). *Angew. Chem. Int. Ed. Engl.* **25**, 131–158.

Clerbaux, C., Boynard, A., and Clarisse, L. (2009). Monitoring of atmospheric composition using the thermal infrared IASI/MetOp sounder. *Atmospheric Chemostry Phys.* **9**.

Cooper, J. B., Wise, K. L., Welch, W. T., Sumner, M. B., Wilt, B. K., and Bledsoe, R. R. (1997). Comparison of Near-IR, Raman, and Mid-IR Spectroscopies for the Determination of BTEX in Petroleum Fuels. *Appl. Spectrosc.* **51**, 1613–1620.

Csele, M. (2004). Visible Gas Lasers. *In* "Fundamentals of Light Sources and Lasers," pp235–260. John Wiley & Sons, Inc.

Davies, J. P., Hallowell, S. F., and Hoglund, D. E. (1994). Particle generators for the calibration and testing of narcotic and explosive vapor/particle detection systems. Vol. 2092, pp137–144.

Demtröder, P. D. W. (2010). Modern Developments in Atomic and Molecular Physics. *In* "Atoms, Molecules and Photons," pp487–518. Springer Berlin Heidelberg.

Demtröder, W. (2015). "Laser Spectroscopy 2: Experimental Techniques." Springer.

Demuth, H. and Beale, M. (2009). "Matlab neural network toolbox user's guide version 6. The MathWorks Inc."

Despagne, F. and Massart, D. L. (1998). Neural networks in multivariate calibration. *Analyst* **123**, 157R–178R.

Dieing, T., Hollricher, O., and Toporski, J. (2011). "Confocal Raman Microscopy." Springer Science & Business Media.

Dingari, N. C., Horowitz, G. L., Kang, J. W., Dasari, R. R., and Barman, I. (2012). Raman Spectroscopy Provides a Powerful Diagnostic Tool for Accurate Determination of Albumin Glycation. *PLOS ONE* **7**, e32406.

Driscoll, R. J. P., Wolverson, D., Mitchels, J. M., Skelton, J. M., Parker, S. C., Molinari, M., Khan, I., Geeson, D., and Allen, G. C. (2014). A Raman spectroscopic study of uranyl minerals from Cornwall, UK. *RSC Adv.* **4**, 59137–59149.

Drooge, B. L. van and Grimalt, J. O. (2015). Particle size-resolved source apportionment of primary and secondary organic tracer compounds at urban and rural locations in Spain. *Atmos Chem Phys* **15**, 7735–7752.

Efremov, E. V., Ariese, F., and Gooijer, C. (2008). Achievements in resonance Raman spectroscopy: Review of a technique with a distinct analytical chemistry potential. *Anal. Chim. Acta* **606**, 119–134.

Eriksson, M., Osán, J., Jernström, J., Wegrzynek, D., Simon, R., Chinea-Cano, E., Markowicz, A., Bamford, S., Tamborini, G., Török, S., Falkenberg, G., Alsecz, A., Dahlgaard, H., Wobrauschek, P., Streli, C., Zoeger, N., and Betti, M. (2005). Source term identification of environmental radioactive Pu/U particles by their characterization with non-destructive spectrochemical analytical techniques. *Spectrochim. Acta Part B At. Spectrosc.* **60**, 455–469.

Fahlman, S. E. and Lebiere, C. (1990). The cascade-correlation learning architecture.

Fauré, A.-L., Rodriguez, C., Marie, O., Aupiais, J., and Pointurier, F. (2014). Detection of traces of fluorine in micrometer sized uranium bearing particles using SIMS. *J. Anal. At. Spectrom.* **29**, 145–151.

Fedchenko, V. (2014). The Role of Nuclear Forensics in Nuclear Security. *Strateg. Anal.* **38**, 230–247.

Fiedor, J. N., Bostick, W. D., Jarabek, R. J., and Farrell, J. (1998). Understanding the Mechanism of Uranium Removal from Groundwater by Zero-Valent Iron Using X-ray Photoelectron Spectroscopy. *Environ. Sci. Technol.* **32**, 1466–1473.

Fittschen, U. E. A., Hauschild, S., Amberger, M. A., Lammel, G., Streli, C., Förster, S., Wobrauschek, P., Jokubonis, C., Pepponi, G., Falkenberg, G., and Broekaert, J. A. C. (2006). A new technique for the deposition of standard solutions in total reflection X-ray fluorescence spectrometry (TXRF) using pico-droplets generated by inkjet printers and its applicability for aerosol analysis with SR-TXRF. *Spectrochim. Acta Part B At. Spectrosc.* **61**, 1098–1104.

Furness, R. (1990). "Heavy Metals in the Marine Environment." CRC Press., Boca Raton.

Hettinger, C., Christensen, T., Ehlert, B., Humpherys, J., Jarvis, T., and Wade, S. (2017). Forward Thinking: Building and Training Neural Networks One Layer at a Time. *ArXiv170602480 Cs Stat*.

Howley, T., Madden, M. G., O'Connell, M.-L., and Ryder, A. G. (2006). The effect of principal component analysis on machine learning accuracy with high-dimensional spectral data. *Knowl.-Based Syst.* **19**, 363–370.

Ilonen, J., Kamarainen, J.-K., and Lampinen, J. (2003). Differential Evolution Training Algorithm for Feed-Forward Neural Networks. *Neural Process. Lett.* **17**, 93–105.

Jaumot, J., Juan, A. de, and Tauler, R. (2015). MCR-ALS GUI 2.0: New features and applications. *Chemom. Intell. Lab. Syst.* **140**, 1–12.

Jeambrun, M., Pourcelot, L., Mercat, C., Boulet, B., Loyen, J., Cagnat, X., and Gauthier-Lafaye, F. (2012). Study on transfers of uranium, thorium and decay products from grain, water and soil to chicken meat and egg contents. *J. Environ. Monit.* **14**, 2170.

Jiang, J., Ma, L., Chen, J., Zhang, P., Wu, H., Zhang, Z., Wang, S., Yun, W., Li, Y., Jia, J., and Liao, J. (2017). SERS detection and characterization of uranyl ion sorption on silver nanorods wrapped with Al2O3 layers. *Microchim. Acta*, 1–8.

Keegan, E., Kristo, M. J., Colella, M., Robel, M., Williams, R., Lindvall, R., Eppich, G., Roberts, S., Borg, L., Gaffney, A., Plaue, J., Wong, H., Davis, J., Loi, E., Reinhard, M., and Hutcheon, I. (2014). Nuclear forensic analysis of an unknown uranium ore concentrate sample seized in a criminal investigation in Australia. *Forensic Sci. Int.* **240**, 111–121.

Kemp, R. S. (2008). Initial Analysis of the Detectability of UO2F2 Aerosols Produced by UF6 Released from Uranium Conversion Plants. *Sci. Glob. Secur.* **16**, 115–125.

Kneipp, K., Kneipp, H., Itzkan, I., Dasari, R. R., and Feld, M. S. (1999). Ultrasensitive Chemical Analysis by Raman Spectroscopy. *Chem. Rev.* **99**, 2957–2976.

Knott, A., Chinea-Cano, E., Wegrzynek, D., Dürr, M., and Vogt, S. (2014). "Production and Characterization of Monodisperse Reference Particles," Rep. No. FZJ-2014-06472. Nukleare Entsorgung und Reaktorsicherheit.

Krajkó, J., Varga, Z., Wallenius, M., Mayer, K., and Konings, R. (2016). Investigation of sulphur isotope variation due to different processes applied during uranium ore concentrate production. *J. Radioanal. Nucl. Chem.* **309**, 1113–1121.

Lau, K. H., Brittain, R. D., and Hildenbrand, D. L. (1985). Complex sublimation/decomposition of uranyl fluoride: thermodynamics of gaseous uranyl fluoride (UO2F2) and uranium oxide fluoride (UOF4). *J. Phys. Chem.* **89**, 4369–4373.

Lavine, B. and Workman, J. (2008). Chemometrics. *Anal. Chem.* **80**, 4519–4531.

Lemma, F. G. Di, Colle, J. Y., Rasmussen, G., and Konings, R. J. M. (2015). Fission product partitioning in aerosol release from simulated spent nuclear fuel. *J. Nucl. Mater.* **465**, 127–134.

Liu, Y., Upadhyaya, B. R., and Naghedolfeizi, M. (1993). Chemometric Data Analysis Using Artificial Neural Networks. *Appl. Spectrosc.* **47**, 12–23.

Loosmore, G. A. and Cederwall, R. T. (2004). Precipitation scavenging of atmospheric aerosols for emergency response applications: testing an updated model with new real-time data. *Atmos. Environ.* **38**, 993–1003.

Lu, G., Forbes, T. Z., and Haes, A. J. (2016). Evaluating Best Practices in Raman Spectral Analysis for Uranium Speciation and Relative Abundance in Aqueous Solutions. *Anal. Chem.* **88**, 773–780.

Luna, A. S., Lima, I. C. A., Rocha, W. F. C., Araújo, J. R., Kuznetsov, A., Ferreira, E. H. M., Boqué, R., and Ferré, J. (2014). Classification of soil samples based on Raman spectroscopy and X-ray fluorescence spectrometry combined with chemometric methods and variable selection. *Anal. Methods* **6**, 8930–8939.

Mahur, A. K., Kumar, R., Mishra, M., Sengupta, D., and Prasad, R. (2008). An investigation of radon exhalation rate and estimation of radiation doses in coal and fly ash samples. *Appl. Radiat. Isot.* **66**, 401–406.

Mandal, A. and Sengupta, D. (2003). Radioelemental study of Kolaghat, thermal power plant, West Bengal, India: possible environmental hazards. *Environ. Geol.* **44**, 180–186.

Mangala, M. J. (1987). Multi-elemental energy dispersive x-ray fluorescence analysis of Kerio valley fluorite ores and Mrima hill soil sediments. Thesis, University of Nairobi.

Martin, T. C., Mathur, S. C., and Morgan, I. L. (1964). The application of nuclear techniques in coal analysis. *Int. J. Appl. Radiat. Isot.* **15**, 331–338.

Maxime, D. and Laurent, B. (2013). Experimental study of uranyl(VI) chloride complex formation in acidic LiCl aqueous solutions under hydrothermal conditions (T = 21 °C–350 °C, Psat) using Raman spectroscopy. *Eur. J. Minerol.* **25**, 765–775.

Mayer, K., Wallenius, M., and Varga, Z. (2013). Nuclear Forensic Science: Correlating Measurable Material Parameters to the History of Nuclear Material. *Chem. Rev.* **113**, 884–900.

Mikoliunaite, L., Rodriguez, R. D., Sheremet, E., Kolchuzhin, V., Mehner, J., Ramanavicius, A., and Zahn, D. R. T. (2015). The substrate matters in the Raman spectroscopy analysis of cells. *Sci. Rep.* **5**, 1–10.

Moody, K. J., Grant, P. M., and Hutcheon, I. D. (2014). "Nuclear Forensic Analysis, Second Edition." CRC Press.

Nguyen Trung, C., Begun, G. M., and Palmer, D. A. (1992). Aqueous uranium complexes. 2. Raman spectroscopic study of the complex formation of the dioxouranium(VI) ion with a variety of inorganic and organic ligands. *Inorg. Chem.* **31**, 5280–5287.

Nriagu, J., Nam, D.-H., Ayanwola, T. A., Dinh, H., Erdenechimeg, E., Ochir, C., and Bolormaa, T.-A. (2012). High levels of uranium in groundwater of Ulaanbaatar, Mongolia. *Sci. Total Environ.* **414**, 722–726.

O'Brien, R. S. and Cooper, M. B. (1998). Technologically enhanced naturally occurring radioactive material (NORM): Pathway analysis and radiological impact. *Appl. Radiat. Isot.* **49**, 227–239.

Oeh, U., Priest, N. D., Roth, P., Ragnarsdottir, K. V., Li, W. B., Höllriegl, V., Thirlwall, M. F., Michalke, B., Giussani, A., Schramel, P., and Paretzke, H. G. (2007). Measurements of daily urinary uranium excretion in German peacekeeping personnel and residents of the Kosovo region to assess potential intakes of depleted uranium (DU). *Sci. Total Environ.* **381**, 77–87.

Offroy, M., Moreau, M., Sobanska, S., Milanfar, P., and Duponchel, L. (2015). Pushing back the limits of Raman imaging by coupling super-resolution and chemometrics for aerosols characterization. *Sci. Rep.* **5**, 1–14.

Otwoma, D., Patel, J. P., Bartilol, S., and Mustapha, A. O. (2000). Radioactivity and Trace Elements in Rock/Soil Samples and Dose Assessment of the Public Residing near Homa Mountain, Homa Bay County, Kenya.

Palacios, M. L. and Taylor, S. H. (2000). Characterization of Uranium Oxides Using *in Situ* Micro-Raman Spectroscopy. *Appl. Spectrosc.* **54**, 1372–1378.

Piliarik, M. and Sandoghdar, V. (2014). Direct optical sensing of single unlabelled proteins and super-resolution imaging of their binding sites. *Nat. Commun.* **5**, 1–8.

Pointurier, F. and Marie, O. (2010a). Identification of the chemical forms of uranium compounds in micrometer-size particles by means of micro-Raman spectrometry and scanning electron microscope. *Spectrochim. Acta Part B At. Spectrosc.* **65**, 797–804.

Pointurier, F. and Marie, O. (2010b). Identification of the chemical forms of uranium compounds in micrometer-size particles by means of micro-Raman spectrometry and scanning electron microscope. *Spectrochim. Acta Part B At. Spectrosc.* **65**, 797–804.

Ramli, A. T., Hussein, A. W. M. A., and Wood, A. K. (2005). Environmental 238U and 232Th concentration measurements in an area of high level natural background radiation at Palong, Johor, Malaysia. *J. Environ. Radioact.* **80**, 287–304.

Ranebo, Y., Eriksson, M., Tamborini, G., Niagolova, N., Bildstein, O., and Betti, M. (2007). The Use of SIMS and SEM for the Characterization of Individual Particles with a Matrix Originating from a Nuclear Weapon. *Microsc. Microanal.* **13**, 179–190.

Ranebo, Y., Niagolova, N., Erdmann, N., Eriksson, M., Tamborini, G., and Betti, M. (2010). Production and Characterization of Monodisperse Plutonium, Uranium, and Mixed Uranium−Plutonium Particles for Nuclear Safeguard Applications. *Anal. Chem.* **82**, 4055–4062.

Ru, E. C. Le and Etchegoin, P. G. (2009). Principles of Surface-Enhanced Raman Spectroscopy and related plasmonic effects. *Elsevier Ltd*, 1–656.

Ruan, C., Luo, W., Wang, W., and Gu, B. (2007). Surface-enhanced Raman spectroscopy for uranium detection and analysis in environmental samples. *Anal. Chim. Acta* **605**, 80–86.

Sandalls, F. J., Segal, M. G., and Victorova, N. (1993). Hot particles from Chernobyl: A review. *J. Environ. Radioact.* **18**, 5–22.

Sato-Berrú, R. Y., Medina-Valtierra, J., Medina-Gutiérrez, C., and Frausto-Reyes, C. (2004). Quantitative NIR–Raman analysis of methyl-parathion pesticide microdroplets on aluminum substrates. *Spectrochim. Acta. A. Mol. Biomol. Spectrosc.* **60**, 2231–2234.

Shah, R. B., Tawakkul, M. A., and Khan, M. A. (2007). Process analytical technology: Chemometric analysis of Raman and near infra-red spectroscopic data for predicting physical properties of extended release matrix tablets. *J. Pharm. Sci.* **96**, 1356–1365.

Shawky, S., Amer, H., Nada, A. A., Abd El-Maksoud, T. M., and Ibrahiem, N. M. (2001). Characteristics of NORM in the oil industry from Eastern and Western deserts of Egypt. *Appl. Radiat. Isot.* **55**, 135–139.

Smith, E. and Dent, G. (2013). "Modern Raman Spectroscopy: A Practical Approach." John Wiley & Sons.

Smith, E. and Dent, G. (2004). Introduction, Basic Theory and Principles. *In* "Modern Raman Spectroscopy – A Practical Approach," pp1–21. John Wiley & Sons, Ltd.

Sobanska, S., Falgayrac, G., Laureyns, J., and Brémard, C. (2006). Chemistry at level of individual aerosol particle using multivariate curve resolution of confocal Raman image. *Spectrochim. Acta. A. Mol. Biomol. Spectrosc.* **64**, 1102–1109.

Sparks, D. L. (2003). "Environmental Soil Chemistry." Academic Press.

Stanimirova, I., Tauler, R., and Walczak, B. (2011). A Comparison of Positive Matrix Factorization and the Weighted Multivariate Curve Resolution Method. Application to Environmental Data. *Environ. Sci. Technol.* **45**, 10102–10110.

Stefaniak, E. A., Alsecz, A., Frost, R., Máthé, Z., Sajó, I. E., Török, S., Worobiec, A., and Van Grieken, R. (2009). Combined SEM/EDX and micro-Raman spectroscopy analysis of uranium minerals from a former uranium mine. *J. Hazard. Mater.* **168**, 416–423.

Stefaniak, E. A., Alsecz, A., Sajó, I. E., Worobiec, A., Máthé, Z., Török, S., and Grieken, R. Van (2008). Recognition of uranium oxides in soil particulate matter by means of μ-Raman spectrometry. *J. Nucl. Mater.* **381**, 278–283.

Stefaniak, E. A., Pointurier, F., Marie, O., Truyens, J., and Aregbe, Y. (2013). In-SEM Raman microspectroscopy coupled with EDX – a case study of uranium reference particles. *Analyst* **139**, 668–675.

Steinfield, J. (1998). EXPLOSIVES DETECTION: A Challenge for Physical Chemistry. *Annu. Rev. Phys. Chem.* **49**, 203–232.

Stiles, P. L., Dieringer, J. A., Shah, N. C., and Duyne, R. P. V. (2008). Surface-Enhanced Raman Spectroscopy. *Annu. Rev. Anal. Chem.* **1**, 601–626.

Stöckle, R. M., Suh, Y. D., Deckert, V., and Zenobi, R. (2000). Nanoscale chemical analysis by tip-enhanced Raman spectroscopy. *Chem. Phys. Lett.* **318**, 131–136.

Udey, R. N., Jones, A. D., and Farquar, G. R. (2013). Aerosol and Microparticle Generation Using a Commercial Inkjet Printer. *Aerosol Sci. Technol.* **47**, 361–372.

Varga, Z., Krajkó, J., Peńkin, M., Novák, M., Eke, Z., Wallenius, M., and Mayer, K. (2017). Identification of uranium signatures relevant for nuclear safeguards and forensics. *J. Radioanal. Nucl. Chem.* **312**, 639–654.

Varmuza, K. and Filzmoser, P. (2016). "Introduction to Multivariate Statistical Analysis in Chemometrics." CRC Press.

Veiga, R., Sanches, N., Anjos, R. M., Macario, K., Bastos, J., Iguatemy, M., Aguiar, J. G., Santos, A. M. A., Mosquera, B., Carvalho, C., Baptista Filho, M., and Umisedo, N. K. (2006). Measurement of natural radioactivity in Brazilian beach sands. *Radiat. Meas.* **41**, 189–196.

Wakui, T., Jin, W.-G., Hasegawa, K., Uematsu, H., Minowa, T., and Katsuragawa, H. (2003). High-Resolution Diode-Laser Spectroscopy of the Rare-Earth Elements. *J. Phys. Soc. Jpn.* **72**, 2219–2223.

White, S. N. (2009). Laser Raman spectroscopy as a technique for identification of seafloor hydrothermal and cold seep minerals. *Chem. Geol.* **259**, 240–252.

Worobiec, A., Potgieter-Vermaak, S. S., Berghmans, P., Winkler, H., Burger, R., and Grieken, R. V. (2011). Air Particulate Emissions in Developing Countries: A Case Study in South Africa. *Anal. Lett.* **44**, 1907–1924.

Zachhuber, B., Gasser, C., Chrysostom, E. t.H., and Lendl, B. (2011). Stand-Off Spatial Offset Raman Spectroscopy for the Detection of Concealed Content in Distant Objects. *Anal. Chem.* **83**, 9438–9442.

Zakaria, N., Baan, R., and Kathiravale, S. Radiological impact from airborne routine discharges of Coal-Fired power plant.

Zhang, D., Xie, Y., Mrozek, M. F., Ortiz, C., Davisson, V. J., and Ben-Amotz, D. (2003). Raman Detection of Proteomic Analytes. *Anal. Chem.* **75**, 5703–5709.

Zielinski, R. A. and Budahn, J. R. (1998). Radionuclides in fly ash and bottom ash: improved characterization based on radiography and low energy gamma-ray spectrometry. *Fuel* **77**, 259–267.

APPENDICES
Appendix 1 Neural Network Algorithm

Load the data

% normalize inputs and targets

```
[In, Is] = mapstd (I);

[Tn, Ts] = mapstd (T);

Sn=mapstd(S);
```

% create a feedforward network with the hidden number of neurons and assign the Levenberg-

Marquardt training function –Logsig. The NEWFF command was used to initialize the weights.

```
net = newff (In, Tn, 3, {'logsig'});
```

% train the network with different parameters

```
net.divideparam.trainratio=0.6;

net.divideparam.testratio=0.25;

net.divideparam.valratio=0.25;

net.trainParam.epochs = 50;

net.trainParam.lr = 0.000001;

net.trainParam.show = 20;

net.trainParam.goal = 0.00001;

% simulate the trained network.

net = train (net, In, Tn);

R = sim (net, Sn);
```

% convert the outputted results of the network into the original units of the targets. This is

because by using mapstd function, the values were normalized. We therefore need to revert them

to their original format.

```
End
```

Appendix 2 PCA Algorithm in R

```r
library (Chemo Spec)

library (devtools)

library(utils)

library(knitr)

library(R.utils)

files2SpectraObject(gr.crit = c("A", "X","U","W","V"), gr.cols = c("red3", "dodgerblue4",
"gray0","yellow","orangered"),

            freq.unit = "Raman shift (/cm)", int.unit = "peak intensity (a.u)", descrip = "Small",

            out.file = "pcasmall", sep=",")

#a new file called pcasim.RData is created which can be accessed as follows

SPCA <- loadObject("pcasmall.RData")

#make the data available

data(SPCA)

sumSpectra(SPCA)

# Will make a fancy title here and re-use in other plots

myt <- expression(bolditalic(PM2.5)~bolditalic(aerosol)~bold(Sample~Spectra))

plotSpectra(SPCA, main = myt,

      which = c(1, 2, 7, 10, 11, 12),

      yrange = c(0, 60000), offset = 100, lab.pos = 320)

#zoom into specific region of the spectra

plotSpectra(SPCA, main = myt,

      which = c(1, 2, 3,4,5,6,7,8,9,10,11,12), xlim = c(600, 1200),
```

```
        yrange = c(0, 60000), offset = 100, lab.pos = 382)

#normalize spectra data

#NTPCA <- normSpectra(TPCA)

sumSpectra(SPCA)

#zoom into specific region of the spectra

plotSpectra(SPCA, main = myt,

        which = c(1, 2, 3,4,5,6, 7,8,9,10,11,12), xlim = c(600, 1200),

        yrange = c(0, 60000), offset = 0.1, lab.pos = 382)

plotSpectra(SPCA, main = myt,

        which = c(1, 2, 3, 7), xlim = c(400, 1200),

        yrange = c(0, 60000), offset = 100, lab.pos = 382)

SPCA

library(baseline)

#baseline restoration

BSPCA <- baselineSpectra(SPCA, int = FALSE, method = "rfbaseline", retC = TRUE)

# To remove a sample from the spectra say

#noL0 <- removeSample(TPCA, rem.sam = c("L0"))

#NormPCA <- normSpectra(noL0)

plotSpectra(BSPCA, main = myt,

        which = c(1, 2, 3, 7), xlim = c(600, 1200),

        yrange = c(0, 6000), offset = 100, lab.pos = 382)

#principal component analysis

class <- c_pcaSpectra(BSPCA, choice = "noscale")
```

```
plotScores(BSPCA, main = myt, class,

      pcs = c(1,2), ellipse = "cls", tol = 0.01)
```

#Possible PCA outliers based on Orthogonaal distance

```
diagnostics <- pcaDiag(BSPCA, class, pcs = 2, plot = "OD")
```

#possible PCA Outliers based on Score Distance

```
diagnostics <- pcaDiag(BSPCA, class, pcs = 2, plot = "SD")
```

#scree plot

```
plotScree(class, main = myt)

plotScree2(class, main = myt)

out <- cv_pcaSpectra(BSPCA, pcs = 5, choice = "noscale")
```

#3D plot for PCA

```
plotScores3D(BSPCA, class, main = myt, ellipse = FALSE)
```

#Plot loadings

```
plotLoadings(BSPCA, class, main = myt,

      loads = c(1, 2, 3), ref = 1)
```

#combine two loadings spectra

```
res <- plot2Loadings(BSPCA, class, main = myt,

            loads = c(1, 2), tol = 0.04)

spt <- sPlotSpectra(BSPCA, class, main = myt, pc = 1, tol = 0.001)

spt <- sPlotSpectra(BSPCA, class, main = "Detail of S. repens IR Spectra", pc = 1, tol = 0.05, xlim
= c(600, 1200)
```

Appendix 3 Sampling on Kiruku Hill Apex

Cascade Sampler Mounted on a tree at the Apex

of Kiruku Hill

Kiruku Hill Apex

Appendix 4: Raman Spectrometer Set-up from Physics Department-University of Nairobi
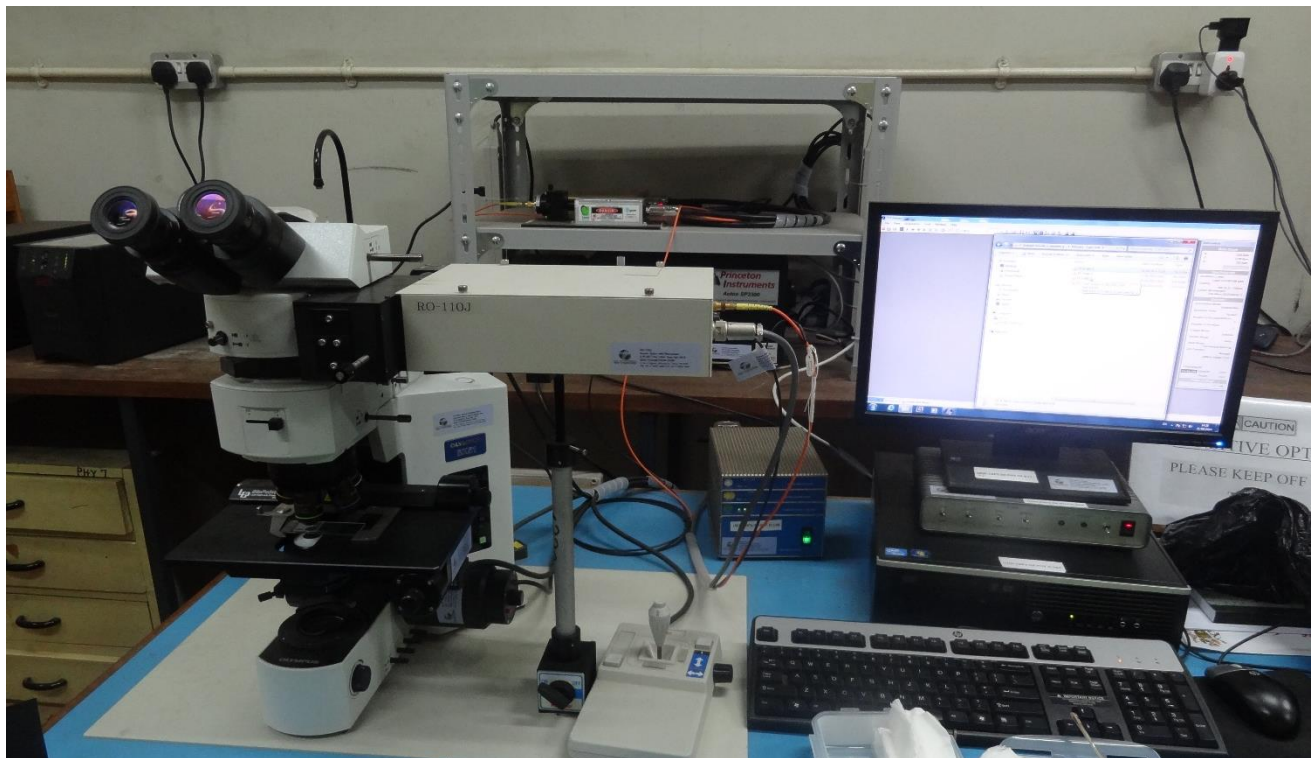
Appendix 5: Uranyl Nitrate Used in Making Simulates and Irradiation Certificate for the IAEA-RGU-1Used for Making Synthetic Standard

IAEA REFERENCE PRODUCTS FOR ENVIRONMENT AND TRADE

IAEA-RGU-1, Uranium Ore

Inorganic, Ores

- o Unit Size: 500g
- o Report: IAEA/RL/148
- o Date of Release: 1987-01-01
- o Producing Laboratory:
- • Certificate of Irradiation: Certificate_of_Irradiation_IAEA-RGU-1

Both, IAEA-RGU-1 and IAEA-RGTh-1 reference materials were prepared on behalf of the International Atomic Energy Agency by the Canada Centre for Mineral and Energy Technology by dilution of a uranium ore BL-5 (7.09% U) and a thorium ore OKA-2 (2.89% Th, 219 µg U/g) with floated silica powder of similar grain size distribution, respectively. No evidence for between-bottles inhomogeneity was detected after mixing and bottling. BL-5 has been certified for uranium, ^{226}Ra and ^{210}Pb confirming that it is in radioactive equilibrium. The agreement between radiometric and chemical measurements of thorium and uranium in OKA-2 shows both series to be in radioactive equilibrium.

Analyte	Value	Unit	95% C.I.	N	R/I/C
^{232}Th	< 4[T]	Bq/kg	-	None	I
^{235}U	228[T]	Bq/kg	226 – 230	None	R
^{238}U	4940[T]	Bq/kg	4910 – 4970	None	R
^{40}K	< 0.63[T]	Bq/kg	-	None	I
K	< 20	mg/kg	-	None	I
Th	< 1	mg/kg	-	None	I
U	400	mg/kg	398 – 402	None	R

(Value) Concentration calculated as a mean of the accepted laboratory means
(N) Number of accepted laboratory means which are used to calculate the recommended or information values and their respective confidence intervals
(R/I/C) Classification assigned to the property value for analyte [Recommended/Information/Certified]
(T) Natural radionuclide activity concentrations derived from the elemental concentrations on basis of isotopic abundance and half-life data

The values listed above were established on the basis of a gravimetric dilution of materials with known uranium, thorium and potassium composition. The details concerning the criteria for qualification as a recommended or information value can be found in the respective report (attached).

(BDH) laboratory reagent

Uranyl nitrate
Of natural isotopic composition
$UO_2(NO_3)_2.6H_2O = 502.13$
Assay (ex U)   Not less than M%
Harmful substance if taken
internally and if in contact   Product
with skin 1 3 8 9 2 6 0   100 g
BDH Chemicals Ltd   Poole   England
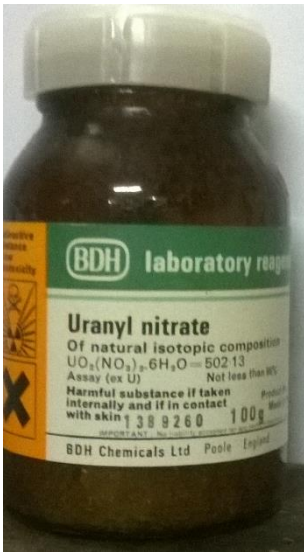
Uranyl Nitrate used in making Simulates

IAEA-RGU-1 irradiance certificate with 400ppm uranium

Appendix 6 Making Stock Solution and Serial Dilutions

The analytical grade salts used for this work were: Sodium Chloride (0.5g), copper sulphate (0.3g) while ammonium nitrate was 0.2g. The background matrix consisted of more Sodium Chloride as it is ideal that the sampling area was expected to be Chloride dominated.

0.15g of Uranyl nitrate dissolved in 100ml of distilled water gives 1500ppm of uranyl nitrate

The concentration of uranium in uranyl nitrate is given by:

$$\frac{RAMofuranium}{RMMofuranylNitrate}*1500\,ppm = \frac{238}{502.129}*1500 = 710.97\,ppm \text{ of uranium}$$

This implies that in the 100ml beaker, there is 710.97 ppm of uranium. This is my stock (highest concentration). Using the dilution formula, other concentrations were obtained. For instance using

$$C_1V_1 = C_2V_2$$

Where C_1 is concentration of the stock and V_1 is the expected volume to be picked from the stock, C_2 is my expected concentration say 200ppm, while V_2 was fixed to be a 10ml container. The 200ppm could be obtained as:

$$710.97*X = 200*10$$

Which would give my X as 2.8ml. This is the volume to be micro pipetted from the stock solution. To make up to 10ml, it will imply that 7.2ml will be micro pipetted from the 100ml beaker having the analar grade salts. Thirty uranium concentrations were prepared based on this approach to constitute the simulate samples.

Expected concentration (ppm)	Volume from Stock (ml)	Volume from base matrix (ml)
65	0.9	9.1
90	1.3	8.7
127	1.8	8.2
150	2.1	7.9
200	2.8	7.2
300	4.2	5.8

Appendix 7: Research Permit from Kenya Forest Service

KENYA Forest Service

Kenya Forest Service Hqs
Karura, Off Kiambu Rd
P.O. Box 30513 - 00100,
Nairobi, Kenya.

Ref. No. HRA/3/KFS/463

Date: 13TH DECEMBER, 2016

Juma Moses Wabwile
University of Nairobi
P O Box 30197 – 00100
Nairobi

Dear Mr. Wabwile,

MASTERS RESEARCH LICENCE

On behalf of the Director, Kenya Forest Service, I have the pleasure of offering you an opportunity to carry out study research at Murima Hills Forest Station in Kwale County for eight (8) days from 14th to 23rd December, 2016.

Please note that this is not an employment offer but an opportunity to gain relevant experience and exposure under the guidance of our experienced officers. No salary, wages or any other benefit is attached to this offer. You will make personal arrangements for your accommodation, travel and insurance.

While undertaking your research you will be expected to abide by all rules and regulations that govern the employees of Kenya Forest Service.

If you accept this offer, please signify by signing in the space provided below and return a copy and a duly filled indemnity agreement to the undersigned.

V. N. MAINGI
FOR: DIRECTOR

I JUMA MOSES WABWILE do accept this offer on the stipulated terms

Signature _____ Date 13th DEC, 2016

Trees for better lives

Tel: (254) 020-3754904/5/6, (254) 020-2014663, (254) 020-2020285, Fax: (254) 020-2385374
Email: info@kenyaforestservice.org, Website: www.kenyaforestservice.org

Appendix 8: Research Permit from NACOSTI

THIS IS TO CERTIFY THAT:
MR. MOSES WABWILE JUMA
of UNIVERSITY OF NAIROBI, 30197-100
NAIROBI, has been permitted to conduct
research in Kwale County

Permit No : NACOSTI/P/16/04025/11431
Date Of Issue : 6th December, 2016
Fee Recieved : Ksh 1000

on the topic: DETECTING URANIUM AND
OTHER RADIOACTIVE ELEMENTS FROM
HIGH BACKGROUND RADIATION AREA
AEROSOLS (MRIMA HILLS KWALE
COUNTY)

for the period ending:
6th December, 2017
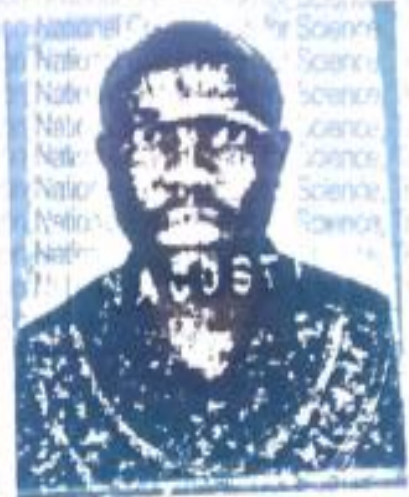
....
Applicant's
Signature

....
Director General
National Commission for Science,
Technology & Innovation

- 135 -